ARISTOTLE UNIVERSITY OF THESSALONIKI
SCHOOL OF GEOLOGY
DEPARTMENT OF GEOPHYSICS

KONSTANTINOS TH. GKOGKAS
Geologist

# INVERSION OF LOVE WAVES FROM AMBIENT NOISE ARRAYS: APPLICATION IN THE MYGDONIA BASIN AREA

MASTER THESIS

*POSTGRADUATE STUDIES PROGRAMME 'APPLIED GEOLOGY',*
*DIRECTION: 'APPLIED GEOPHYSICS AND SEISMOLOGY'*

THESSALONIKI
2018

KONSTANTINOS TH. GKOGKAS
ΚΩΝΣΤΑΝΤΙΝΟΣ Θ. ΓΚΟΓΚΑΣ
Πτυχιούχος Γεωλόγος

INVERSION OF LOVE WAVES FROM AMBIENT NOISE ARRAYS: APPLICATION IN THE MYGDONIA BASIN AREA
ΑΝΤΙΣΤΡΟΦΗ ΚΥΜΑΤΩΝ LOVE ΑΠΟ ΔΙΚΤΥΑ ΚΑΤΑΓΡΑΦΗΣ ΕΔΑΦΙΚΟΥ ΘΟΡΥΒΟΥ: ΕΦΑΡΜΟΓΗ ΣΤΗΝ ΠΕΡΙΟΧΗ ΤΗΣ ΜΥΓΔΟΝΙΑΣ ΛΕΚΑΝΗΣ

Υποβλήθηκε στο Τμήμα Γεωλογίας στα πλαίσια του Προγράμματος Μεταπτυχιακών Σπουδών ‘Εφαρμοσμένη Γεωλογία’, Κατεύθυνση ‘Εφαρμοσμένη Γεωφυσική και Σεισμολογία’

Ημερομηνία Προφορικής Εξέτασης: 20/12/2018
Oral Examination Date: 20/12/2018

**Examinination Board**

Professor C. Papazachos, Supervisor
Researcher B’ ITSAK Dr A. Savvaidis, Member
Researcher Potsdam University Dr M. Ohrnberger, Member

**Εξεταστική Επιτροπή**

Καθηγητής Κ.Παπαζάχος, Επιβλέπων
Ερευνητής Β’ ΙΤΣΑΚ Δρ. Α. Σαββαΐδης, Μέλος Τριμελούς Εξεταστικής Επιτροπής
Ερευνητής  Πανεπιστημίου Πότσδαμ Δρ. M. Ohrnberger, Μέλος Τριμελούς Εξεταστικής Επιτροπής

INVERSION OF LOVE WAVES FROM AMBIENT NOISE ARRAYS: APPLICATION IN THE MYGDONIA BASIN AREA – *Master Thesis*


ΑΝΤΙΣΤΡΟΦΗ ΚΥΜΑΤΩΝ LOVE ΑΠΟ ΔΙΚΤΥΑ ΚΑΤΑΓΡΑΦΗΣ ΕΔΑΦΙΚΟΥ ΘΟΡΥΒΟΥ: ΕΦΑΡΜΟΓΗ ΣΤΗΝ ΠΕΡΙΟΧΗ ΤΗΣ ΜΥΓΔΟΝΙΑΣ ΛΕΚΑΝΗΣ – *Μεταπτυχιακή Διπλωματική Εργασία*

<u>Citation:</u>

Gkogkas K. Th., 2018. – Inversion of Love waves from ambient noise arrays: Application in the Mygdonia basin area, Aristotle University of Thessaloniki, 97 pp.

Γκόγκας Κ. Θ., 2018. – Αντιστροφή κυμάτων Love από δίκτυα καταγραφής εδαφικού θορύβου: Εφαρμογή στην περιοχή της Μυγδονίας λεκάνης. Μεταπτυχιακή Διπλωματική Εργασία, Τμήμα Γεωλογίας Α.Π.Θ., 97 σελ.

*To my grandmother,*
*Athena*

# *Preface*

The current thesis concerns the application of Love wave ambient noise cross-correlation tomography to obtain a 3-D Vs model of the EUROSEISTEST area (Mygdonia basin, northern Greece). This study also attempts to assess the uncertainties of the two-step inversion process that was implemented to obtain the 3-D Vs model. This research was conducted within the frame of the postgraduate studies programme "Applied Geology" (Direction: "Applied Geophysics and Seismology") of School of Geology, of the Aristotle University of Thessaloniki (A.U.Th.).

The first chapter presents information about the geology and the geotectonics of Mygdonia basin. The active tectonics and the seismic hazard of the area are also discussed. Available geotechnical and geophysical results for the study area are also presented.

The second chapter describes the methodology of this thesis. Initially, the principles of surface wave propagation, dispersion and complex wave phenomena are described. Moreover, the nature, sources, wave-field content and the exploitation of ambient vibration recordings are described. Finally, the fundamentals of inversion theory and the application of inversion (e.g. damping and smoothing) constrains are also discussed.

The third chapter presents the obtained results from the application of the method in the EUROSESTEST area and the comparison with the available geological, geotechnical and geophysical information.

I would like to thank my supervisor Professor Papazachos Constantinos for all these years of mentoring and support, even since I was an undergraduate student. This master thesis was strongly improved by his suggestions and comments during the processing and the improvement of the text. Also, I would also like to thank A. Savvaidis and M. Ohrnberger for being members of my advising and examination committee and for providing the data on which this thesis is based. Furthermore, I want to thank Marios Anthymidis for providing several of the scripts which were used in this thesis and for his contribution in this work. Also, I want to thank Katrin Hannemann for providing the FTAN data. Moreover, I would like to thank the whole staff of the Department of Geophysics AUTh for all the theoretical and practical knowledge that they taught me all these years. I wish them all the best.

I would like to thank my friends for all these years that we have been together in good and bad times. Also, I would like to thank my fellow graduate students and colleagues for having a wonderful cooperation while studying together at the School of Geology AUTh during lectures and field-trips. Lastly, I would like to dedicate this thesis to my grandmother, Athena.

# *Contents*

## Περίληψη

Η παρούσα μεταπτυχιακή διατριβή ειδίκευσης πραγματεύεται την εφαρμογή της τομογραφικής αντιστροφής κυμάτων Love από ειδικά δίκτυα καταγραφής εδαφικού θορύβου για τη μελέτη της τρισδιάστατης επιφανειακής δομής της βόρειας Μυγδονίας λεκάνης. Αρχικά περιγράφεται η διασυσχέτιση καταγραφών εδαφικού θορύβου από ειδικό δίκτυο σεισμογράφων που είχε εγκατασταθεί στην περιοχή, καθώς και η επιλογή των καμπυλών διασποράς των κυμάτων Love για κάθε συστοιχία σεισμογράφων. Έπειτα, παρουσιάζονται οι χρόνοι διαδρομής των κυμάτων Love και τα σφάλματά τους, καθώς και η χωρική τους διασπορά που βρίσκεται σε εξαιρετική συμφωνία με την επιφανειακή γεωλογία. Στη συνέχεια περιγράφεται η μέθοδος αντιστροφής που χρησιμοποιήθηκε (αρχικό μοντέλο αντιστροφής, προσεγγιστικοί όγκοι Fresnel, παράμετροι απόσβεσης, χωρικής και συχνοτικής εξομάλυνσης) και παρουσιάζονται τα αποτελέσματα της χωρικής μεταβολής των ταχυτήτων ομάδας των κυμάτων Love για κάθε συχνότητα. Επιπλέον, περιγράφεται μία σειρά δοκιμών της αξιοπιστίας της ανάλυσης του τομογραφικού μοντέλου και της αντιστροφής, ενώ περιγράφονται και τα κριτήρια αποκοπής της τελικής λύσης. Από το τομογραφικό μοντέλο, κατασκευάστηκαν τοπικές καμπύλες διασποράς για ~270 κόμβους του καννάβου, οι οποίοι αντιστράφηκαν ανεξάρτητα με μία μη γραμμική αντιστροφή για να προσδιοριστεί η κατανομή των ταχυτήτων των εγκαρσίων κυμάτων με το βάθος. Το τελικό τρισδιάστατο μοντέλο που προέκυψε από την υπέρθεση των μονοδιάστατων κατανομών των ταχυτήτων των εγκαρσίων σεισμικών κυμάτων με το βάθος βρίσκεται σε συμφωνία με τις τεκτονική δομή της λεκάνης, αλλά και ανεξάρτητες γεωλογικές, γεωτεχνικές και γεωφυσικές πληροφορίες. Τα βάθη των σεισμικών ασυνεχειών εντοπίζονται πιο επιφανειακά σε σχέση με τα παλαιότερα αποτελέσματα για τα κύματα Rayleigh. Συμπερασματικά, προτείνεται ότι η συνδυαστική αντιστροφή των κυμάτων Rayleigh και Love πιθανότατα θα δώσει μία πιο ολοκληρωμένη εικόνα της τρισδιάστατης δομής της περιοχής μελέτης, καθώς και χρήσιμες πληροφορίες για την εγκάρσια ανισοτροπία, ειδικά για τα βαθύτερα ιζήματα, όπως δείχνει η κατανομή των λόγων των ταχυτήτων των S σεισμικών κυμάτων που προσδιορίστηκαν από τα δύο είδη επιφανειακών κυμάτων.

# Abstract

The current master thesis derives a new shallow 3-D Vs model for the EUROSEISTEST area (Mygdonia basin, northern Greece) from high frequency Love wave ambient noise cross-correlation tomography. The recordings were cross-correlated and the Love wave dispersion curve for each cross-correlation path was obtained from manually picking. The computed Love wave group travel-times are in excellent agreement with local geology and the errors of manually picking depict two populations, with the larger error population being spatially distributed mainly in the westernmost part of the study area. The Love wave travel-times for each frequency were inverted using a tomographic approach with the implementation of approximate Fresnel volumes, damping, spatial and inter-frequency smoothing constrains. The Love wave group velocity maps depict the main 2-D basin features and the geometry of the outcropping bedrock is well resolved. Local group slowness dispersion curves were reconstructed for each node of the tomographic grid for solutions satisfying resolution quality cut-off criteria. The local group slowness dispersion curves were inverted using a non-linear Monte Carlo approach and ground profiles with appropriate 1-D Vs variation with depth were generated. The resulting 3-D Vs model, despite its local instabilities, depicts the main basin structure. The derived average bottom layer depths are shallower than the proposed model from Rayleigh waves, with deeper formations exhibiting strong transverse anisotropy. Also, the 3-D Vs model is in good correlation with independent geological, geophysical and geotechnical information. New results for EUROSEISTEST area suggest that the joint inversion of Rayleigh and Love waves would give a better insight in understanding the local 3-D Vs structure.

# CHAPTER 1 – INTRODUCTION

## 1.1 Geological and morphotectonic regime of Mygdonia basin

The study area considered in this present work is located in the Mygdonia basin, which belongs to the central Macedonia region (Northern Greece) and is situated to the E-NE from Thessaloniki. From a geomorphological point of view, it is an elongated basin with a roughly E-W trending main axis, covering a spatially large region, which consists of the lakes Langada and Volvi in its western and eastern part, respectively. The basin is bordered by the mountains of Vertiskos - Kerdyllia (to the north) and Chortiatis - Stratonikos (to the south) and it is characterized by a significant lowering of the geomorphological relief in comparison to its surrounding area. The basin borders and its sigmoidal shape were formed from the activity of neotectonic faults (mainly normal faulting) and the activity of the neighboring North Anatolia Fault (Gkarlaouni et al. 2015).

The study area belongs to the internal Hellenides mountain chain, which was formed during the last phase of the Alpine orogenesis (Figure 1). Furthermore, the largest part of the basin belongs to the Serbomacedonian massif, while the westernmost section is part of the Circum-Rhodope geological zone. Both geotectonic zones consist of a variety of geologic formations, with intense and complex tectonic structures, leading to a long-term debate of the scientific community regarding the origin, subdivision and evolution of these zones (Mountrakis 1993; Kilias et al. 1999; Mountrakis 2010; Kilias et al. 2013). In the present work we present a brief summary of the current understanding regarding these questions for the observed complex geologic and tectonic structure of the broader study area.

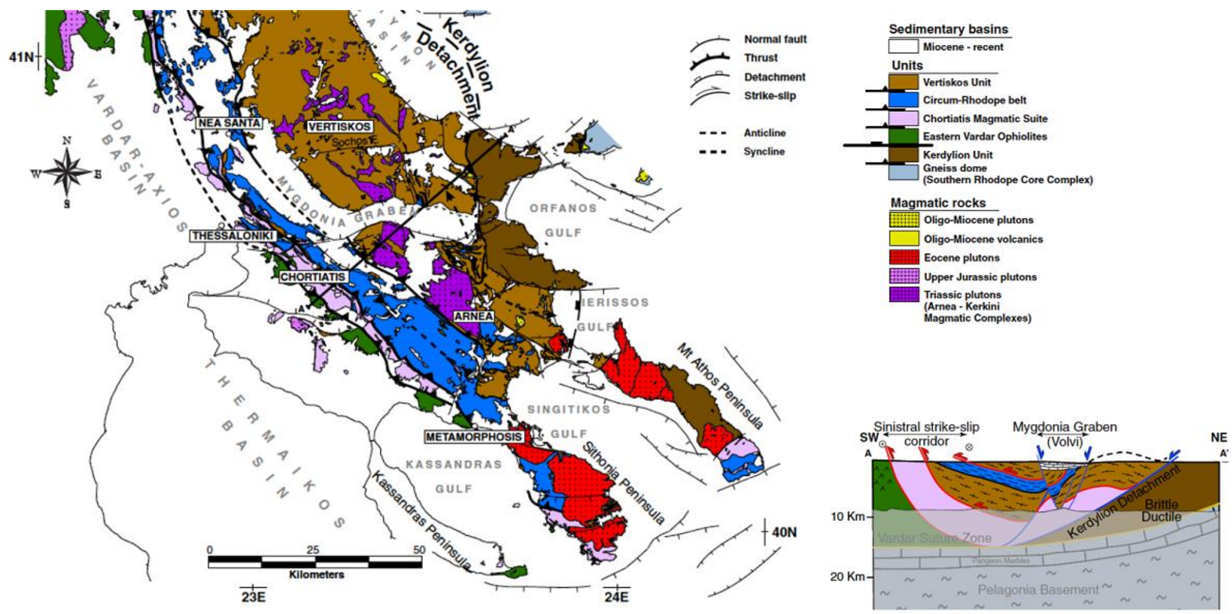


***Figure 1.*** Geotectonic zones, major geologic formations and compressional tectonism of the broader area of internal Hellenides and Mygdonia basin. A geological crustal cross-section perpendicular to the basin main axis is also presented, depicting the brittle and ductile rock conditions (modified from *Kydonakis et al. 2015*).

The Serbomacedonian massif consists mostly of Paleozoic and Mesozoic plutonic rocks, such as gneiss, schists, marbles and ophiolites, and is subdivided in two units; the westernmost Vertiskos unit and the easternmost Kerdyllia unit (Mountrakis 2010). The contact between the Vertiskos and Kerdyllia units is an old thrust fault, the Strymon or Kerdylion fault, which has reversed to an active low angle detachment fault (at present) that underlies the Neogene age Strymon supra-detachment basin (Burg 2012; Kydonakis et al. 2015). This is probably the mechanism that led to the obduction of both units above the Rhodope and the presence of an enigmatic thrust fault that led to the superposition of the Vertiskos unit above Kerdyllia (Kilias et al. 1999). The border between the Serbomacedonian massif (Vertiskos unit) and the Circum-Rhodope zone (overlying Neogene sediments) is a strike-slip fault with a significant thrust component, which has led to the fluctuating overlay of Vertiskos unit and Circum-Rhodope Neogene sediments above each other (Tranos et al., 1993).

Contrary to previous suggestions regarding the relationship between the subdivisions of Serbomacedonian massif and Rhodope, recent research (Kilias et al. 2013; Burg 2012; Kydonakis et al. 2015) has proposed a new conceptual model, according to which these geotectonic units are actually nappes overlying a metamorphic core in Rhodope (Figure 2). More specifically, both Vertiskos and Kerdyllia units extend to Rhodope zone's Kimi and Sidironero units, respectively (Kilias et al. 2013). This assumption is based on the correlation of the geologic structure of the above units and their cooling ages. However, the correlation between Vertiskos and Kimi or the overlying Asenitsa nappe (the metamorphic core complex uppermost nappe outcropping in southern Bulgaria) is still ambiguous (Burg 2012).

The Chalkidiki block, which contains Mygdonia basin, is bounded by a sinistral strike slip fault (compressional boundary) in its westernmost part and a detachment fault (extensional boundary) in its easternmost part. Due to crustal accretion, ductile rock conditions prevail at larger depths, while shallow geologic formations are in brittle conditions, resulting in significant faulting, combined with the regional stress field (see next section for details). A simplified geologic cross-section of all Alpine geotectonic zones neighboring the Mygdonia basin is shown in Figure 1. A regional scale cross-section extending up to Rhodope units is shown in Figure 2, featuring the southern and northern Rhodope metamorphic core complexes (Kydonakis et al. 2015).

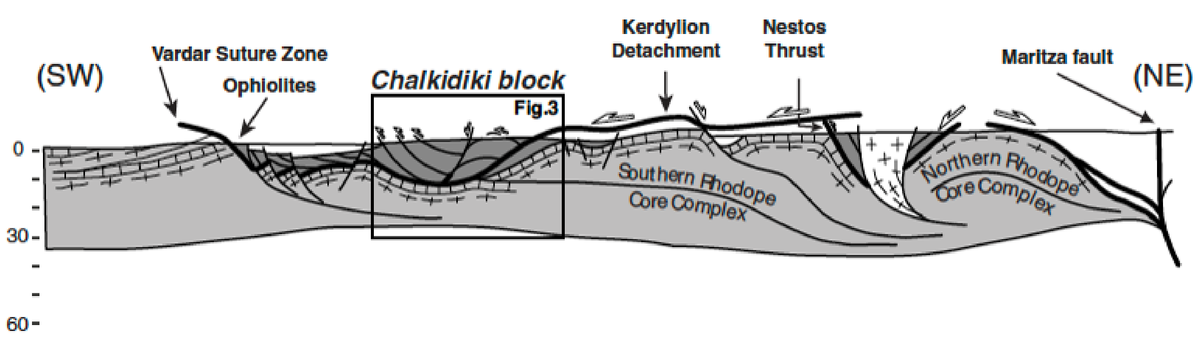


***Figure 2.*** Regional crustal scale geological cross-section of northern Greece's major Alpine geotectonic zones. The Chalkidiki block, which includes the Mygdonia basin and the study area, is depicted with a black rectangle (from *Kydonakis et al. 2015*).

### 1.1.1 Lithology

Mygdonia basin exhibits a complicated lithostratigraphy due to the intense geotectonic setting of the Serbomacedonian massif during the Alpine orogenesis and the neotectonic activity of the area, leading to the basin generation and vast sedimentation under different processes that took place in Neogene-Quaternary (Figure 3). The sedimentation which occurred after the establishment of the Alpine units was intense, with a deposition of sediments up to 400m in the center of the basin (Psilovikos 1977), due to the action of the neotectonic faults that formed the basin. Therefore, the basin structure can be summarized in three main geological units: a) the Alpine bedrock, b) the pre-Mygdonian system and, c) the Mygdonian system.

The Alpine bedrock consists of a mixture of continental (Kerdyllia unit) and oceanic (Vertiskos unit) crust geologic formations. The oceanic crust formations are meta-ophiolites and meta-gabbro, which outcrop in the northern part of the basin and formulate the border between the Kerdyllia and Vertiskos units. The basement rocks are exposed at the borders of the basin and are mainly metamorphic rocks, such as gneiss, phyllites, schists and amphibolites, indicators of the different metamorphic phases that took place during the geotectonic evolution of each unit. In addition, Alpine granitic intrusions are reported in the Arnaia area (dated in 240 Ma; Poli et al. 2009), which is correlated with the rupture of Pangea (pre-orogenic), as well as in Phanos area (U. Jurassic; Michail et al. 2016) which intrudes ophiolithic rocks (syn-orogenic). The gneiss bedrock was formed due to the metamorphism of granitic intrusions of this age (Kilias et al. 1999). Also, newer intrusions took place during the last stage of the orogenic circle, amongst which in Sithonia and Olympiada (Christofides et al 2001, Gurk et al 2007), forming ore deposits and geothermal fields in the broader area.

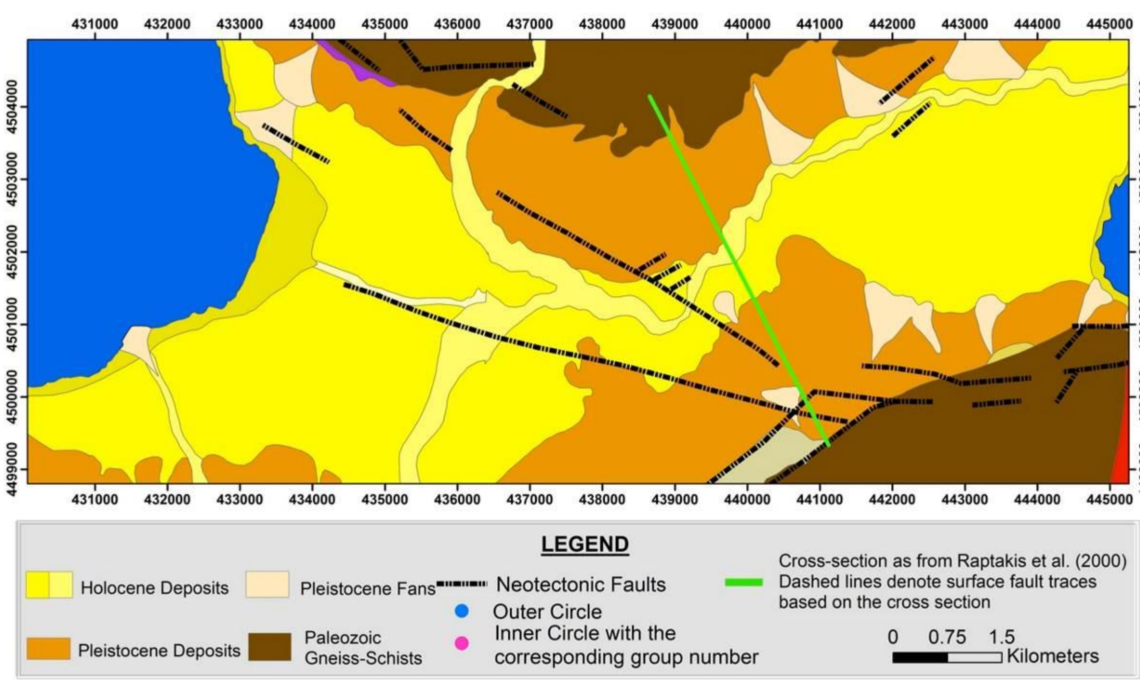


***Figure 3.*** Geological map of central Mygdonia basin (coordinates in EGSA87 Greek Transverse Mercator system), depicting the major geological units and neotectonic faults of the basin.

### 1.1.2 Stratigraphy and post-Alpine evolution

The sedimentary deposits of the Mygdonia basin have been well-studied (Psilovikos 1977, Sotiriadis et al. 1983, Koufos et al. 1995), providing significant information on the main stratigraphic heterogeneities, which correspond to different depositional conditions of the basin formations. Also, precise dating has been conducted for most units, mainly due to the presence of a large number of mammal fossils. These sediments were deposited shortly after the normal faulting activity in Lower – Upper Miocene and due to the intense erosion of the surrounding crystalline rocks. These sediments are classified in two main systems, namely the pre-Mygdonian and the Mygdonian units, which consist of different lithologies, exhibiting varying soil mechanical properties due to their different compaction rates and age.

The pre-Mygdonian system sediments comprise mainly of clastic sediments of Neogene age and the Alpine basement of the area (Serbomacedonian massif metamorphic rocks). The deposition of pre-Mygdonian sediments started in Lower - Upper Miocene, with conglomerates, sandstones, red-beds and silty-sand deposits with clay intercalations under fluvio-lacustrine and terrestrial conditions (Sotiriadis et al. 1983). The Mygdonian system lithostratigraphic column starts with a conglomerate, typical indicator of cessation of sedimentation and is followed up by mainly alluvial deposits of fluvial, fluvio-lacustrine, lacustrine and terrestrial conditions. The Mygdonian system sediments are softer and have a smaller thickness in comparison to the pre-Mygdonian sediments.

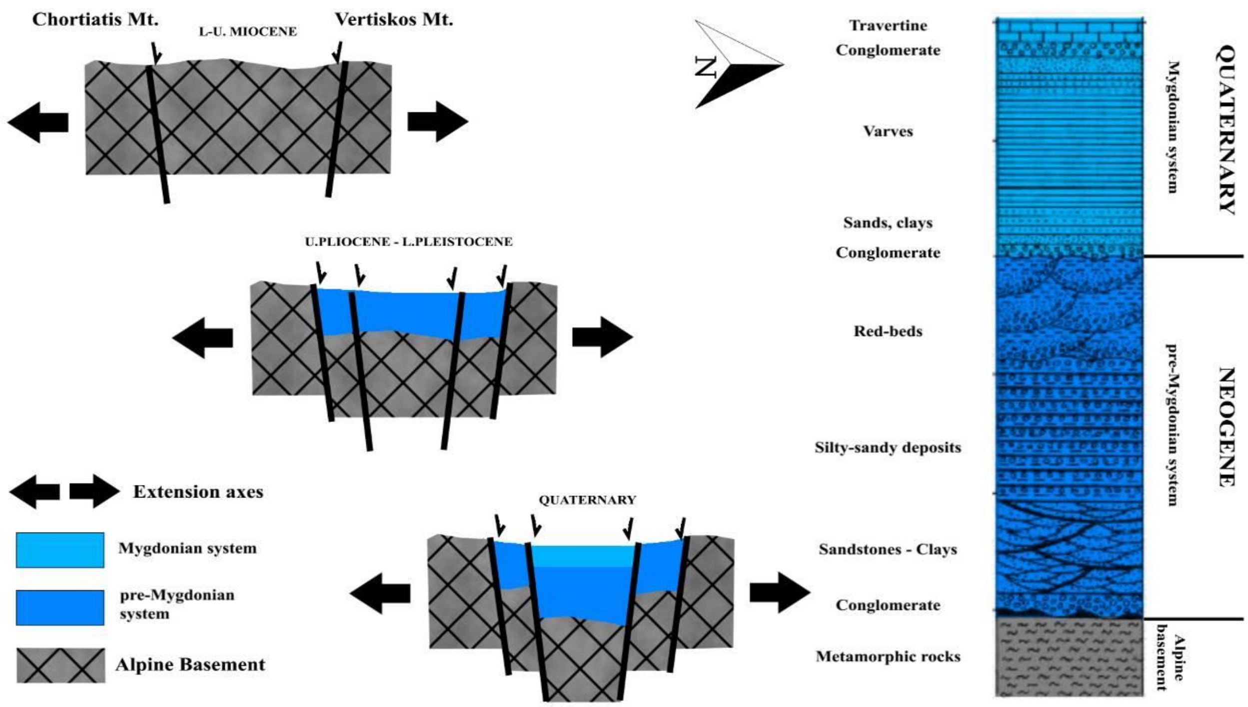


***Figure 4.*** Schematic representation of the evolution of Mygdonia basin (left) and typical geological column (right), with the main sedimentary units (modified from *Sotiriadis et al. 1983*).

The formation, structure and evolution of the Mygdonia basin is typical for a sedimentary basin. It was formed in Lower - Upper Miocene from the activity of normal faults with an E-W trend axis. During this period new faulting took place with mainly E-W normal faults acting in the middle of the basin and generating space for the deposition of Mygdonian system sediments. Moreover, a large lake (named Mygdonia), was formed in the area, and lacustrine sediments were deposited mostly in the middle of the basin. Nowadays, lakes Langada and Volvi are the leftovers of this Mygdonia lake, and alluvium and fluvial sedimentation is taking place.

The evolution of Mygdonia basin and a characteristic lithostratigraphic column provided by Sotiriadis et al. (1983) is shown in Figure 4, where basement rocks are marked with a grey color and the pre-Mygdonian and Mygdonian system sediments with blue and light blue colors, respectively. The E-W striking normal faults are shown with thick black lines, identifying the extensional stress field that led to the fragmentation of the basement rocks in two phases. These phases resulted in the generation of the basin (i) and the deposition of pre-Mygdonian (ii) and Mygdonian (iii) system sediments under intense erosion (due to gravity and relief anomalies) and different sedimentation conditions.

The boundaries of the basin are formed by the activity of neotectonic faults over the last million years, forming terraces and lowering of the geomorphological relief. In addition, these faults have different slip rates, generating a multifragmented regime (Pavlides 1990). Quantitative morphotectonic studies conducted by Pavlides and Chatzipetros (1998) have revealed three units of tectonic slopes, while seismotectonic and microzonation studies have revealed that they tend to be tectonically active (see next section and references therein). These units consist of:

a) High dip angle unit, observed along active fault zones and resulting in the crystalline basement rocks fragmentation, with significant slips. They are the oldest reported slopes that created the basin, followed by a relief gradient lowering due to different soil and rock mechanical properties

b) Low dip angle faults, affecting mainly Neogene formations, products of the second tectonic phase that took place in U. Pliocene – L. Pleistocene.

c) Present stress field abrupt dip angle faults, affecting Neogene - Quaternary formations, with low slip rates.

The Alpine orogenesis tectonism was accomplished under plastic rock conditions, while recent tectonics are taking place under brittle conditions, causing the deformation and the elimination of older thrust structures. Therefore, Alpine tectonic structures are well maintained or identified as fragments, mainly found in the surrounding Chalkidiki block (e.g. folds, S-C clasts, foliation patterns and more; Kilias et al. 1999, Kydonakis et al., 2015), while being affected by present day tectonics under brittle conditions. The study area's active tectonic field comprises mostly of extensional and secondary of strike slip structures, most of them being seismically active faults, with the occurrence of destructive historic earthquakes (see next section and references therein).

## 1.2 Active tectonics setting

The tectonic setting follows the general northern Greece N-S extension taking place due to the subduction of the African plate under Europe (e.g. Papazachos and Comninakis 1969). The seismicity of the area is significant, despite the fact that it is less intense than in other areas, such as the Hellenic arc or the Ionian islands. A significant number of earthquakes have occurred along several rupture zones (see spatial distribution in Figure 5, obtained from Galanis et al. 2004). Also, many urban centers can be found within the basin or in the surrounding area, such as Thessaloniki, the second largest city of Greece, that suffered severe damages and financial losses due to the 20/06/1978, $M_s$ = 6.5 earthquake (Papazachos et al. 1979). This earthquake is the main reason of a long-term seismological, geophysical and geotechnical investigation of the area, also leading to the establishment of the EUROSEIS program (see next section for details).

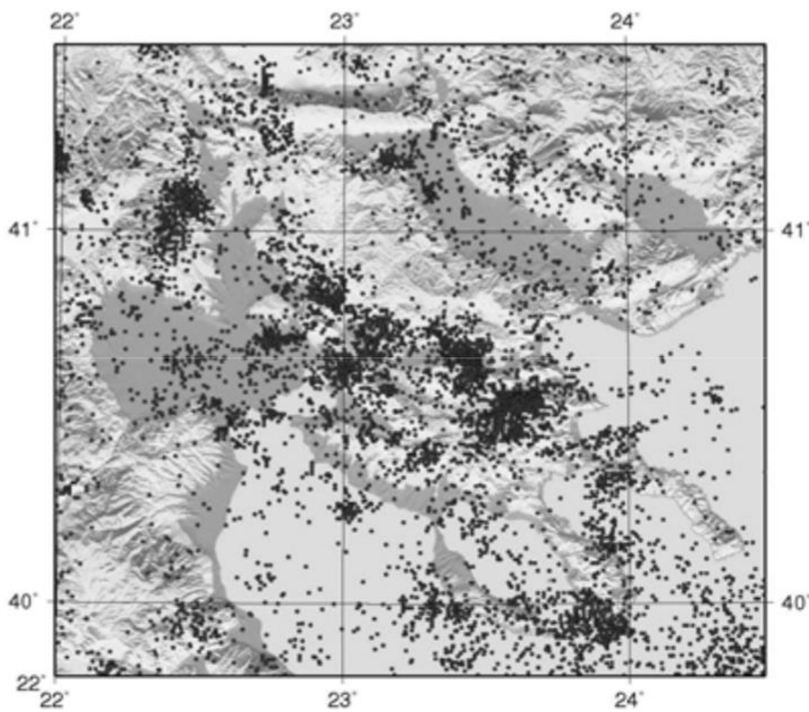


***Figure 5.*** Spatial distribution of earthquake epicenters of the broader study area for the period 1981 - 2003 (from *Galanis et al. 2004*)

The Internal Hellenides and the Chalkidiki blocks are located in the northern section of the back-arc area of the current subduction processes, with extensional deformation prevailing and creating normal faults with E-W and NW-SE directions, that bound the basin. It is well known that strike slip faults with WNW-ESE and NE-SE strike also occur due to the presence and impact of the left-lateral strike-slip Northern Anatolia fault, situated to the southeast with respect to the basin (see Figure 6). Furthermore, the North Anatolia fault activity involves the rotation of the main extensional deformation axes, generating the sigmoidal basin shape (Gkarlaouni et al. 2015). The seismic activity along these faults comprises of shallow earthquakes, occurring at large dip angle normal or strike-slip faults.

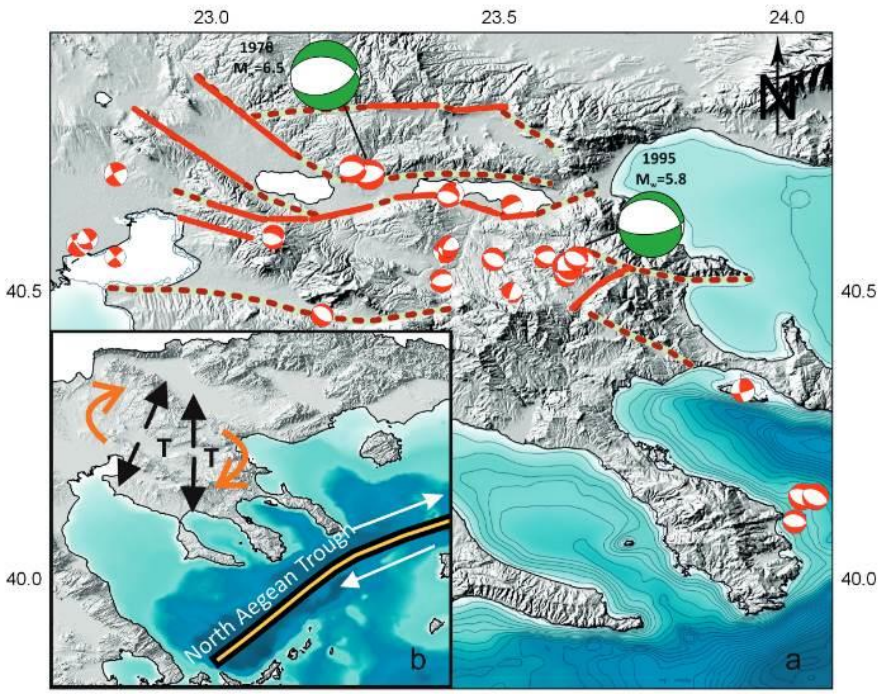


***Figure 6.*** a) Major neotectonic faults of the broader Mygdonia basin. b) Rotation of extension stress axes due to North Anatolia fault activity (from *Gkarlaouni et al., 2015*).

The normal faults of the broader study area can be classified into two groups, namely a southern group and a northern group, with different characteristics regarding their faulting, seismicity and structure (Gkarlaouni et al. 2015). The southern group consists of faults with large surface ruptures and extends from Thessaloniki to Gerakarou (Figure 7). The northern group of faults is mainly depicted by seismological data rather than field observations, resulting into smaller vertical displacements in comparison to the southern group of faults, undergoing half-graben tectonics (Mountrakis 2010). The measured displacement rates of Mygdonia basin are ~5 - 6 mm/year, revealing a N-S deformation pattern, in agreement with seismological and neotectonic results (Doukas et al. 2004). Based on the studies of Papazachos et al. (2001), Tranos et al. (2003), Paradisopoulou et al. (2006) and Vamvakaris et al. (2006), the rupture zones of Mygdonia basin can be classified as:

a) A NW-SE striking rupture zone in the westernmost part of lake Langada with extensional deformation (NE-SW tensional axes direction). This zone consists of two major faults, the Agios Vasileios fault (L-AV.F) in the southern boundary of the basin and the Assiros-Analipsis (As-An.F) and Nikopolis-Xylopolis fault system (N-X.F) in the northern.

b) An E-W and ENE-WSW rupture zone extending from the easternmost part of Thessaloniki to the region between lakes Langada and Volvi. This zone consists of the Stivos-Gerakarou fault system (TGFZ), the Pylaia-Panorama fault (P-P.F), the Peristeras fault (PR.F), the Asvestochorion-Chortiatis fault (A-Ch.F), the Pefka-Asvestochorion fault (P-A.F) and Stivos-Gerakarou faults (S-G.F). The extensional axes have a N-S to NNW-SSE orientation near

Thessaloniki and NNE-SSW near Gerakarou.

c) A N-S extensional rupture zone near lake Volvi and NNW-SSE in the NW part of the basin. The epicenter of the $M_s$ = 5.8 Arnaia earthquake (04/05/1995) is located in this zone.

The major fault systems that were mentioned above can be seen in Figure 7, as presented by Paradisopoulou et al. (2006), following previous work by Tranos et al. (2003). The N-S extension is dominant through the basin tectonics, causing the E-W, NNE-SSW, NNW-SSE faulting towards the westernmost part of the basin, near the Thessaloniki urban area. The easternmost deformation of Mygdonia basin is also significant, with the occurrence of the Ierissos $M_s$ = 7.4 26/09/1932 earthquake (Papazachos and Papazachou, 2003).

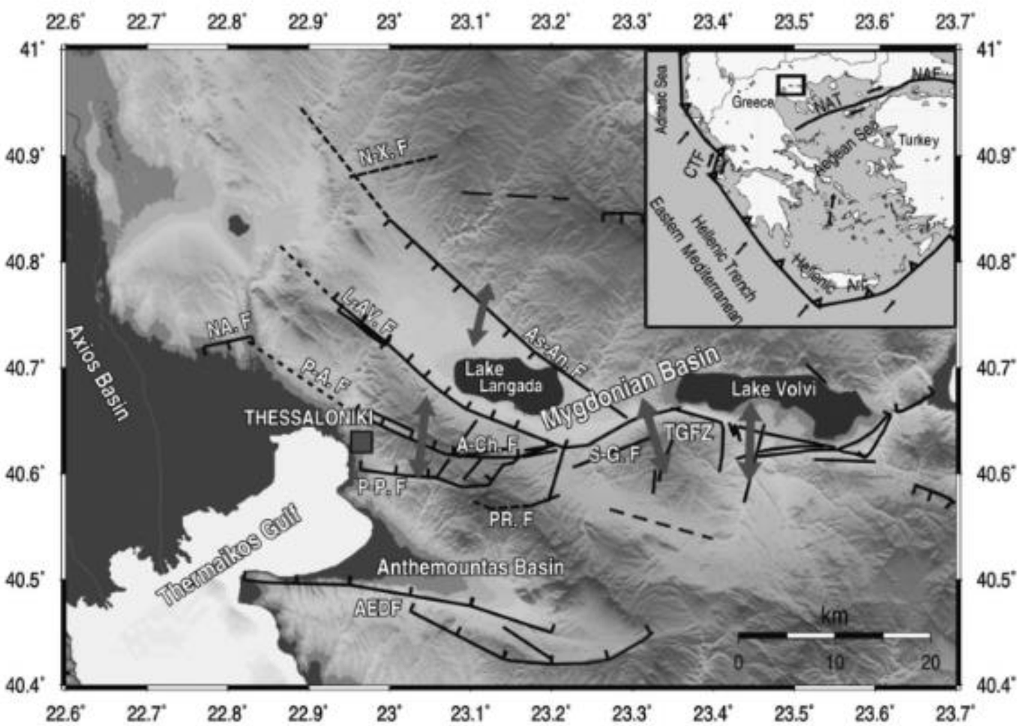


***Figure 7.*** Neotectonic map of the Thessaloniki – Mygdonia and Athemountas basins (from *Tranos et al., 2003*). Regional scale tectonics are also depicted in the subfigure (see text for details, figure from *Paradisopoulou et al., 2006*).

## 1.3 Previous geophysical studies

The previous discussion and presented results verify that the active tectonics setting of Mygdonia basin is significant and the resulting seismic risk is quite high. The long term seismological, neotectonic, geophysical, geotechnical and geodetic assessment of the area has provided fruitful information for an improved understanding of the regional and local tectonics that are taking place in the area. The EUROSEISTEST program, established in 1993 after the occurrence of the $M_s$ = 6.5 Thessaloniki earthquake (http://euroseisdb.civil.auth.gr), has provided useful information on these topics.

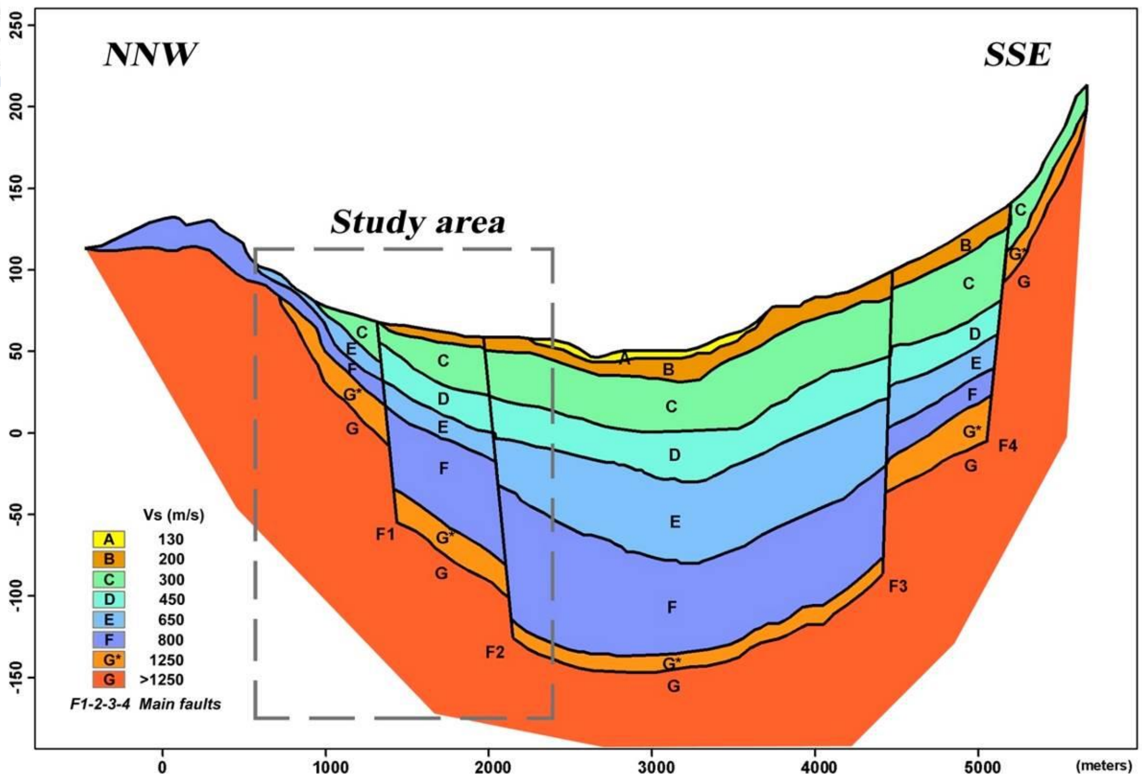


***Figure 8.*** Cross-section of Mygdonia basin showing its Vs structure, with eight prevailing seismic layers. The cros-section is depicted with a green line in Figure 3 (from *Hannemann et al. 2014*, modified from *Raptakis et al., 2010*).

| LAYER | A | B | C | D | E | F | G* | G |
|---|---|---|---|---|---|---|---|---|
| **Vs (m/s)** | 120 | 200 | 300 | 450 | 650 | 800 | 1250 | >1250 |
| | **Mygdonian System** | | | | **Pre-Mygdonian System** | | **Bedrock** | |

***Table I.*** Correlation between seismic layers, as revealed by their Vs velocities, and the main basin geological units.

A 2-D cross-section of Mygdonia basin, perpendicular to its main axis, is presented in Figure (8), as modified from Raptakis et al. (2010). The cross-section has a NNW-SSE direction (green line in Figure 3) and was compiled on the basis of results from seismic refraction, MASW and geotechnical surveys, extending roughly 5500m in horizontal distance and up to a depth of 200m. The section reveals the geometry of the main sedimentary geological formations, bedrock depth and the major tectonic features of the basin. Eight seismic strata with a normal Vs velocity increase with depth have been proposed on the basis of the determined Vs velocities values, also shown in Figure 8. The correlation of these layers with the bedrock, the pre-Mygdonian system and the Mygdonian system sediments is depicted in Table I, with a Vs velocity range extending from 150 m/s up to 1250 m/s. Layers A-D correlate with the pre-Mygdonian system sediments, (Vs values from 120 - 450 m/s), layers E-F correspond with the Mygdonian system sediments (Vs values 650 - 800 m/s), while layers G* and G depict the weathered and healthy bedrock formations, respectively (Vs velocities ≥ 1250 m/s).

An extension to three dimensions of the previous study was conducted by Manakou et al.

(2010), who compiled results from multiple surveys (such as ambient noise, seismic methods and geotechnical data from the area), in order to propose the 3-D model shown in figure 9. Their results are in very good agreement with previously published information and provide an insight on the three-dimensional features of the basin, such as the depths of layers A and B (Figure 9a) and layers C and D (Figure 9b) of the pre-Mygdonian system, which reach up to a thickness of 250m in the central part of the basin. Also, their results suggest an approximate thickness of 150m for the Mygdonian system sediments - layers E and F (Figure 9c) and a maximum bedrock depth of 400m in the eastern-central part of the basin (Figure 9d). The proposed Holocene and Quaternary sediments thickness is larger in the southern and the easternmost part, while older Pleistocene sediments of the pre-Mygdonian system are thicker in the westernmost part of the basin, a clear indicator of the complex tectonic history and activity of the area.

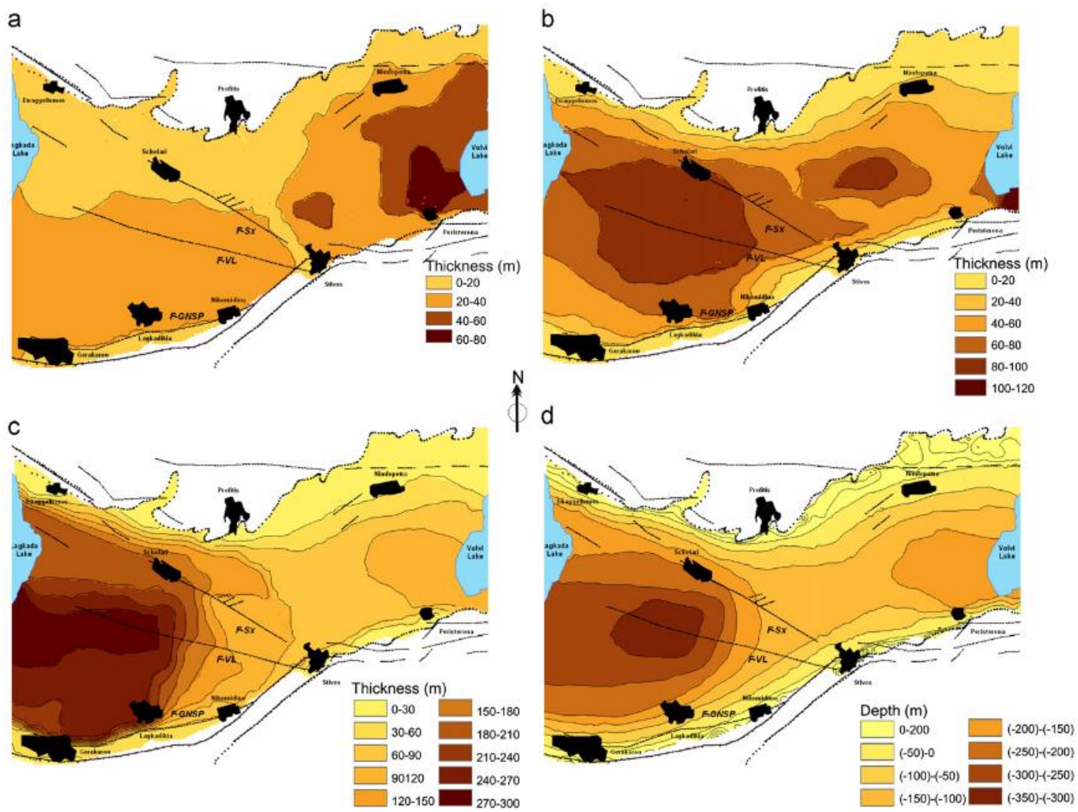


***Figure 9.*** Three-dimensional structure of the central part of Mygdonia basin, derived by the compilation of several geophysical and geotechnical surveys (from *Manakou et al., 2010*).

## 1.4 Study area

The study area of the present thesis is located in the northern part of the basin, where sediments are expected to have a smaller thickness due to the half-graben tectonism of the basin, as reported earlier. The major geologic units of the area, bounded by the red rectangle of Figure 10, consist of the Paleozoic crystalline basement rocks (northern part), the Pleistocene sediments of the pre-Mygdonian system (central part) and the Holocene-Quaternary sediments of the Mygdonian system (southern part). It should be noticed that the study area includes all major geologic units of the basin, whereas their characteristics can be studied at shallower depths, rather than in other sections of the basin, where reported results suggest larger depths and more complex geometries.

The main focus of this study was to retrieve information regarding the 3-D Vs structure of shallow formations by implementing a tomographic approach from ambient noise cross-correlation tomography. For this reason, a temporary instrument pool was installed in the northern part of the basin, depicted by the red rectangle of Figure 10. In total, 28 instruments were installed in two circles, an outer circle with diameter ~1.8km (blue dots in Figure 10) and an inner circle with diameter ~700m (purple dots in Figure 10) consisting of 8 instruments, which were moved during the network operation. The total ambient noise recording time was 8-15 hours per day, with the inner circle instruments being moved each day (7 times in total), in order to obtain a denser network coverage and sustain possible data losses (see Chapter 3 for details). More than 12 GB of mini-SEED data were collected in total, with a recoding rate of 100 Hz.

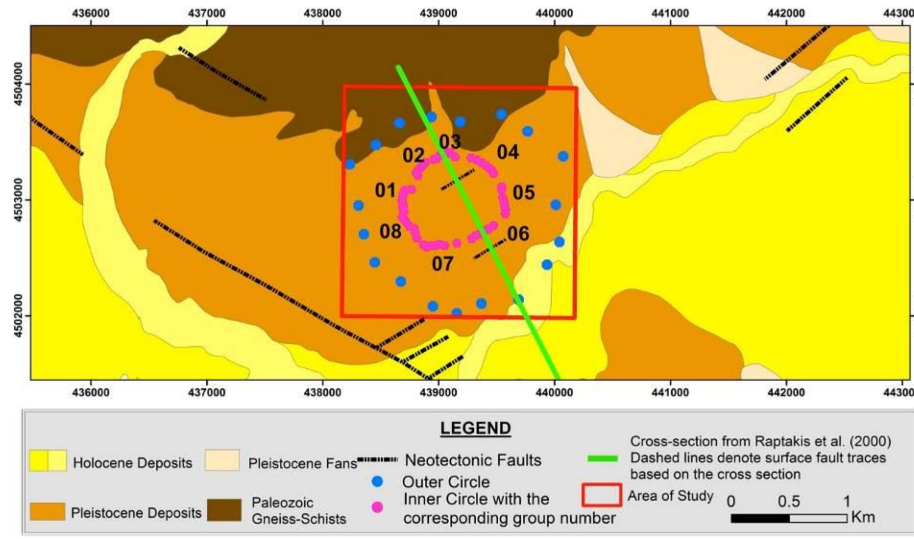


***Figure 10.*** Close-up of Figure 3, where the study area is depicted with a red rectangle. The positions of the inner (purple) and outer (blue) circles of the instrument pool are also shown, together with the 2-D cross section of *Raptakis et al., 2010* (green line) and the neotectonic faults (black lines). The inner circle instruments were moved during the operation of the network and are annotated by their original position (from *Hannemann et al., 2014*).

During this study we utilize the approach of Hannemann et al. (2014), who applied ambient noise cross-correlation tomography for Rayleigh waves from the same recording network, for Love waves. The resulting Rayleigh wave group velocity spatial variation for six frequencies is presented in Figure 12. The group velocities for Rayleigh waves in the northern part (bedrock outcrop) of the array are much faster than in the southern (sedimentary deposits), with their boundary roughly depicted by the ~700 m/sec velocity level. This velocity change is in good agreement with local tectonics, changing the boundary strike from WNW-ESE in the western part to EWE-SNS in the eastern part of the northern basin border. The derived group velocities for each frequency were used to reconstruct local group slowness dispersion curves for each node of the tomographic grid. The reconstructed local group slowness dispersion curves were inverted using a neighborhood algorithm, in order to generate a pseudo-3D Vs model for the area.

Hannemann et al. (2014) inverted all Rayleigh group slowness dispersion curves independently to obtain 1-D Vs depth variations for each node and a pseudo-3D Vs model was generated from the superposition of all 1-D models. Table II presents the model parameterization that was tested for each 1-D inversion. For each model the Table provides the name of the model, the number of layers above the half-space, the Degrees of Freedom (DOF) for parameters allowed to vary in the inversion, the fixed Vs layer velocities and the allowed depth range for each layer interface.

The resulting layer depths for each model parameterization adopted by Hannemann et al. (2014) for the inversion of the Rayleigh wave local group slowness dispersion curves are shown in Figure 13. The presented layer depths are averaged from all model parameterizations and the cross-sections (parallel to the EUROSEISTEST cross-section shown in Figure 8) depict the average bottom interface of each velocity layer, which was computed from averaging the bottom layer interfaces of each node inside the white polygon (Figure 13-left). The three lower EUROSEISTEST discontinuities (layers discontinuities E/F, F/G*, G*/G in Table I and Figure 8) proposed from Raptakis et al. (2010) were used for comparison.

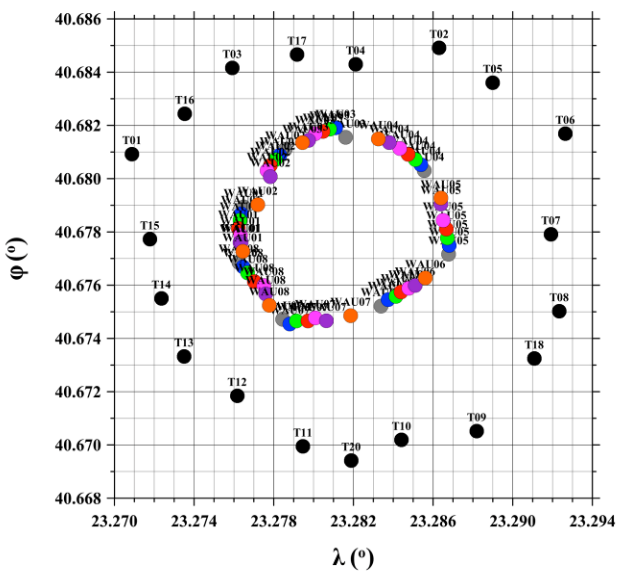


***Figure 11.*** Instrument geometry for the study area in geographic coordinates (WGS84), after the repetitive installation of inner circle instruments in different locations during the operation of the temporary network.

The Mygdonian system sediments (layers A and B in Table I and Figure 8) have small thicknesses and small inter-model variability, in good agreement with the local geology. The pre-Mygdonian system sediments (layers C-F in Table I and Figure 8) have much larger thicknesses to the right (south) of fault F1 in all cross-sections, but this thickening is observed closer to the center of the basin than the F1 fault position proposed by Raptakis et al. (2010). The pre-Mygdonian system sediments are parameterized with 4 layers, while models with fewer (e.g. models 5/6UL) or too many layers (e.g. 8UL) exhibited stronger and even unrealistic variations. The bedrock formations (weathered, G* and healthy, G in Table I and Figure 8) are better resolved using a single layer parameterization (Vs = 800 m/sec), since models with free bedrock parameterizations or inter-bedrock discontinuity parameterization (e.g. 8UL) tended to generate unrealistic bedrock depth variations. Therefore, Hannemann et al. (2014) proposed a Vs model based on the 7UL-2 model parameterization, as this is listed in Table II.

The obtained results for the bottom layer interfaces (discontinuities) are shown in Figure 14, where magneto-telluric results and the proposed Vs model from Raptakis et al. (2010) are superimposed for comparison. In general, the obtained seismic bedrock depths and the morphology of the bedrock/sediments discontinuity (from the noise data inversion) are in good agreement with the high resistivity bedrock identified by the magneto-telluric results. Although the magneto-telluric model extends up to the depth of 100 m, the sediments dipping at the section horizontal distance around 300 m distance is clearly recognized from both models, with a shift of ~100 m towards the basin center compared to the proposed F1 fault position by Raptakis et al. (2010). The fault F2 is not identified in any model, since it does not seem to affect shallow layer interfaces. Also, the seismic layer interfaces depict the presence of an uplift at horizontal distance locations 600m to 1000 m, indicating the possible presence of a horst-type structure. This structure is also indicated in the group velocity results (Figure 12), showing approximately a feature dimensions of ~200mX200 m.

| Name | Number of Layers | DOF | Vs (m/sec) | Layer Depth Range (m) |
|---|---|---|---|---|
| **5UL** | 5 | 8 | 250, 350, 425, 600, 800 | 1-300 |
| **6UL-1** | 6 | 9 | 150, 250, 350, 425, 600, 800 | 1-300 |
| **6UL-2** | 6 | 9 | 250, 350, 425, 600 | 1-100 |
| | | | 700, 800 | 1-200 |
| **7UL-1** | 7 | 10 | 150, 250, 350, 425, 600, 700, 800 | 1-300 |
| **7UL-2** | 7 | 10 | 150, 250 | 1-50 |
| | | | 350, 425 | 1-100 |
| | | | 600 | 1-200 |
| | | | 700 | 1-250 |
| | | | 800 | 1-300 |
| **7UL-3** | 7 | 10 | 150, 250 | 1-50 |
| | | | 350, 425 | 1-100 |
| | | | 600, 700 | 1-300 |
| | | | 800 | 1-500 |
| **8UL-1** | 8 | 11 | 150, 250, 350, 425, 600, 700, 800 | 1-300 |
| | | | 1200 | 1-500 |
| **8UL-2** | 8 | 11 | 150, 250 | 1-50 |
| | | | 350, 425 | 1-100 |
| | | | 600 | 1-300 |
| | | | 700 | 1-400 |
| | | | 800, 1200 | 1-500 |

***Table II.*** List of model parameterizations used for the 1-D inversion of Rayleigh wave group dispersion curves, as adopted by *Hannemann et al. (2014)*.

The current thesis presents new results from the inversion of Love wave group travel-times from the same network used by Hannemann et al. (2014), as presented in Figure 11. We also attempt to assess the reliability of all inversion steps leading to the model derivation and recover useful information on the geophysical structure of the study area. Model uncertainties emerging from the two-step inversion procedure adopted from Hannemann et al. (2014) are also discussed. The tomographic inversion of Love wave group travel-times for each frequency is performed with the use of approximate Fresnel volume ray-tracing, as well as damping, spatial smoothing and inter-frequency constrains. Finally, the 1-D inversion of reconstructed local dispersion curves for each node is performed using an adapted Monte-Carlo approach and a new 3D Vs model is reconstructed for the study area.

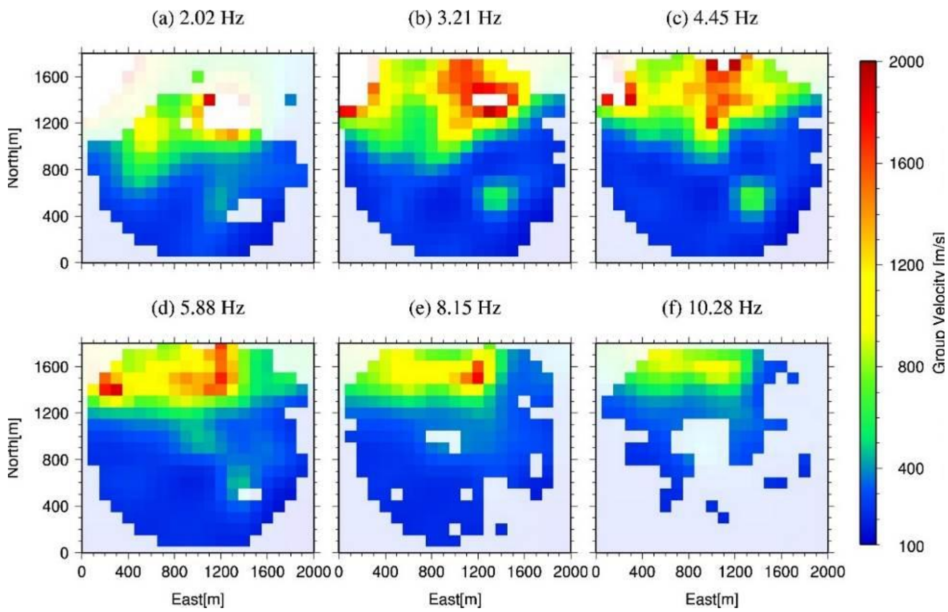


***Figure 12.*** Spatial variation of the Rayleigh wave group velocities for six frequencies of the study area (from *Hannemann et al., 2014*).

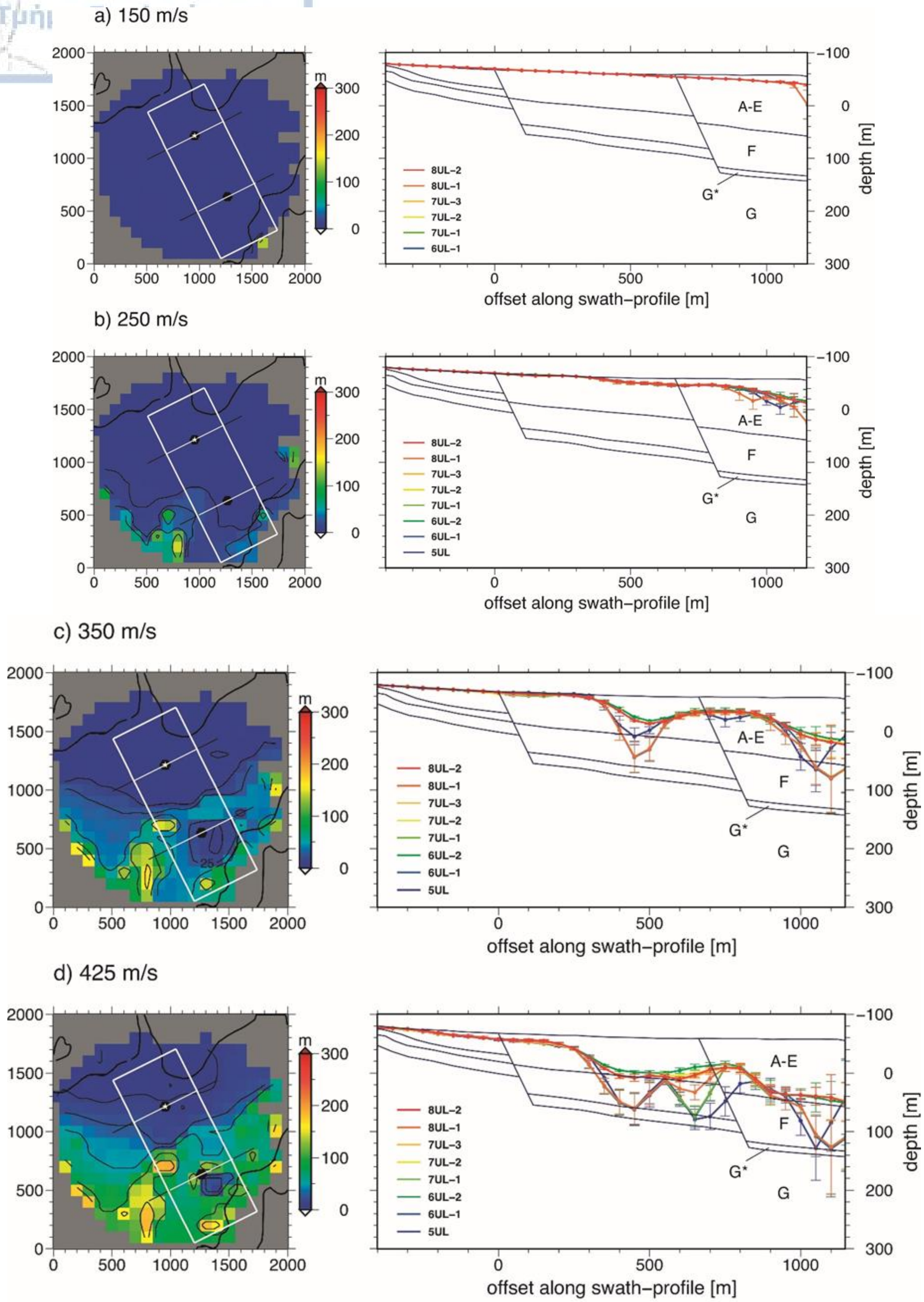
a) 150 m/s
b) 250 m/s
c) 350 m/s
d) 425 m/s
offset along swath−profile [m]
depth [m]
A-E
F
G*
G
8UL−2
8UL−1
7UL−3
7UL−2
7UL−1
6UL−2
6UL−1
5UL

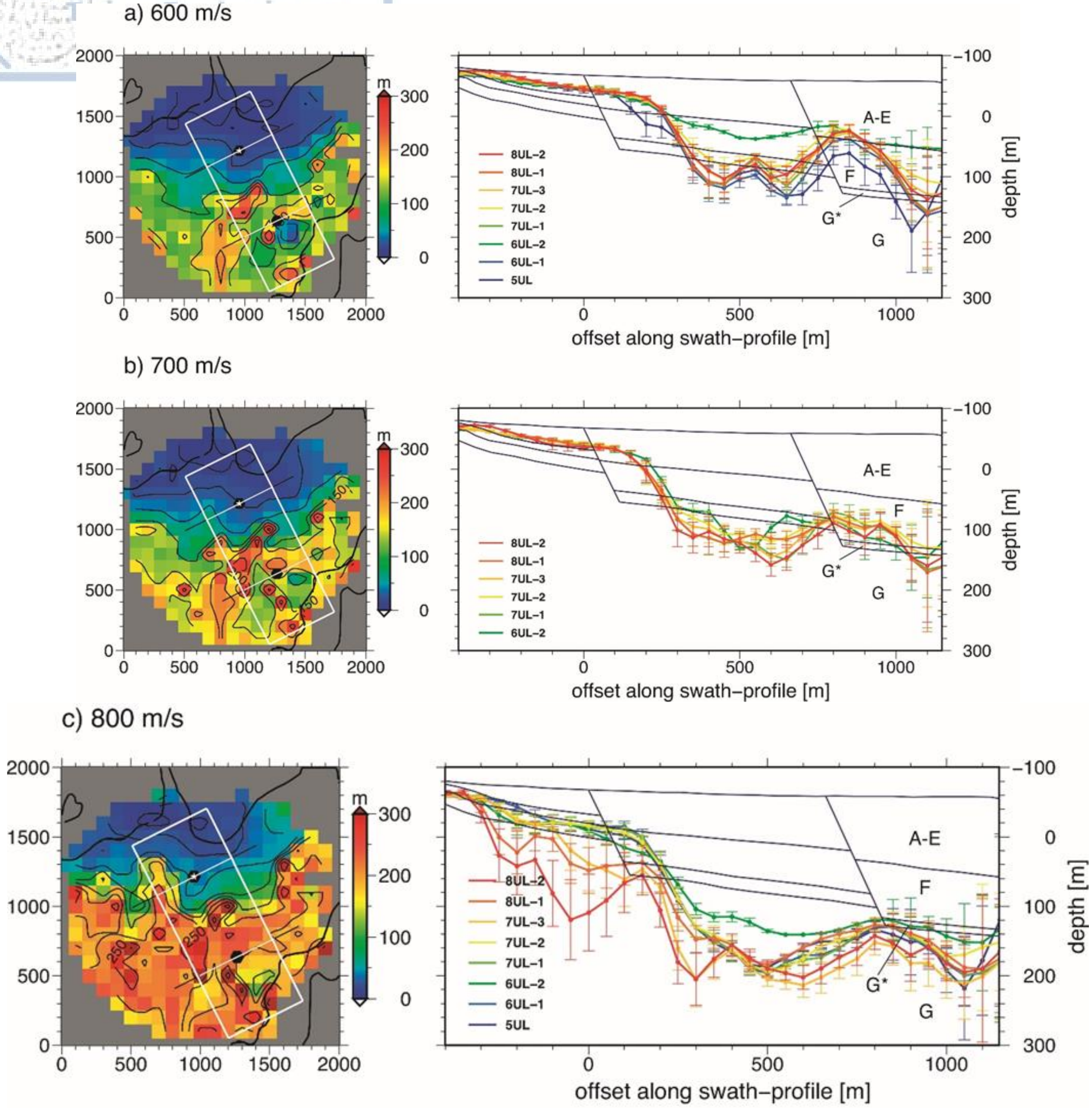


***Figure 13.*** Left: Spatial variation of average interface depths for seven layer velocities (Vs = 150, 250, 350, 425, 600, 700 and 800 m/s) from all model parameterizations adopted by *Hannemann et al. (2014)* to invert reconstructed Rayleigh wave group slowness dispersion curves, presented in Table II and discussed in the text. The white polygons indicate the area that was used for the computation of the average interface depths, while black polygons depict the surface positions of faults F1 and F2. Right: Depth variation of the averaged bottom interfaces for the seven Vs layers employed for the various model parameterizations presented in Table II and discussed in text (from *Hannemann et al., 2014*).

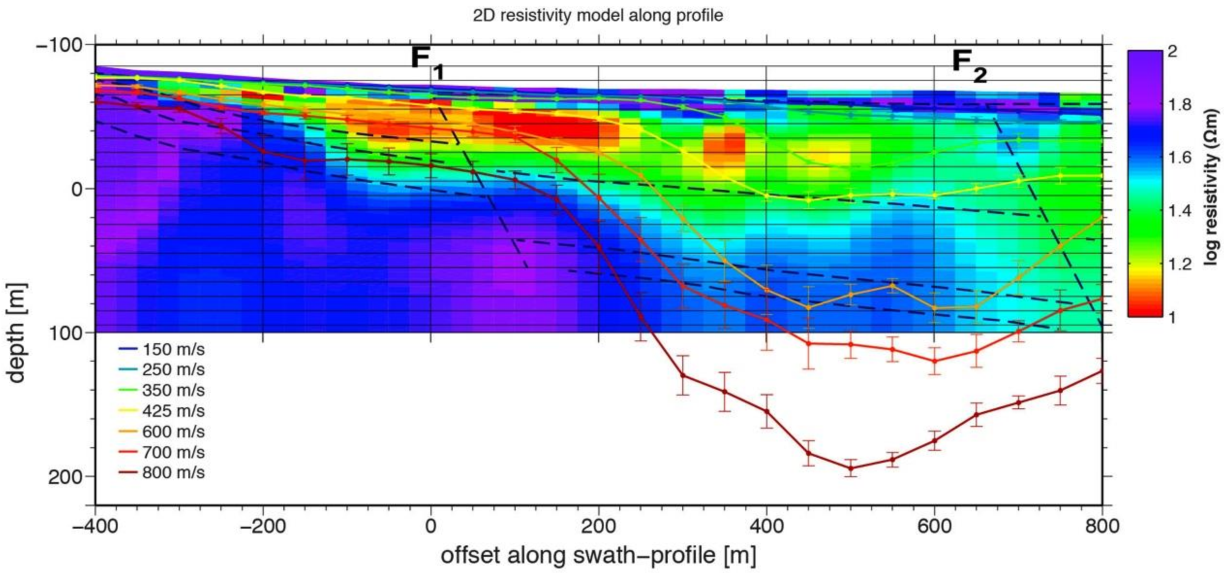


***Figure 14.*** Cross-section derived from cross-correlation ambient noise tomography of Rayleigh wave group traveltime for the study area. The magneto-telluric results (*Autio et al., 2016*) for the same area are also depicted using a logarithmic color scale, while the E/F, F/G*, G*/G discontinuities and the two neotectonic faults, F1 and F2, from *Raptakis et al. (2010)* are also shown with dashed lines (modified from *Hannemann et al., 2014*).

# CHAPTER 2 – METHODOLOGY

## 2.1 Surface Waves

### 2.1.1. Generation and Propagation

If we consider a homogeneous and isotropic medium, the application of a tensional force in its mass will result in the generation of body waves, namely P and S waves. The P waves (or primary waves) correspond to wave propagation in a parallel direction with this tensional force, while S waves (or secondary waves) involve wave oscillation in the plane which is perpendicular to P wave propagation direction (see Figure 15). The propagation of P waves, which travel faster than S waves, involves the generation of local compressions and dilatations in the considered medium, while the propagation of S waves corresponds to the propagation of shear deformation. S waves are usually analyzed in two components, the horizontal SH component and the vertical SV component (Figure 15). Body waves from earthquakes typically arrive first, before all other types of waves and are recorded in seismograms, with P waves recognized primary in the vertical component and S waves in the horizontal components (North-South and West-East). However, recordings of long-distance seismic events are typically dominated by the presence of longer period waves with higher amplitudes, arriving after the S wavetrain. Those waves, whose energy propagates mainly in the shallow layers of the earth’s crust, are surface waves, namely the Rayleigh and Love waves.

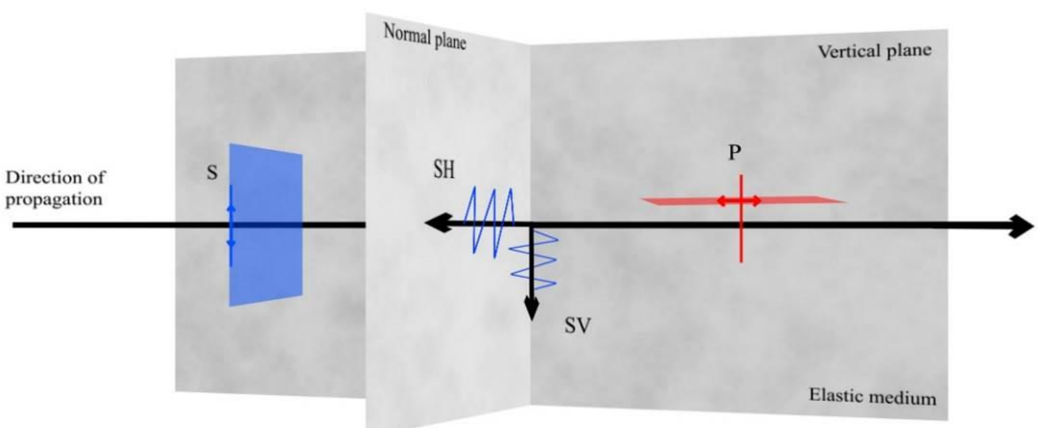


***Figure 15.*** Schematic propagation of body (P and S) waves.

In an isotropic medium Rayleigh waves propagate along a vertical plane and are generated due to the interference of the motions of P and SV waves (Figure 16). Let us assume a SV wave incidence to the free surface (for example the earth’s surface) with an angle lower than the critical angle of an incident P wave or at the critical angle (incidence angle which would result in a P wave horizontal propagation through the surface). The interference of these waves, without any interaction with the SH waves, gives rise to the generation of Rayleigh waves, which, due to the phase shift between P and SV waves, propagate in reverse elliptical orbits. Those elliptical orbits are characterized by a significant amplitude decay with depth, corresponding to the energy "trapping" observed for these waves in the shallow layers of earth's crust. It is interesting to notice that Rayleigh waves can propagate even in a homogeneous half-space medium, due to their generation from the interaction of P-SV waves along the half-space free surface.

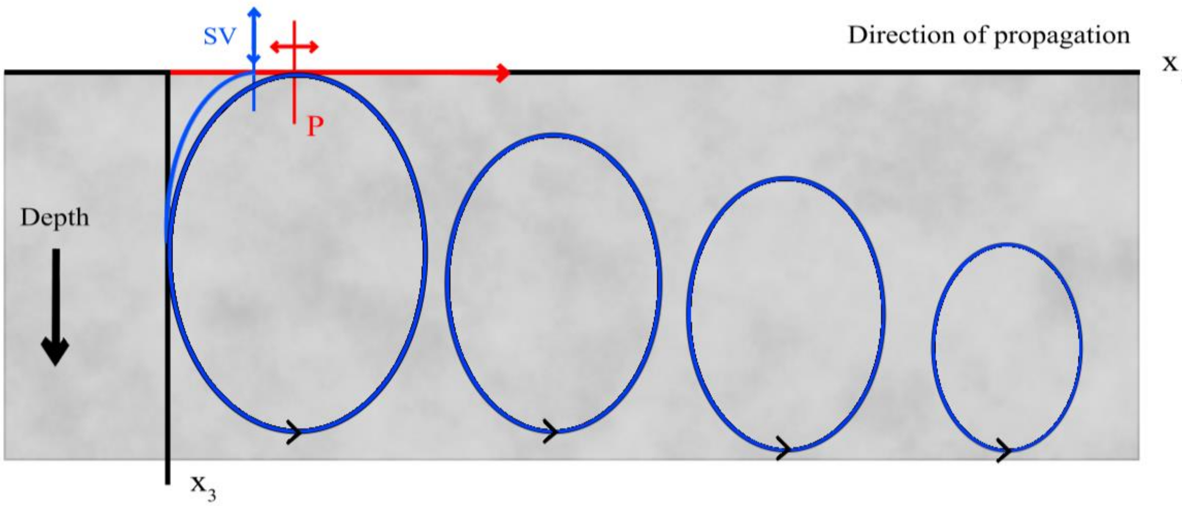


***Figure 16.*** Superposition of P and SV waves propagating in a homogeneous medium and generation of Rayleigh surface waves, propagating in elliptic orbits (modified from *Lay and Wallace 1995*).

Love waves propagate along the horizontal plane and are generated (in the simplest case) by the superposition of SH waves trapped in a layer over a halfspace. In contrast to the propagation of P and SV waves, SH waves convert only to SH waves upon their incidence on a set of layers (Figure 17). As earlier noted, the generation of Love waves involves the existence of a layer with significant contrast between its physical properties and the underlying halfspace, also bounded by a free surface. The incident SH waves (and their energy) are trapped in this layer, resulting in the generation of a superimposed set of SH waves, a Love wave travelling in the horizontal direction.

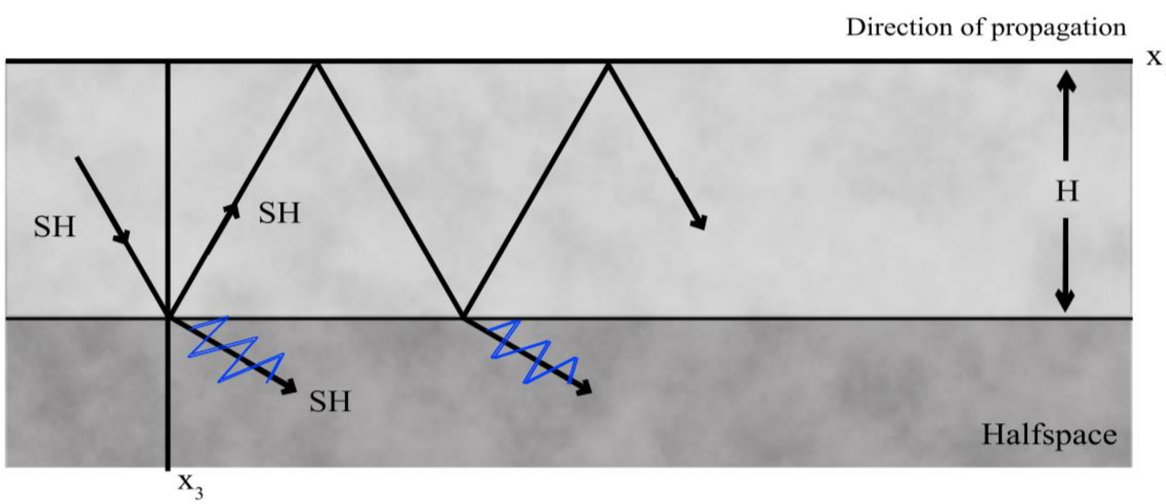


***Figure 17.*** Generation of Love surface waves from the superposition of SH waves propagating in a layer with thickness H, above a halfspace (modified from *Lay and Wallace 1995*).

### 2.1.2. Dispersion

An important property of the surface waves is that they are dispersive, which means that different periods (or wavenumbers) travel with different velocities. To demonstrate this behavior, let us assume the simplest case of two harmonic waves, propagating in a medium with slightly different angular frequencies, $\omega_1$ and $\omega_2$, which are close to a dominant angular frequency, $\omega$ (equal to $2\pi f$, where f is the dominant frequency) and different wavenumbers, $k_1$ and $k_2$, close to the dominant wavenumber, k. The interaction of these two harmonic waves results in the generation of a wave with displacement, u(x,t), given by:

$$u(x,t) = 2\cos(\omega t - kx)\cos(\delta\omega t - \delta kx) \qquad \delta\omega <<< \omega,\ \ \delta k <<< k \tag{2.1}$$

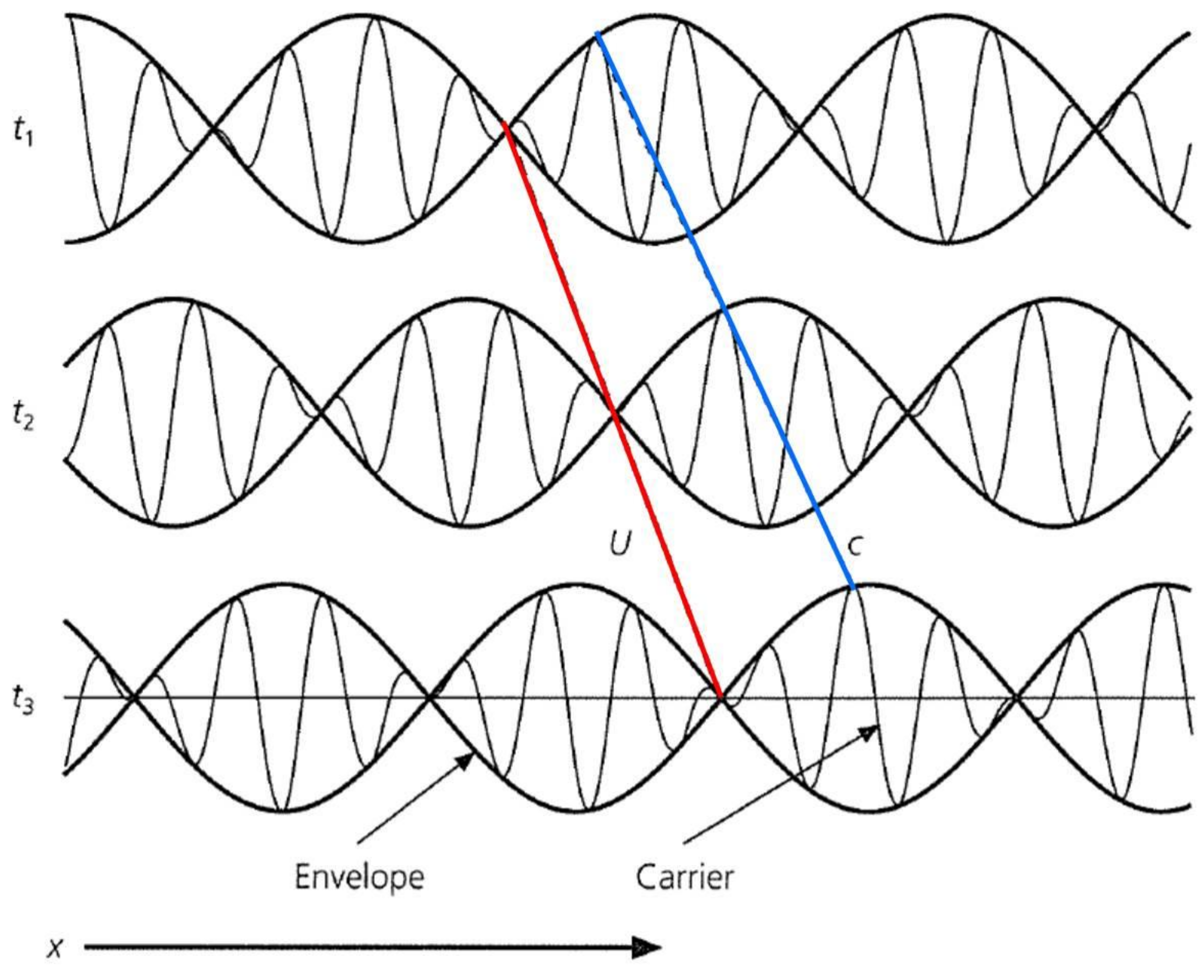


***Figure 18.*** Carrier and envelope functions of a dispersive harmonic wave travelling towards the +x direction in three different time snapshots. The phase and group velocities, c and U, are denoted with blue and red lines, respectively (modified from *Stein and Wysession 2003*).

The two cosine functions of equation 2.1 correspond to two harmonic waves, propagating with different velocities and phases. The second term corresponds to a harmonic wave propagating much slower than the first, both in space and time, because the terms δω and δκ are typically much smaller than ω and κ. Therefore, we have a carrier wave propagating faster in both space and time than its envelope function, expressed as the first and the second cosine terms of equation 2.1. When the phase of the propagation of these two functions remains constant, a snapshot of the resulting wave shows that both the carrier and the envelope describe waves propagating with different speeds (see also Figure 18). The speed of the oscillating carrier (first term in equation 2.1) is called **phase velocity, c,** describing its rapid variation of the signal in both space and time. The speed of the envelope function corresponds to the energy maxima of the travelling wave, the circumferential of all carriers and its velocity is called **group velocity, U**. From equation 2.1, the phase velocity can be written as:

$$c = \frac{\omega}{\kappa} \tag{2.2}$$

while the group velocity, U, also from equation 2.1 can be expressed as:

$$U = \frac{d\omega}{d\kappa} \tag{2.3}$$

which is the derivative of equation 2.2 with respect to the wavenumber, κ.

The phase velocity, depicted with a blue line in Figure 16 inside the carrier function, bisects the travelling waves at phases which vary quick in space and time. The group velocity (red line in Figure 18), bisects the envelope function at the energy maxima points of wave propagation. Considering the slope of the two dashed lines in Figure 16, it is clear that the slope of the phase velocity is (in general) expected to be smaller than the slope of the group velocity, suggesting that phase velocities of harmonic waves tend to be bigger than group velocities.

The formulation presented in Figure 18 and equations 2.2 and 2.3 is widely employed for surface waves. However, if we assume a normal velocity increase with depth for the earth’s interior, surface waves of larger periods (or equivalently larger wavelengths), that penetrate deeper earth’s formations, tend to have larger phase and group velocities. In contrast, surface waves of smaller periods (also smaller wavelengths), tend to have smaller phase and group velocities, as they “sample” shallower earth layers (e.g. soft sediments and other upper crustal rocks etc.).

### 2.1.3. Deviations from elasticity and isotropy

#### 2.1.3.1. Anelasticity

For most studies and applications, seismic wave propagation is considered for the case of elastic, isotropic and homogeneous layers. However, the earth’s interior comprises of complex structures, therefore wave propagation takes place within anelastic, inhomogeneous and sometimes anisotropic media. While the variability of wave propagation phenomena (wave amplitudes, seismic ray incidence angles, etc.) is controlled by the elastic properties of the medium (i.e. seismic velocities), energy loss is caused by the medium anelasticity. To illustrate the effect of anelasticity, we first consider the case where stress is applied in an elastic material, where the relation between stress and strain is linear (Hooke's law, Figure 19 left). In the case of anelastic behavior, the relation between stress and strain is non-linear and the path of deformation is shown in right plot of Figure 19. In this case, energy is consumed during every loading-unloading cycle, with the total area defined by the "sigmoidal" stress-strain path being equal to the total consumed energy, ΔE. This does not occur in the case of elastic material, since when stress is removed strain return to its initial position (zero value) without any energy loss (along the linear stress-strain path, Figure 19 left).

When seismic waves propagate through the earth's interior, there is a significant amount of energy loss, either due to geometrical spreading (elastic phenomenon) or anelastic attenuation (anelastic phenomenon). Geometrical spreading refers to the amount of energy loss due to the spread of seismic energy in a bigger surface as it propagates, in a manner consistent to the energy loss of light rays radiated from lightning fixtures. More specifically, assuming uniform radiation of seismic waves from their source, as the distance, r, from their source increase with time, so does the area of the wave-front and the total energy decay is proportional to $r^{-2}$.

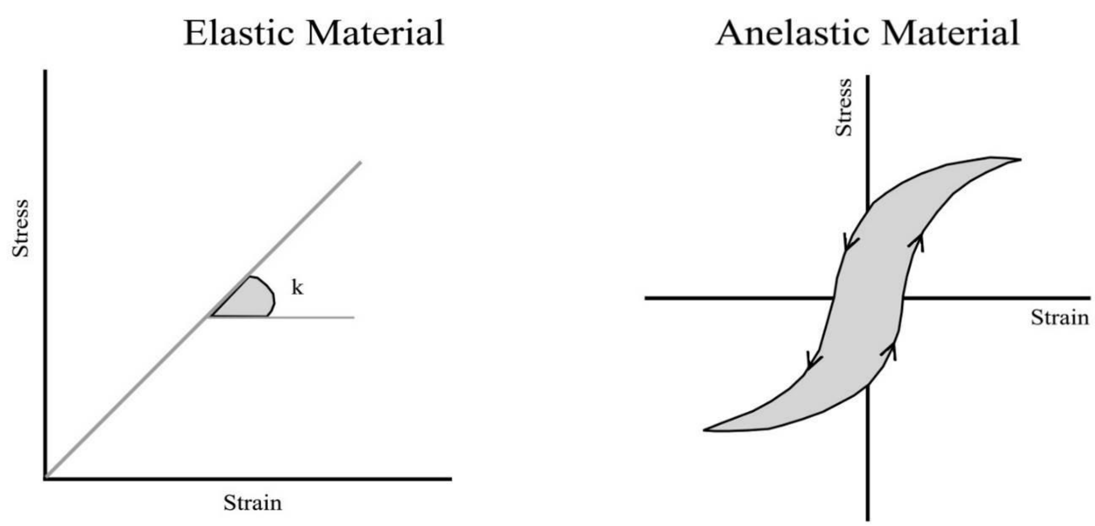


***Figure 19.*** Stress-strain schematic models for elastic (left) and anelastic (right) behavior of materials. The slope of the left (linear) relation corresponds to Hooke's constant, while the shaded area in the right plot is proportional to the energy consumption during its loading-unloading cycle (ΔE).

In the anelastic case, a fraction of the seismic waves' kinematic energy is mainly transformed into heat (possibly also some other energy forms) due to the structure (e.g. internal friction) of the propagating medium. In the simplest case of wave propagation in a homogeneous medium, if $A_0$ is the initial amplitude of seismic waves radiated from the seismic source, the decay of the signal's envelope, or overall amplitude with time, is expressed as an exponential function of the form:

$$A(t) = A_0 e^{\frac{-\omega_0 t}{2Q}} \tag{2.4}$$

The term Q in equation 2.4 is the quality factor, which depends on the material and its physical properties of the material, such as temperature, compaction rate, presence of water and several others. This complicated dependency makes the interpretation of the nature of the real attenuation mechanism quite difficult, especially if we consider the data uncertainties and the estimation of other parameters affecting the modeling of attenuation (e.g. geometrical spreading). Moreover, the attenuation of S waves is usually higher than the attenuation of P waves, due to the consumption of large energy amounts by the medium's shear deformation or the stronger effect of fluids and gasses on S velocities.

2.1.3.2. Anisotropy

Usually for most geophysical applications the earth's materials are treated as isotropic, considering that their physical properties are azimuthally independent. However, several theoretical and experimental studies have demonstrated that properties such as seismic wave velocities or the magnetic susceptibility of earth's minerals and layers tend to vary with their orientation in space. Considering the anisotropic behavior of these materials, we can extract other useful information about the earth's structure, such as the fabric of the studied layers. In general, there are two main types of seismic anisotropy, namely mineral anisotropy and formation anisotropy.

The mineral or rock anisotropy is the effect of directionality in the fabric of rocks or minerals. Due to this alteration in their internal structure, seismic waves oscillating parallel to specific crystallographic axes of these materials tend to propagate with different velocities, usually along an axis with faster velocities and an axis with slower velocities, compared to the average velocity that the waves would propagate if the material was isotropic. A characteristic example is the mineral of olivine, which is extremely anisotropic. Experimental studies have shown that P waves propagating parallel to the [100] axis of olivine are much faster than the average P wave velocity of olivine. The same axis tends to orient parallel to the direction of lithospheric plates' motion. Therefore, identification of the direction of fast P-wave velocity propagation in the earth's mantle allows the use of mineral anisotropy as an index to study lithospheric plate motions. Figure 20 presents the spatial variation of the lattice preferred orientation (LPO) of olivine/enstatite inferred from the SKS seismic phase waves splitting (Becker et al., 2014), showing the anisotropic fabric of the earth's mantle at the depth of 150 km.

Several phenomena associated with the petrogenesis of rocks in the earth's crust can also produce anisotropy. Sedimentary deposits can behave as anisotropic due to their 3-D complex depositional geometry. Also, the foliation of metamorphic rocks, such as gneiss and schists is a source of anisotropy for these formations. Therefore, seismic waves oscillating parallel to the strike of the foliation or the layering of these geologic formations tend to propagate faster than those oscillating normal to these planes/surfaces, generating complex spatial forms of seismic velocity anisotropy.

Usually, large-scale sedimentary formations consist of a series of layers with different composition, depositional conditions, structure and mechanical properties. Their most common form of anisotropy is called transverse anisotropy and is quite frequently observed in the earth's crust. In practice, SH waves which oscillate parallel to the sedimentary layering are faster than the perpendicular SV component. Theoretically, these components can be constrained by the Love and Rayleigh waves. Another form of anisotropy is the case of seismic wave velocity variations in the horizontal plane, usually termed as azimuthal anisotropy. The study of azimuthal anisotropy can be performed using either body waves (P and S) or surface waves (Rayleigh and Love), thought it usually requires dense data coverage to resolve the ambiguity between velocity variations and anisotropy.

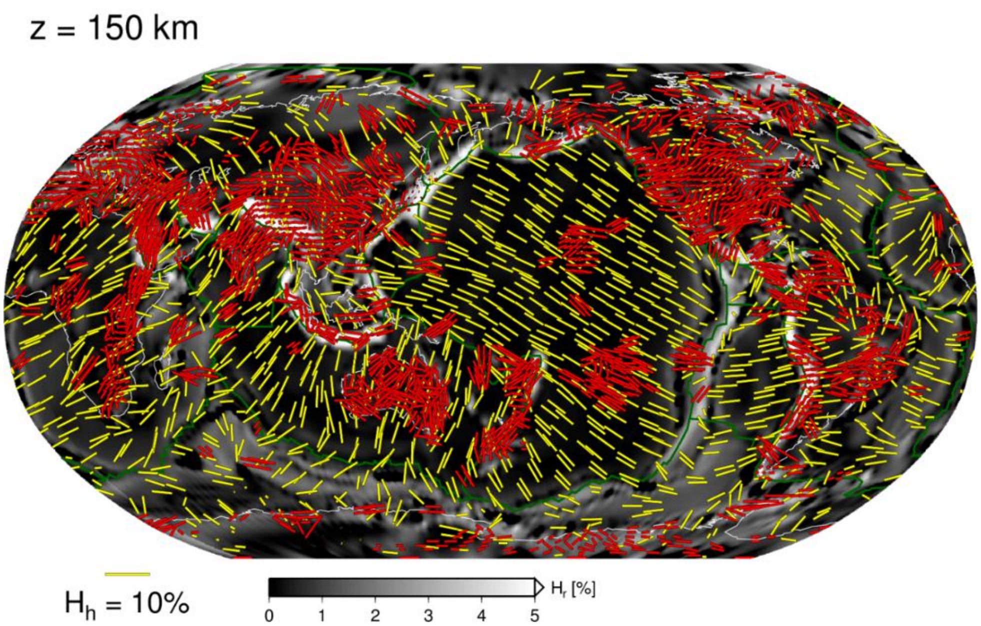

***Figure 20.*** Azimuthal (radial) anisotropy of the earth's mantle at the depth of 150 km, inferred from SKS splitting (from *Becker et al. 2014*).

## 2.2. Ambient noise

### 2.2.1. Nature and sources of ambient noise

Ambient noise is the superposition of low-amplitude ambient vibrations of the earth's shallow layers that are usually recorded at seismic stations. These vibrations exhibit a stochastic spatio-temporal variation, with amplitudes of about $10^{-2}$ - $10^{-4}$ mm and therefore are not felt by humans, nor cause damage to infrastructure. In most cases, where active seismic sources are employed in Geophysics, they are treated as seismic "noise", since their presence distorts the waveform due to the superposition of ambient vibrations and the (active source) seismic waves signals. Ambient noise consists mainly of surface waves, as shown in the pioneering work of Aki (1957), hence their decay with depth is significant, as discussed for surface waves. As a result, the maximum penetration depth of these vibrations depends on their wavelength, which varies with the nature of the surface waves generated by ambient noise sources.

The ambient vibrations source uncertainties make their modelling quite difficult. Ambient vibration recordings are usually employed for the study of the earth's structure. The corresponding techniques have recently seen significant development (typically referred to as passive source techniques), since the cost and environmental impact of generating seismic waves signal from the conventional active seismic sources is eliminated. Despite the involved uncertainties, the correlation between generated ambient vibrations and specific natural sources has been demonstrated in several cases, such as the example of Figure 22. In their work, Rhie and Romanowicz (2004) have shown a strong correlation between stacked amplitudes of daily recorded ambient noise with a small number of earthquakes and significant ocean wave heights for winter and summer of the year 2000 (northern hemisphere). Their results indicate that more than 85% of the maximum amplitude recordings depends on the interaction between ocean surface, bottom and atmosphere for winter periods (northern and southern hemisphere, respectively).

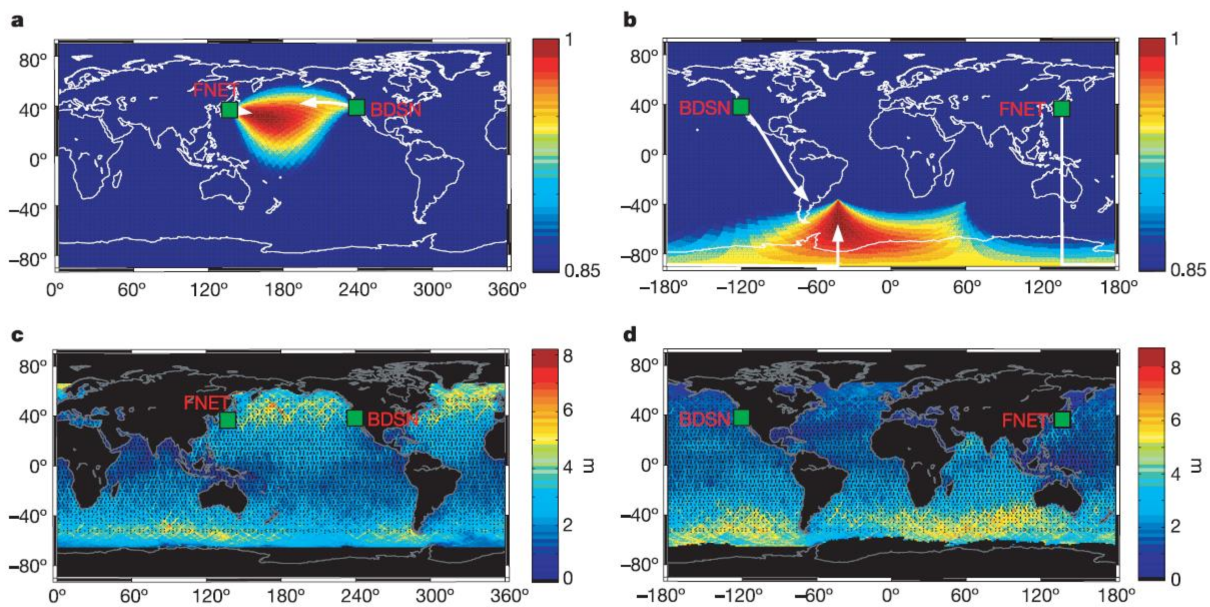


***Figure 21.*** Correlation of stacked amplitudes of ambient noise recordings for winter (a) and summer (b) periods and significant ocean wave height for the same time period (c and d respectively) for the year 2000 (from *Rhie and Romanowicz 2004*).

Noise sources are not only natural (e.g. ocean waves, volcanic tremor etc.) as earlier described, but also anthropogenic (e.g. drilling activities, vehicles etc.) which generate vibrations in different frequency bands. However, the true origin of ambient noise is still enigmatic. Usually, vibrations with frequencies lower than 1 Hz are called microseisms and above 1 Hz microtremors (Seo 1997). Furthermore, noise generated from anthropogenic activities tends to generate waves with relatively high frequencies (short periods), while noise generated from natural sources is mainly dominated by high frequencies or long periods (Gutenberg, 1958; Asten, 1978; Asten and Henstridge, 1984; Bennefoy-Claudet et al., 2006). Seo (1997) suggested that the frequency band of the generated ambient vibrations is affected by the source depth, recording time (day or night), the variation of recorded amplitudes and the area of the recording.

Frequency bands of recorded signals from different noise sources are summarized in Table II (Bennefoy-Claudet et al., 2006). According to this classification, natural noise sources produce waves with a low frequency content, close to the 1 Hz limit, while urban ambient noise sources (human activities, such as vehicles, drilling, etc.) generate waves with higher frequencies.

| Source | Gutenberg (1958) | Asten (1978, 1984) |
|---|---|---|
| **Ocean waves** | **0.05 - 0.1 Hz** | **0.5 - 1.2 Hz** |
| **Monsoon** | **0.1 - 0.25 Hz** | **0.16 - 0.5 Hz** |
| **Cyclones over the oceans** | **0.3 - 1 Hz** | **0.5 - 3 Hz** |
| **Local scale meteorological conditions** | **1.4 - 5 Hz** | |
| **Volcanic tremor** | **2 - 10 Hz** | |
| **Urban ambient noise** | **1 - 100 Hz** | **1.4 - 30 Hz** |

***Table III.*** Comparison of frequency bands of ambient vibrations generated from various sources (from *Bennefoy-Claudet et al. 2006*).

The wave-field of ambient noise is complex, comprising of body (P and S) and surface waves (Rayleigh and Love), with random spatio-temporal variations. As earlier noted (Aki, 1957) ambient vibrations consist mostly of surface waves, therefore decay rapidly with depth and penetrate only shallow earth layers. The related research suggests that body waves phases (P, SV and SH) contribute lower amounts of energy in the total wave-field, while vertical and horizontal components seem to be dominated by Rayleigh and Love waves. Several researchers studied the wave content of ambient noise, in an attempt to distinguish the contribution of Rayleigh and Love waves. These studies suggest that Rayleigh waves dominate the noise wave-field of signals for frequencies lower than 1 Hz, while Love waves tend to dominate higher frequencies. Also, Tokimatsu (1997) showed that Rayleigh wave higher modes are also present (and sometimes dominate) in the noise wave-field and are highly affected by the Vs structure.

The wave content of ambient noise has been studied by several researchers. Bennefoy-Claudet et al. (2006) compiled all published results on the comparison of the contribution of Rayleigh and Love waves in the ambient noise wave-field, for several geologic settings. Their results indicate that for shallow sedimentary formations (with depths lower than 100m) and for frequencies lower than 1 Hz, Rayleigh waves dominate the wave-field. In contrast, for higher frequencies and significant depths of sedimentary deposits, Love waves are dominating the wave-field. Although this approach provides useful information on the composition of the noise wave-field, the results are limited to sedimentary deposits and do not cover a significant range of possible site geologic conditions (weathered rocks, presence of water, igneous / metamorphic bedrock etc.).

| Study | Frequency Band | Geology | Rayleigh | Love |
|---|---|---|---|---|
| Chouet et al. (1998) | >2 Hz | Volcanics | 23% | 77% |
| Yamamoto (2000) | 3 - 8 Hz | Sediments (thickness <100m) | <50% | >50% |
| Arai and | 1 - 12 Hz | Sediments (thickness <100m) | 40% | 60% |

| | | | | |
|---|---|---|---|---|
| Tokimatsu (1998) | | | | |
| Cornou (2002) | 0.1 - 1 Hz | Sediments (thickness ~500m) | 50% | 50% |
| Okada (2003) | 0.4 - 1 Hz | Sediments (thickness ~50m) | <50% | >=50% |
| Kohler et al. (2004) | 0.5 - 1.3 Hz | Sediments (thickness ~200m) | 10 - 35% | 65 - 90% |

***Table IV.*** Percentages of Rayleigh and Love surface waves in the ambient noise wave-field for different frequency bands and site geological conditions (from *Bennefoy-Claudet et al., 2006*).

## 2.2. Noise interpretation techniques

The techniques that exploit ambient vibrations to study the earth's structure can be divided in two categories, namely single-station techniques and array techniques.

Single station techniques use single-station recordings to study the ambient vibrations of shallow earth layers. A typical single-station method is the Horizontal to Vertical Spectral Ratio (HVSR technique) of ambient noise recordings (Nogoshi and Igarashi, 1971; Nakamura, 1989). This technique is a useful method. which can be used to study the resonance ground frequency, since the peak of the HVSR curve can be related to independent information provided by Rayleigh wave ellipticity (Bennefoy-Claudet et al., 2006). The H/V ratio depends on the percentage of Rayleigh waves in the wave-field of the recordings and the different acoustic impedances of underlying sediments and the bedrock. Also, the HVSR technique is a useful tool to understand the local site effects using data from a single recording station. A rough approximation is that the depth, H, of the sedimentary deposits above the bedrock, depends on the average shear seismic wave velocity, Vs, of the sediments and their resonance frequency, $f_0$, using the following relation:

$$h = \frac{V_S}{4 f_0} \tag{2.5}$$

Another form of noise interpretation is based on methods that employ ambient noise recordings from two or more recording stations (arrays). Two of the most common array techniques are SPAC (Aki 1957) and f-k (Lacoss et al., 1969; Capon, 1969). Both methods rely on the reconstruction of the surface wave dispersion curves, in order to determine the Vs variation with depth, employing recorders installed in random (F-K) or semi-circular arrays (SPAC). An alternative method for ambient noise vibration processing is based on the cross-correlation of noise recordings between two stations (e.g. Gouedard et al., 2008). If A and B are the recording stations, the cross-correlation of the ambient vibrations, $C_{AB}$, can be expressed as (e.g. Cuppilard et al., 2011):

$$C_{AB}(t) = \sum_{P-P'} \int A_P(t_A + t) B_P(t) dt_A \tag{2.6}$$

where AP is the signal of noise source P recorded at station A at time delay $t_A$, with respect to the recording at station B. In equation 2.6 P and P' describe the superposition of all seismic noise sources that produce noise waves which are recorded by the two stations. Ambient vibrations generated from a single source, P, can also be correlated, leading to:

$$C^{P}_{AB}(t) = \int A_P(t_A + t) B_P(t) dt_A \quad (2.7)$$

A schematic illustration of this concept is shown in Figure 22, where a band of noise waves is generated from a source and is being recorded at stations A and B, with a time difference of Δt. Using the Fourier theorem, we can compute the cross-correlation in the frequency domain as:

$$C_{AB}(t) \Leftrightarrow A(\omega) * B(\omega) \quad (2.8)$$

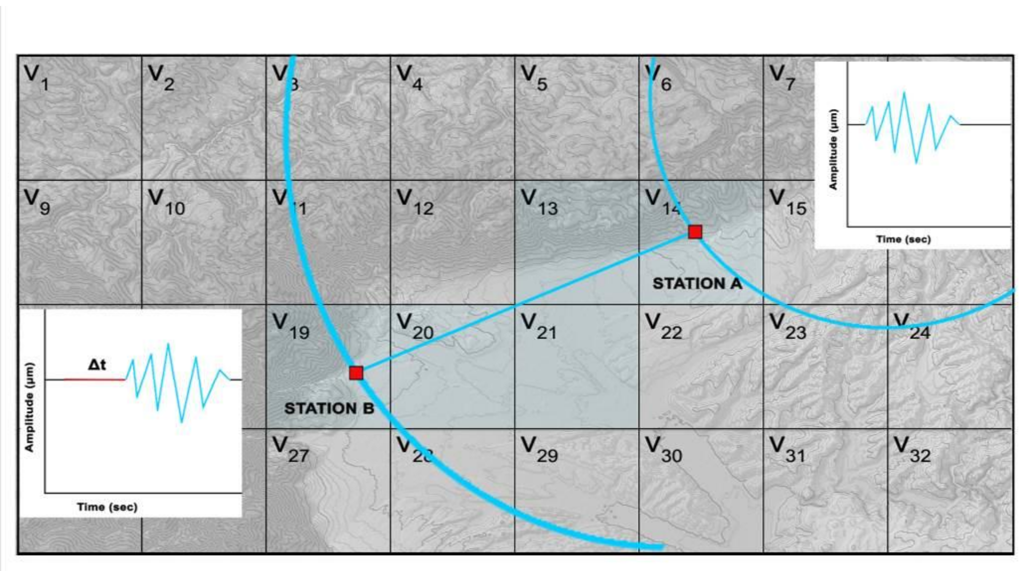


***Figure 22.*** Illustration of an ambient noise wavetrain generation from a single source and its recording at stations A and B with a time delay Δt.

Moreover, it is well known (e.g. Lin et al., 2013) that the cross-correlation of noise recordings can be related to the Green's function between points A and B, $G_{AB}$ and $G_{BA}$, of the medium of propagation in the time domain as:

$$\frac{dC_{AB}(t)}{dt} = -G_{AB}(t) + G_{BA}(-t) \quad -\infty < t < \infty \quad (2.9)$$

implying that the cross-correlations (negative and positive time lags) of ambient vibrations are the derivative of the medium's Green's functions, hence they can be used to study its geophysical structure.

## 2.3. Inversion theory

### 2.3.1 Fundamentals

Geophysical problems are usually classified in two groups, namely the forward and inverse problems. Forward problems correspond to the generation of synthetic geophysical data, d, (various measurable geophysical quantities such as seismic travel-times, intensity of the gravity or magnetic field, etc.) for a known earth's structure, m. Inverse problems correspond to the determination and modelling of the unknown earth's structure (and its uncertainties) from the available measured data, as well as their errors. Usually the forward modelling relation is written as:

$$d = G(m) \tag{2.10}$$

where G denotes the functionals that relate the model functions, m, with the data measurements, d. The determination of the earth's physical properties, m, that we would like to study is called model parameterization and is of critical importance for the selection of the appropriate function that best describe these parameters. Functionals G are generally non-linear and can be employed to generate the expected data values, d, once we know the actual (real) model parameters.

The inversion theory is a set of theoretical and numerical methods, which are used to solve the inverse problems. Besides the model solution, the methods also consider the uncertainties of data and attempt to derive the model errors, while trying to also assess the non-uniqueness of the solution. If the forward problem can be solved and $d_i$ (i=1,…,N) is a set of all available (discrete) data that we have acquired to study the earth's geophysical structure, if we assume that this structure can be described by a discrete set of model parameters, $m_j$ (j=1,…,M), then the corresponding synthetic data equations can be written as:

$$d_i = G_i(m_1, m_2, ..., m_M) \qquad i = 1, \dots, N \tag{2.11}$$

If the functionals $G_i$ are linear, equations 2.11 can be re-written in a matrix form:

$$\mathbf{Gm} = \mathbf{d} \tag{2.12}$$

For equation 2.12 the N unknowns (model parameters) can be determined using the standard Least Squares solution, which minimizes the norm between real and synthetic data (i.e. $|Gm-d|^2 \rightarrow \mathit{min}$):

$$\mathbf{m}^{\mathbf{LSQ}} = (\mathbf{G}^{\mathbf{T}}\mathbf{G})^{-1}\mathbf{G}^{\mathbf{T}}\mathbf{d} \tag{2.13}$$

### 2.3.2. Iterative Least Squares solution of non-linear inverse problems

In general, the functionals G in equation (2.11) are non-linear for most geophysical problems. For such non-linear problems, the solution typically employs an iterative procedure, with successive solutions of the forward and inverse problems. Initially, model parameters are described by adopting an *a-priori* model, $m_0$. Then, the forward problem is solved for this model and synthetic data, $d_i^0$, are calculated:

$$d_i^0 = G_i(m_1^0, m_2^0, ..., m_M^0) \qquad (i=1, \ldots, N) \tag{2.14}$$

The Taylor series expansion of equation 2.14, around the *a-priori* model, $m^0$, leads to:

$$d_i = G_i(m_1^0, m_2^0, ..., m_M^0) + \sum_{j=1}^{M} \left.\frac{\partial G_i}{\partial m_j}\right|_{m_j^0} (m_j - m_j^0) + (\textit{higher order terms}) \qquad (i=1,\ldots,N) \tag{2.15}$$

If the *a-priori* model is close to the real model, then the higher order terms in equation 2.15 can be considered to be small compared to first order term ($\left|m_j - m_j^0\right| << 1$ j=1, ..., M), and therefore can be neglected. In this case, the differences between real and synthetic data, $\delta d_i = d_i - d_i^0 = d_i - G_i(m_1^0, m_2^0, ..., m_M^0)$, from equation 2.15 can be written as:

$$\delta d_i \cong \sum_{j=1}^{M} \left.\frac{\partial G_i}{\partial m_j}\right|_{m_j^0} \delta m_j \qquad j=1, \ldots, M \tag{2.16}$$

Equation 2.16 can be also written in a matrix form as:

$$\delta\mathbf{d} = \mathbf{A}\delta\mathbf{m} \tag{2.17}$$

where $\delta\mathbf{d}$ and $\delta\mathbf{m}$ are column vectors, containing the differences between observed and synthetic (model) data, and final and *a-priori* model parameters, respectively:

$$\delta\mathbf{d} = \begin{bmatrix} d_1 - d_1^0 \\ d_2 - d_2^0 \\ \ldots \\ d_N - d_N^0 \end{bmatrix} \qquad \delta\mathbf{m} = \begin{bmatrix} m_1 - m_1^0 \\ m_2 - m_2^0 \\ \ldots \\ m_M - m_M^0 \end{bmatrix} \tag{2.18}$$

The partial derivatives of the linear functionals, G, with respect to model parameters, $m_j$, represent the sensitivity of each linearized equation (datum) to each parameter. The matrix **A**, containing these derivatives is called Jacobian, and can be written as:

$$\mathbf{A} = \begin{bmatrix} \left.\frac{\partial G_1}{\partial m_1}\right|_{m_1^0} & \left.\frac{\partial G_1}{\partial m_2}\right|_{m_2^0} & \cdots & \left.\frac{\partial G_1}{\partial m_M}\right|_{m_M^0} \\ \left.\frac{\partial G_2}{\partial m_1}\right|_{m_1^0} & \left.\frac{\partial G_2}{\partial m_2}\right|_{m_2^0} & \cdots & \left.\frac{\partial G_2}{\partial m_M}\right|_{m_M^0} \\ \cdots & \cdots & \cdots & \cdots \\ \left.\frac{\partial G_N}{\partial m_1}\right|_{m_1^0} & \left.\frac{\partial G_N}{\partial m_2}\right|_{m_2^0} & \cdots & \left.\frac{\partial G_N}{\partial m_M}\right|_{m_M^0} \end{bmatrix} \tag{2.19}$$

For most geophysical problems, the available collected data are more than model unknowns (N > M), hence the linear system 2.17 is over-determined for these cases and can be solved by implementing a least-squares' solution approach. The least squares' solution of the for the model corrections, δ**m**, can be computed as:

$$\delta\mathbf{m}^{\mathbf{LSQ}} = (\mathbf{A}^{\mathbf{T}}\mathbf{A})^{\mathbf{-1}}\mathbf{A}^{\mathbf{T}}\delta\mathbf{d} \tag{2.20}$$

Since higher order terms are omitted from equation 2.16, equation 2.20 needs to be solved iteratively. Hence, the derived model corrections, $\delta\mathbf{m}^{LSQ}$, are applied in an iterative manner:

$$\mathbf{m} = \mathbf{m}^0 + \delta\mathbf{m}^{LSQ} \tag{2.21}$$

Since, the synthetic data can be computed as:

$$\mathbf{d}' = \mathbf{Am} \tag{2.22}$$

where **m** is the final least-squares solution, the difference between real and synthetic data can be evaluated by the Root Mean Square (RMS) error, which approximates the input data average error, *σ*, if we assume that data errors are uncorrelated. This RMS error can be computed as:

$$\mathrm{RMS} = \sqrt{\frac{\sum_{i=1}^{N}(d - d')^2}{N - M}} \tag{2.23}$$

Using the $RMS^2$ as an estimate of the data variance, $\sigma^2$, the model parameter uncertainties can be estimated by the model variance-covariance matrix, $\mathbf{C_m}$, computed as:

$$\mathbf{C_m} = \sigma^2(\mathbf{A^T A})^{\mathbf{-1}} = \begin{bmatrix} \sigma^2{}_{11} & \sigma^2{}_{12} & \cdots & \sigma^2{}_{1M} \\ \sigma^2{}_{21} & \sigma^2{}_{22} & \cdots & \sigma^2{}_{2M} \\ \cdots & \cdots & \cdots & \cdots \\ \sigma^2{}_{M1} & \sigma^2{}_{M2} & \cdots & \sigma^2{}_{MM} \end{bmatrix} \tag{2.24}$$

which contains the model parameters variances along its diagonal elements.

If we consider that the inversion model, **m'**, from equation (2.13) or (2.20) (whether it is the model itself or its corrections) is a linear function of the data, **d**, which are themselves (or their perturbations) also a linear of the real model parameters, **m**, then the predicted (the solution of the inverse problem) model parameters, **m'**, can be written as:

$$\mathbf{m'} = \mathbf{Rm} \tag{2.25}$$

where **R** is called the model resolution matrix. In the case of the least squares solution (equations 2.12 and 2.13 or 2.17 and 2.20) , matrix **R** is easily computed as:

$$\mathbf{R} = (\mathbf{A}^{\mathbf{T}}\mathbf{A})^{-1}\mathbf{A}^{\mathbf{T}}\mathbf{A} = \mathbf{I} \tag{2.26}$$

which means that the real model is (in principle) properly resolved by the least-squares solution.

2.3.3. Solution stability constrains

In several cases, the matrix $\mathbf{A^TA}$ in equation 2.20 is ill-conditioned, i.e. its determinant, $|\mathbf{A^TA}|$, is close to zero. Since $(\mathbf{A^TA})^{-1}$ is proportional to $|\mathbf{A^TA}|^{-1}$ (from Kramer's rule), when $|\mathbf{A^TA}| \rightarrow 0$ the model perturbations determined from equation 2.20 obtain unrealistically large amplitudes, while the corresponding errors (equation 2.24) also become very large. Typically, this behavior reflects the fact that the data derivatives (contained in the Jacobian matrix, **A**) are "almost" linearly dependent (at least for some of the data), which can be due to e.g. poor data geometry, or simply the non-uniqueness of the geophysical problem. In order to handle such issues, one approach is to determine the generalized inverse solution of the Jacobian matrix, from the singular value decomposition (SVD), i.e. define $\mathbf{A}=\mathbf{U\Lambda V^T}$, where **U** and **V** are appropriate left-orthogonal matrices sampling the data (**U**) and model (**V**) spaces and **Λ** contains the singular values of **A**, which are the positive square roots of the eigenvalues of $\mathbf{A^TA}$. In this case, the least-squares solution of equation 2.17 is given by:

$$\mathbf{m} = \mathbf{V\Lambda^{-1}U^Td} \tag{2.27}$$

The solution can be written as:

$$\mathbf{m} = \mathrm{v}_1 \frac{1}{\lambda_1}\mathrm{u}_1{}^{\mathrm{T}}\mathrm{d}_1 + \mathrm{v}_2 \frac{1}{\lambda_2}\mathrm{u}_2{}^{\mathrm{T}}\mathrm{d}_2 + \ldots + \mathrm{v}_N \frac{1}{\lambda_N}\mathrm{u}_N{}^{\mathrm{T}}\mathrm{d}_N \tag{2.28}$$

which is clearly controlled by the singular values of the Jacobian matrix, **A** (or the eigenvalues of $\mathbf{A^TA}$). As earlier noted, the presence of data which are partially independent leads to small eigenvalues of the $\mathbf{A^TA}$ matrix, hence to also small singular values, increasing the amplitude of the solution, as verified by equation 2.28 for small $\lambda_i$. To handle the instability of the solution, equation 2.12 is typically augmented, by using additional linear equations, which impose desired constraints on the solution. The most common approach is the damped least-squares solution, where the linear system is augmented as:

$$\begin{bmatrix} \mathbf{A} \\ \mathrm{d_c}\mathbf{I} \end{bmatrix} \mathbf{m} = \begin{bmatrix} \mathbf{d} \\ \mathbf{0} \end{bmatrix} \tag{2.29}$$

where $d_c$ is a Lagrange multiplier implemented in order to stabilize the solution, by obtaining a solution with minimum norm ($|\mathbf{m}|^2 \rightarrow$min), that also minimizes the differences between real and synthetic data ($|\mathbf{Am\text{-}d}|^2 \rightarrow$min). More specifically, the least squares solution of equation 2.28 minimized the quantity $|\mathbf{Am\text{-}d}|^2+d_c^2|\mathbf{m}|^2$ and is given by:

$$\mathbf{m} = (\mathbf{A}^\mathbf{T}\mathbf{A} + \mathrm{d_c}^2\mathbf{I})^{-1}\mathbf{A}^\mathbf{T}\mathbf{d} \tag{2.30}$$

In the damped least-squares solution the presence of the additional constant $d_c^2$ in the diagonal of $\mathbf{A^TA}$ controls the effect of small eigenvalues (and singular values) in the final solution and the derived model parameters (solutions) are restricted from obtaining large and unrealistic values. This is easily seen by considering the covariance matrix of the model solution, which for the damped least-squares solution becomes:

$$C_\mathbf{m} = \sigma^2(\mathbf{A}^\mathbf{T}\mathbf{A} + \mathrm{d_c}^2\mathbf{I})^{-1} \tag{2.31}$$

where the inverse matrix has a “normal” determinant, even when $|\mathbf{A^TA}|^{-1} \rightarrow 0$. However, this solution control is applied at the expense of reducing the resolving ability of the solution. Instead of a unit matrix (equation 2.26) for the simple least-square’s case the resolution matrix for the damped least-squares’ solution is computed as:

$$\mathbf{R} = (\mathbf{A}^\mathbf{T}\mathbf{A} + \mathrm{d_c}^2\mathbf{I})^{-1}\mathbf{A}^\mathbf{T}\mathbf{A} \tag{2.32}$$

where clearly $\mathbf{R}\neq\mathbf{I}$. If the resolution matrix is close to the identity matrix, **I**, then the model parameters are well resolved. When the resolution matrix non-diagonal elements are non-zero, then there are parameters which are not well resolved, and the distribution peaks of the resolution matrix elements are far from the bisector, i.e. the identity matrix, as seen in Figure 23.

Instead of damping, one can choose different additional constraints in equation 2.29, which produce solutions with different desired properties. In general, the optimal value of the Lagrange multiplier is hard to be determined in an objective manner. As discussed later (Chapter 3), the Lagrange multiplier is generally chosen to obtain a value that minimizes the trade-off between data error (e.g. RMS) and a model property (e.g. expressed by the model norm, |**m**|, in the case of damped least-squares). In several cases, the derived model solutions have rough spatial (or even temporal) variations. A typical approach is to obtain a solution that exhibits smoother model variations in space, by introducing spatial smoothing constrains which are applied to augment the linear equations 2.17, similar to equation 2.29. For example, in several cases we select the model that minimizes the data fit and also the second spatial derivative of the model, expressed by the Laplacian, solving the following system of equations:

$$\begin{bmatrix} \mathbf{A} \\ \lambda\nabla^2 \end{bmatrix}\mathbf{m} = \begin{bmatrix} \mathbf{d} \\ \mathbf{0} \end{bmatrix} \tag{2.33}$$

In this case, the inverse problem solution is given by the following equation:

$$\mathbf{m} = (\mathbf{A}^{\mathbf{T}}\mathbf{A} + \lambda^2(\nabla^2)^{\mathrm{T}}\nabla^2)^{-1}\mathbf{A}^{\mathbf{T}}\mathbf{d} \tag{2.34}$$

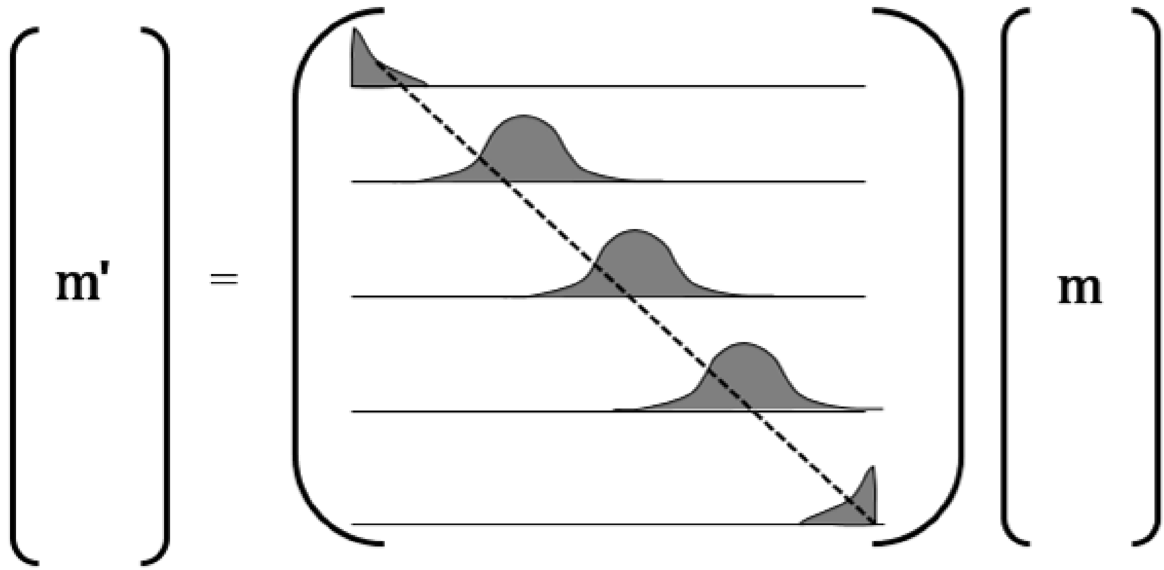


***Figure 23.*** Schematic illustration of the diagonal elements of the model resolution matrix, **R**. When model parameters are well resolved the peaks of the distributions are close to the dashed line (modified from *Menke 1989*).

The previous approach demonstrates how the inverse solution can be stabilized when the problem is ill-conditioned and how to obtain models (solutions) with desired properties, e.g. smooth variation of model parameters in space. Additional details on the damping and spatial smoothing constrains selection, as employed in the present thesis, are discussed in Chapter 3.

# CHAPTER 3 – TOMOGRAPHIC INVERSION OF LOVE WAVES FROM AMBIENT NOISE DATA IN THE MYGDONIA BASIN

## 3.1 Cross-correlation of ambient noise data

As earlier described (Chapter 1), the present thesis ambient noise data were obtained from the same temporary array that was installed in northern Mygdonia basin from Hannemann et al. (2014). This array consisted of 27 recorders installed in two circles; an outer circle with diameter ~1.8 km (black dots in Figure 11) and an inner circle with diameter ~0.7 km (colorful dots in Figure 11). The outer circle recorders remained stable during the operation of the network, while inner circle instruments were moved each day of the experiment. In particular, more than 78 recording sites are reported from the installation of 27 recorders (WARAN, Ohrnberger et al. 2006), after the two-week operational time of the network, recording 8-15 hours of ambient noise data per day and obtaining miniSEED (Standard for the Exchange of Earthquake data) files with more than 12 GB size. The data were sampled at 100 Hz, using 24 bit Guralp recorders and 5 sec sensors. Initially, raw data were pre-processed in order to improve the accuracy of the cross-correlations and to retrieve reliable information from the cross-correlated signals. After removing the instrument response, a Buttersworth filter was applied to remove effectively low and high frequencies. In this case, a lower limit of 0.5 Hz and a high frequency limit of 30 Hz was implemented. Also, cross-correlations of 90 sec windows of ambient noise recordings were stacked to increase the Signal to Noise Ratio (SNR) and stabilize temporal noise variations (Bensen et al. 2007).

The stacked cross-correlated signals were analyzed using the Frequency Time ANalysis (FTAN), to retrieve the slowness values for each frequency (Dziewonski et al. 1969) from each path of recorders. The cross-correlated signals were filtered with 6 Gaussian filters per octave, with each one having a range equal to the 25% of the central frequency. This approach filters the actual cross-correlation recording to slowness values for each frequency, while the global maxima points for each frequency correspond to the dispersion curve for each path of recording stations. For the computation of the correlation functions, each recording was shifted logarithmically with respect to each other and slowness values were computed for positive and negative time lags, stacked near a central time (t=0) and the RMS amplitude of each FTAN was used for the dispersion curves manual picking.

The sources of ambient noise for the study area were complex, due to the nearby large railways and spots of agricultural activities. Perhaps, the main sources of ambient vibrations are the Egnatia highway and a secondary E-W road in the northern part of the array. Also, the agricultural activities in the area are significant, with a large amount of water pumping from boreholes taking place. The cross-correlated envelope traces show an asymmetry (especially in the N-S paths), due to the complex wave-field of ambient vibrations, making more difficult the accurate picking of the dispersion curves.

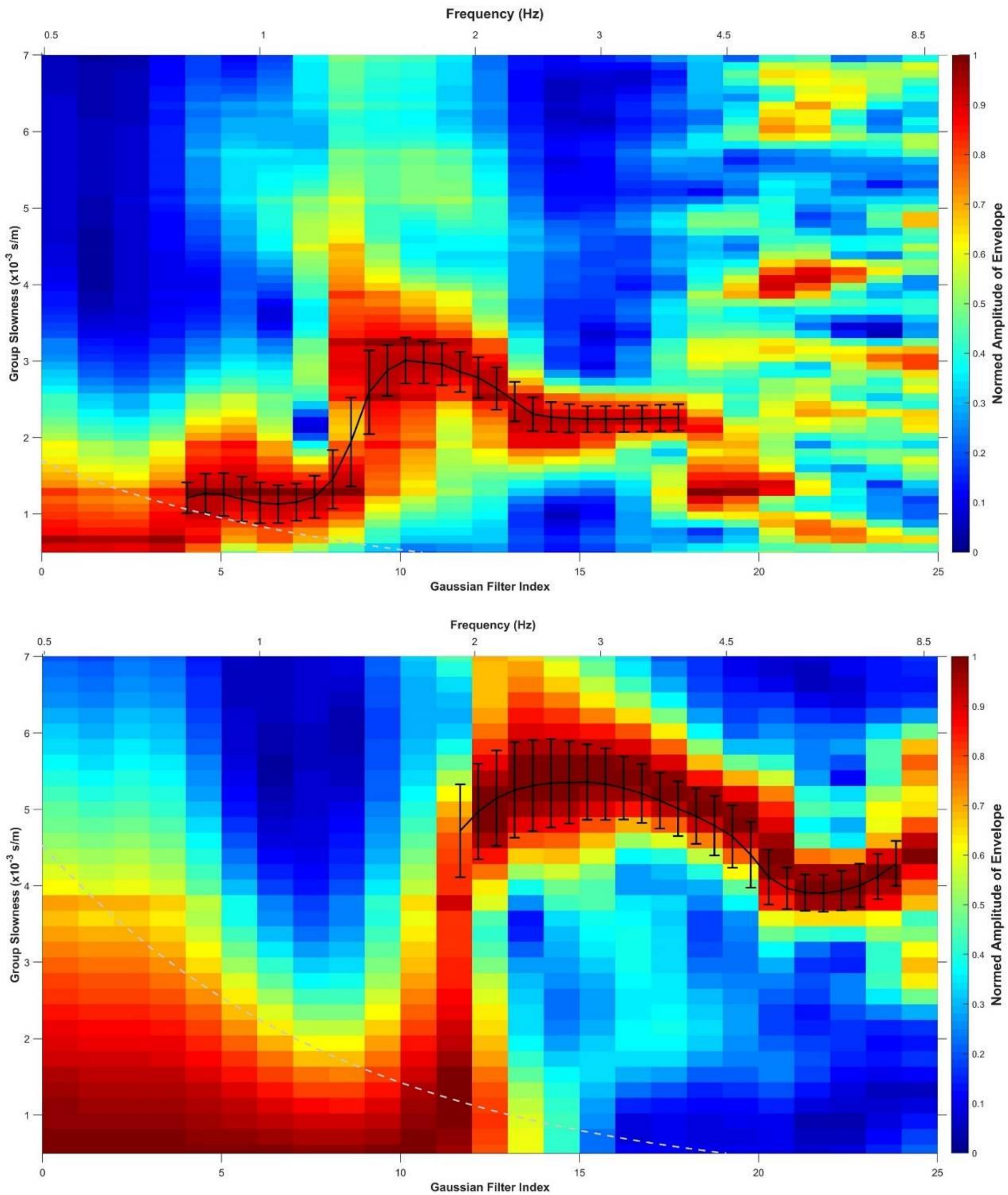


***Figure 24.*** Resulting FTAN for a northern (up) and a southern (down) inter-station path of the recording array. The area of maximum normalized amplitudes of the envelope function (red blocks) depicts the energy maxima of each path (the group slowness dispersion curve for Love waves). The dashed grey line depicts the r=2λ curve, bounding the FTAN area which corresponds to untrusted wavelengths. The northern path energy maxima correspond to smaller group slownesses (larger group velocities) for the same frequency than the southern path, being strongly affected by the local geology.

The heterogeneities of the basin and the complex geologic structure lead to the scattering of seismic energy and the resulting energy maxima areas are rather random for high frequencies (more than 10 Hz), as observed in many cases during the manual picking of the dispersion curves. Also, small frequency (large period) signals tend to dominate the power spectra of the wave-field carrying information from large distances (larger penetration depths), that could not be sampled by the instrument array. Therefore, to improve the efficiency of the dispersion curves, the energy maxima points corresponding to distances smaller than two times the maximum wavelength (grey dashed lines in Figure 24), were discarded.

In total near 1000 dispersion curves of the maximum 1426 possible were manually picked from the FTAN plots for Love waves. The derived Love wave group slowness dispersion curves are superior to any automatic processing/picking, as shown by previous research for the area (Hannemann et al. 2011, Gkogkas et al. 2018). Also, the derived dispersion curves exhibit significant spatial variabilities, having smaller average group slowness (higher group velocities) for northern paths, where bedrock outcrops and larger average group slowness (slower group velocities) for intermediate and southern paths, where the sedimentary deposits have significant thickness (Figure 24).

## 3.2 Love wave travel-times

### 3.2.1. Acquisition of travel-times

The derived dispersion curves for Love waves were resampled (0.02 log-frequency steps from 0.5 to 30 Hz) resulting in a total number of 56 frequencies. The standard deviation of each dispersion curve was manually picked to take into account the possible flattening of the energy maxima due to the stacking of negative and positive time lags. The travel-times of Love waves were computed for each frequency from the group slowness values of each dispersion curve and the corresponding path inter-station distance (0-1800 m). The inter-station distance, D, between station A($x_1$,$y_1$) and B($x_2$,$y_2$) is computed as:

$$D = \sqrt{(x_2 - x_1)^2 + (y_2 - y_1)^2} \tag{3.1}$$

The resulting Love wave travel-times tend to have a complex variation with the inter-station distance for small frequencies (e.g. 0.95 Hz in Figure 25) and limited variability for inter-station distances larger than 1200 m. The first observation can be explained by the complex wave propagation of small frequencies. The reason of the second observation can be the presence of higher mode propagation due to the anelastic attenuation of fundamental mode (presence of low Qs / low Vs Holocene deposits in the southern part). The second observation was recognized by Hannemann et al. (2014) for Rayleigh waves and therefore similar cut-off inter-station distance limit of 1200 m was implied to avoid the propagation of errors in the tomographic inversion procedure. These paths and travel-times are depicted by red colors in Figure 25 and mainly consist of N-S paths.

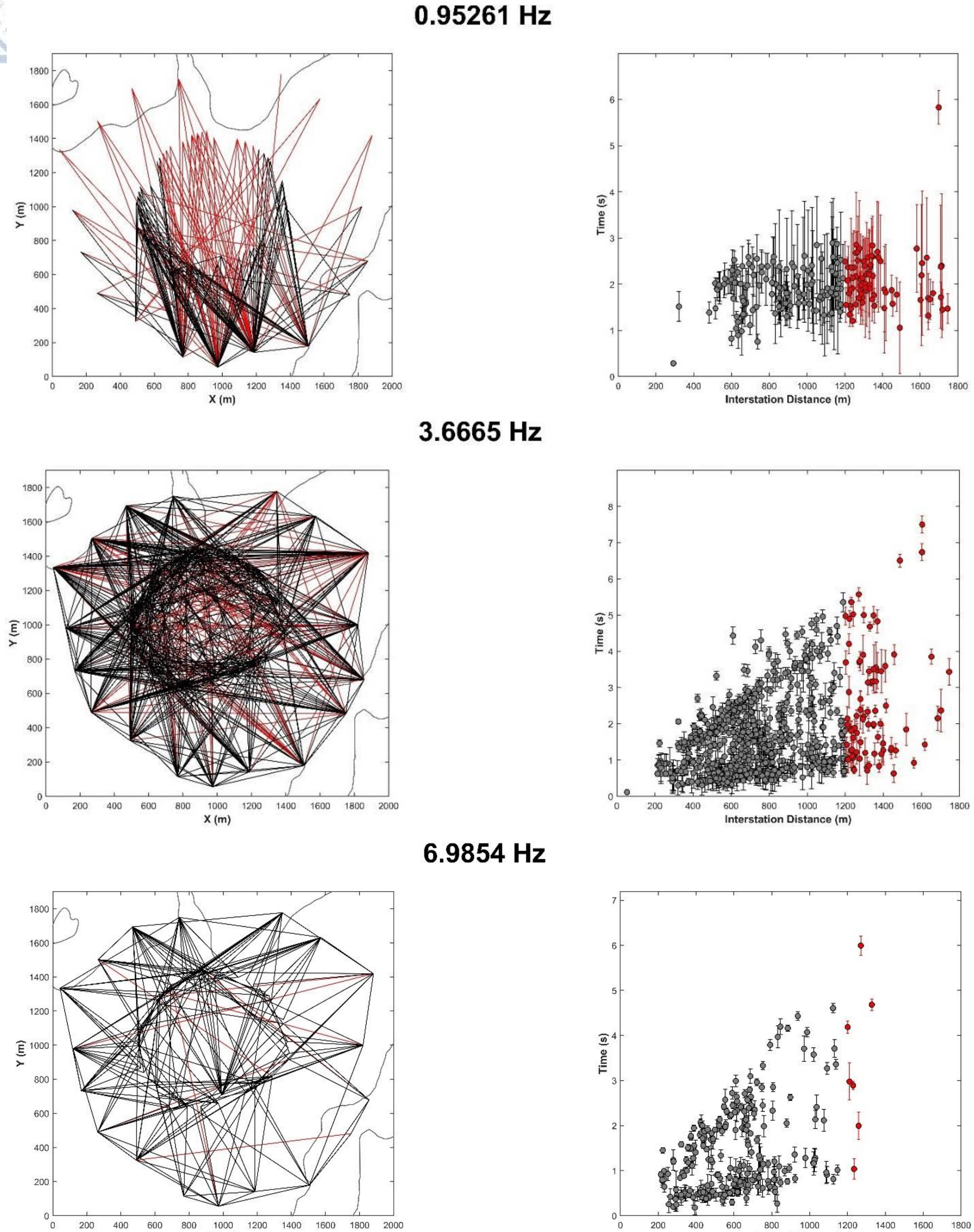


***Figure 25.*** Ray path coverage (left) and derived group travel-times of Love waves for three typical frequencies. Red paths and dots indicate discarded data, with inter-station distances larger than 1200 m.

### 3.2.2. Spatial variability of the travel-time dataset

The obtained travel-times for each frequency have several interesting characteristics regarding their spatial distribution. More, specifically for frequencies f > ~ 1 Hz, the derived travel-times have three different trend-lines, suggesting that they are strongly affected by the local geology. Therefore, the study area was subdivided into three separate regions, taking into account the N-S geology/tectonic pattern of the basin. The study area was divided in three sub-regions, according to each path Y midpoint (the average Y coordinate of each path in N-S direction). The study area was divided in a northern part with Ymid greater than 1200m, a southern part with Ymid lower than 600m and a central part with Ymid between 600-1200m.

Northern travel-times (Y > 1200 m) are absent in low frequencies (e.g. 0.95 Hz in Figure 26), depicting that the used inter-station distances could not sample the large wavelength propagating waves in the bedrock. Furthermore, there is not much information in the south for high frequencies (e.g. 7.86 Hz in Figure 26), depicting the presence of low Qs / low Vs Holocene/Quaternary formations and the anelastic attenuation of the fundamental mode of propagation (mainly at higher frequencies). Instead, the southern and northern paths are present in both small and high frequencies, respectively. There is a significant reduction of data for larger frequencies due to difficulties in the manual picking caused mainly by energy scattering due to the presence of small-scale heterogeneities in the basin.

The derived travel-time grouping is in well agreement with the N-S structure of the basin and the expected thickening of sedimentary deposits in the southern part of the study area. Moreover, three major trend-lines were observed for each frequency travel-times, exhibiting slow average group velocities in the southern part (red dots in Figure 26), being affected by Holocene/recent deposits and fast average group velocities in the northern part (blue dots in Figure 26), where paths are affected by the crystalline bedrock outcrop. The central paths exhibit intermediate average group velocities (green dots in Figure 26), being affected by the transition between bedrock and recent deposits (possibly related to the pre-Mygdonian system sediments). The central area includes paths that are mostly affected by both northern and southern velocities.

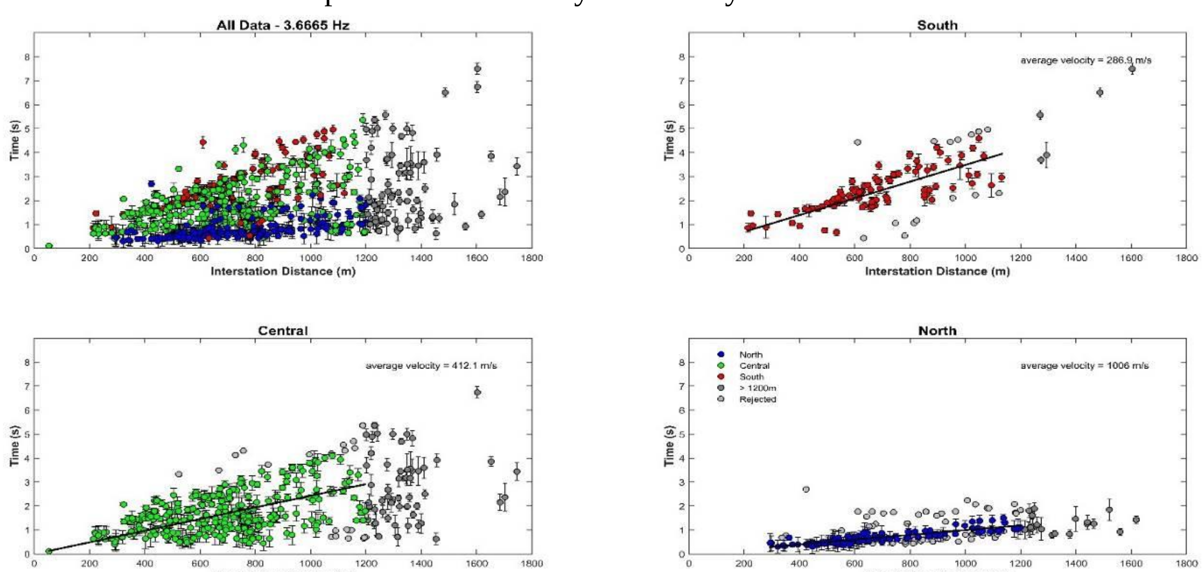

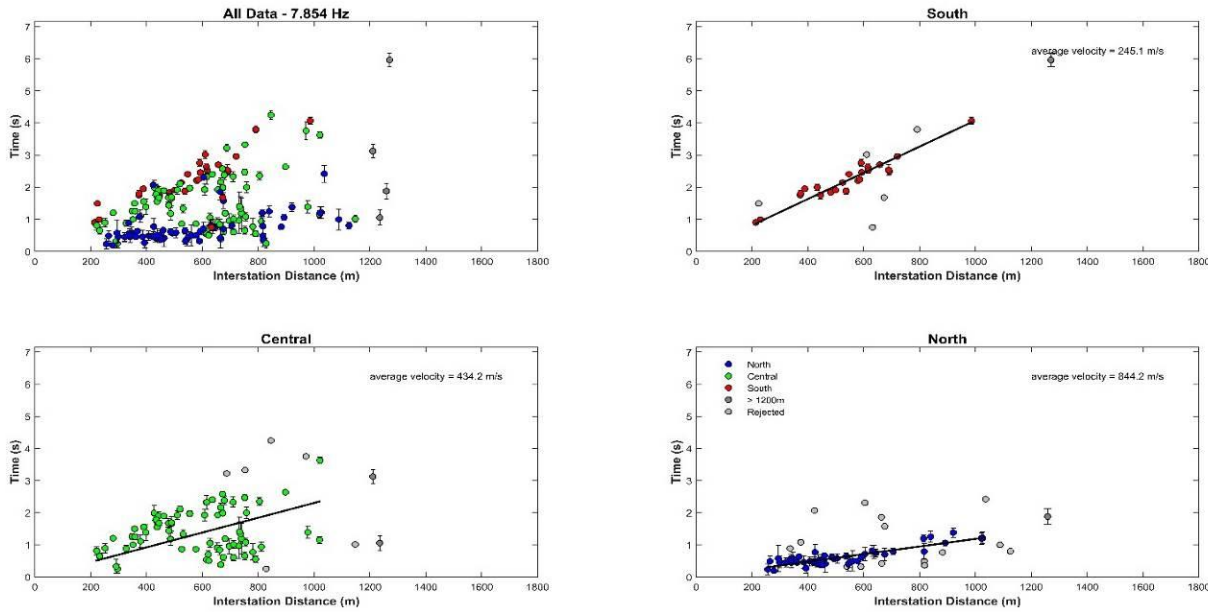


***Figure 26.*** Spatial variation of Love wave group travel-times for f = 3.67 Hz and f = 7.85 Hz. The obtained travel-times for each frequency were subdivided in three separate sub-regions (see the text for details). Light grey colors indicate inversion outliers and dark grey colors data with inter-station distances larger than 1200 m.

To quantitatively examine the reliability of the results, the standard deviation of each dispersion curve was also manually picked to study the propagation of uncertainties during the processing. The derived travel-times standard deviation histograms for each frequency revealed two populations with different mean values (Figures 27 and 28), almost normally distributed (blue and red bars in both figures). The populations were automatically separated and the azimuthal and spatial distributions of each population were examined, including the standard deviation magnitude. In particular, travel-times propagating in the eastern part of the array tend to have smaller standard deviations than those propagating in the western part. The correlation between the path azimuth with N-S orientation, which are perpendicular to the 2-D characteristics of the basin and the population with larger mean values can be possibly related to the post-stack flattening, due to positive and negative time lags stacking (waves travelling in opposite directions first encountering the bedrock and sediments, respectively).

To further explore this 2D pattern for the frequency band from 0.8 Hz to 14 Hz, each frequency travel-times were grouped into bins of 100 m in a N-S direction (based on Cartesian Y midpoint coordinate) and average group velocities were computed for each bin with 50% overlapping. The resulting smoothed group velocity curves in N-S orientation (Figure 29) converge for all frequencies at small Y values (southern part of the array), having small average group velocities (~200 m/sec), suggesting an excellent agreement with local geology, since they sample recent formations (Holocene/Quaternary sediments). In contrast, for large Y values (northern part of the array) the average group velocities converge to large values (more than 1000 m/sec), in excellent agreement with the outcropping crystalline bedrock (gneiss/schist). For intermediate Y values (central part of the array), the average group velocities have intermediate values (400-1000 m/sec).

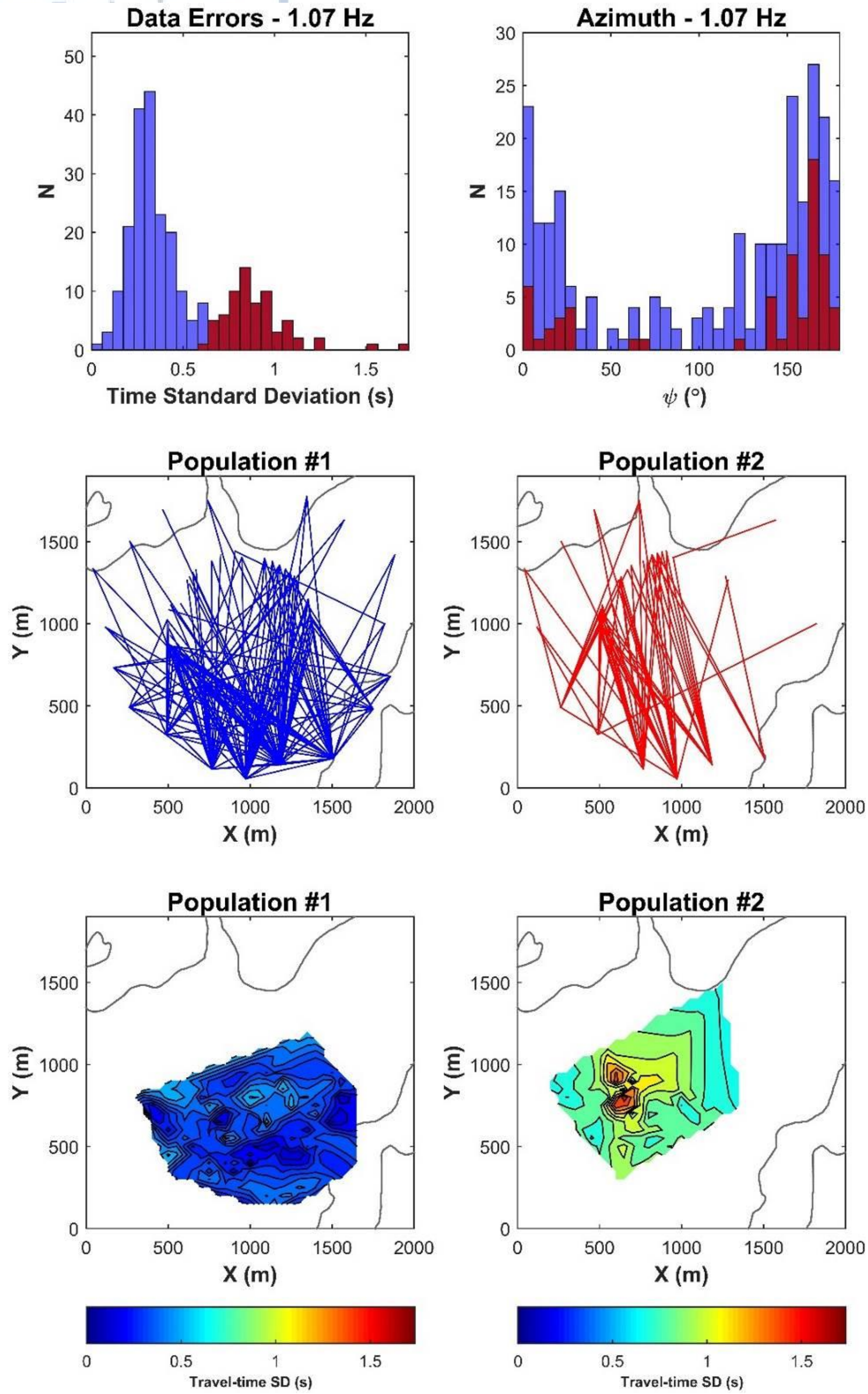


***Figure 27.*** Love wave group travel-times standard deviation histograms for 1.07 Hz, depicting the presence of two populations with different means (blue and red) and their azimuthal variation (up). Spatial variation maps of ray paths corresponding to each population (middle) and magnitude of standard deviation (down) are also presented.

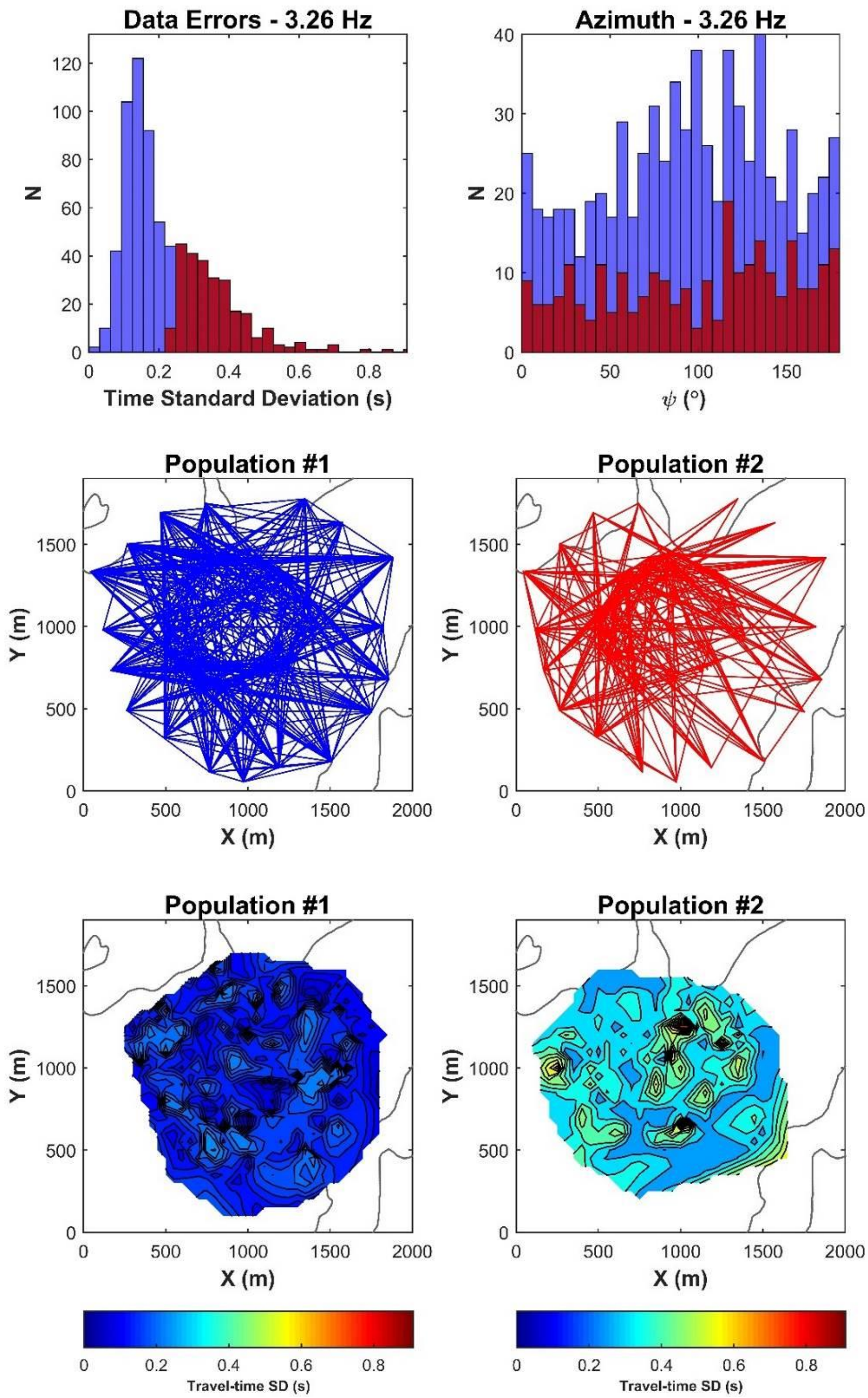


***Figure 28.*** Same with Figure 27 for 3.26 Hz.

A pseudo-2D model was created (similar to Hannemann et al., 2014) by 3rd order polynomial fit of the average group slowness values with respect to the binned Y coordinate and frequency. The derived smoothed pseudo-2D model (Figure 30) shows that in the southern part of the array (small Y midpoint values), the obtained group slowness values are large (small average group velocities), indicating that these paths penetrate recent formations, with low Vs and low Qs values, since information for higher frequencies is absent due to anelastic attenuation. On the contrary, for large Y distances (northern part of the model), paths for high frequencies tend to converge faster to the rather small average group slowness values (larger average group velocities), due to the different wavelengths of each seismic wave band being affected by the bedrock presence.

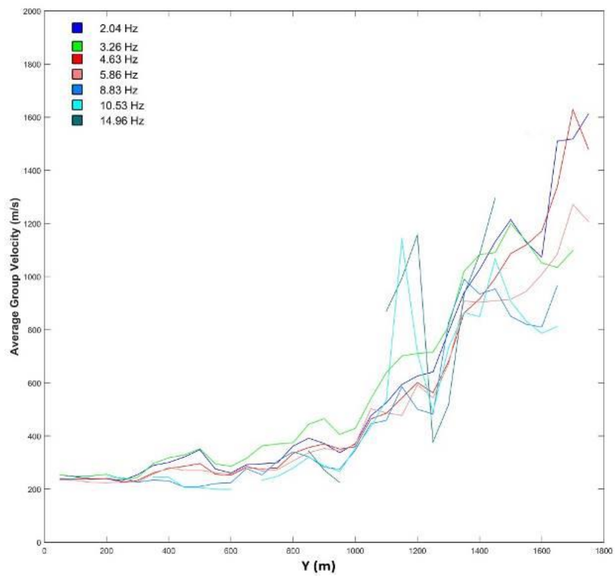


***Figure 29.*** Variation of smoothed average group velocities with respect to the local Y (North-South) coordinate distance for several frequencies of the acquired travel-time dataset, gradually increasing from small average velocities (sediments) in the south towards the larger Y distances (bedrock) in the North.

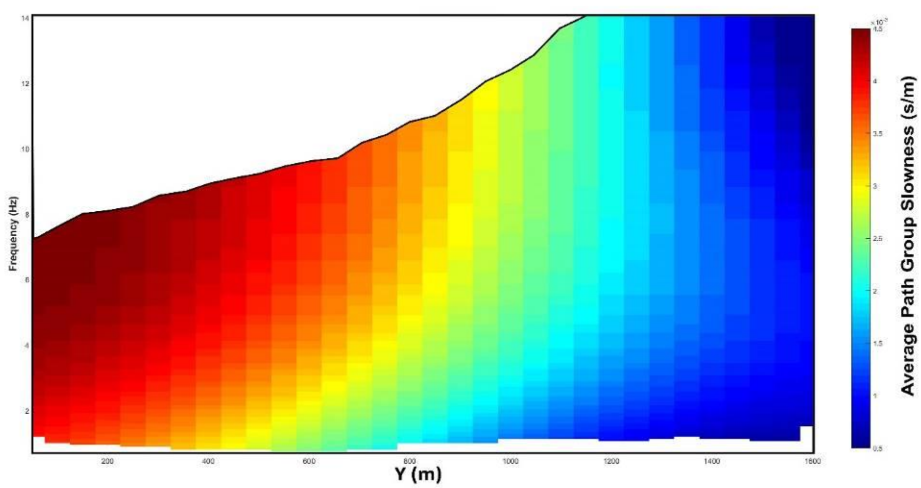


***Figure 30.*** Smoothed variation of average group slowness values for each binned Y coordinate and frequency (see text for details), derived from 3rd order polynomial fitting. Areas with no data are excluded from plotting.

## 3.3 Travel-time tomography

A tomographic approach was implemented in order to obtain the spatial variation of Love wave group velocities for each frequency. If L is the Fermat ray-length of each travel-time, $t_i$ (i=1,…,N) and the medium has group slowness, s, the following integral can be used to compute the expected travel-times:

$$t_i = \int_{L_i} s\,dl \qquad i=1,\ldots,N \tag{3.2}$$

This integral is the solution of the forward problem for travel-time tomography and can be transformed into a linear system if we divide the study area into a model of M nodes with group slowness $s_j$ (j=1,…M) and compute the associated length of each ray for each node, after performing a ray-tracing procedure. The linear system to be solved has the form:

$$\mathbf{t} = \mathbf{L}\mathbf{s} \tag{3.3}$$

To stabilize the solution and obtain spatially smoothed results, the linear system that was adopted has the following form:

$$\begin{bmatrix} \mathbf{L} \\ \lambda\nabla^2 \\ d\,\mathrm{I} \end{bmatrix} \mathbf{s} = \begin{bmatrix} \mathbf{t} \\ 0 \\ 0 \end{bmatrix} \tag{3.4}$$

where L is the derivative matrix of the Fermat ray-lengths for each node with respect to group slowness, s, λ is a spatial smoothing constant which stabilize the model roughness and d is a damping constant. These additional damping and smoothing constrains stabilize the final tomographic solution (see e.g. Aki and Lee 1976, Marquardt 1963, Constable et al. 1987) and generate a reliable tomographic model for each frequency, minimizing the propagation of uncertainties during the inversion procedure. Approximate first order Fresnel volumes were computed (ellipses in the 2D tomographic case), redistributing the elements of the derivatives matrix to take into account the volume that affects the travel-times of each path (as discussed in Cerveny and Soares 1992). Furthermore, an iterative approach was implemented transforming the system into non-linear solving for starting model corrections for each node. Also, data with large errors were rejected from the iterational process (3 total iterations). Each element of equation 3.4 is discussed in this section separately and the obtained results are discussed in the following.

### 3.3.1. A-priori model information

The first step in travel-time tomography is the acquisition of a reliable a-priori information model, in order to have a good first estimate of model parameters and perform ray-tracing. Then we invert for model corrections for each node with respect to the starting group slowness for each frequency. If $m_s$ is the starting group slowness for each frequency, the final inversion solution for each node is $s_j$ (j=1,…,M) and $\delta m^{LSQ}$ is the inversion solution for each iteration, then:

$$s_j = m_s + \delta m_j^{LSQ} \tag{3.5}$$

This step of the inversion could be performed either by computing an average group velocity for each frequency from the best-fit line of travel-times with respect to inter-station distance (e.g. Behm et al. 2013) or by using an average group slowness from all data for a given frequency (e.g. Hannemann et al., 2014). The average group slowness model derived from the arithmetic mean of the group slowness values of all paths for each frequency is shown in Figure 31, and it was used as *a-priori* model information (Figure 31). It is also notable that the computed values for large frequencies (> 10 Hz) exhibit anomalous variations, due to the lack of precise data for these frequencies, as well as the dominant presence of bedrock-crossing paths for these frequencies.

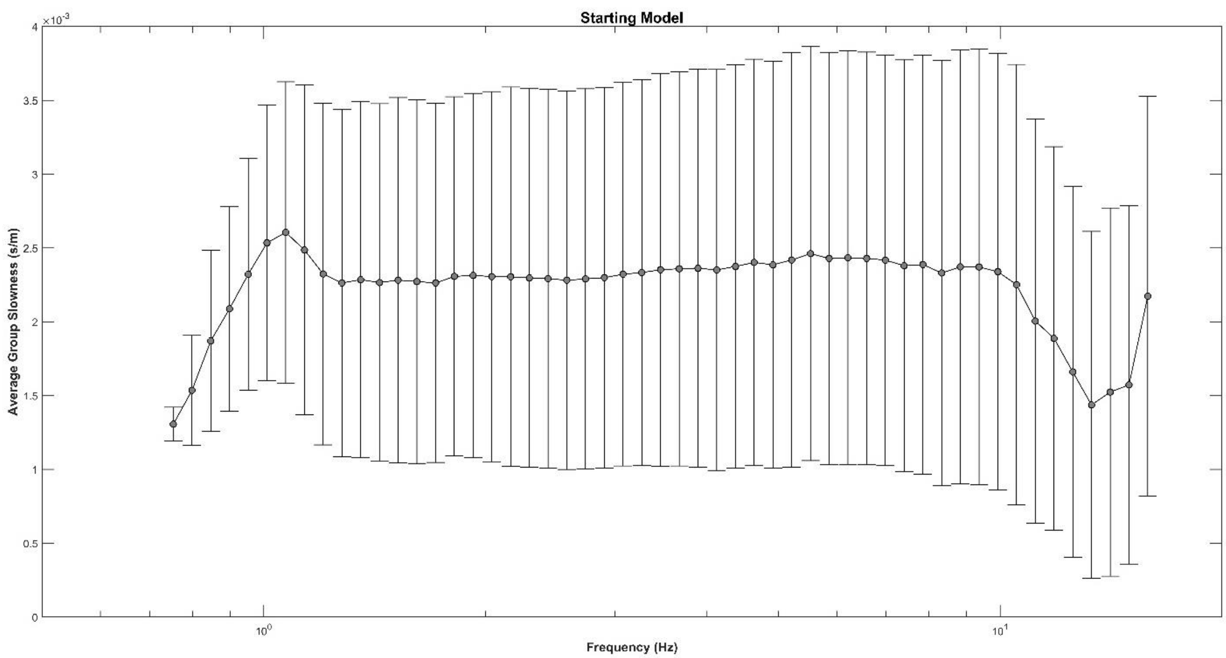


***Figure 31.*** Average group slowness for each frequency derived from the arithmetic mean value from the observed travel-time dataset.

## 3.3.2. Damping and smoothing constrains

As earlier explained, in order to retrieve reliable tomographic results for the Love wave group velocities spatial variation for each frequency, appropriate damping and smoothing constrains were used during the solution of the inverse problem. As discussed in Chapter 2, damping is used to constrain large variations of the solution, while spatial smoothing is used to obtain smooth tomographic results and avoid artificially rough models. The optimal solution would minimize the trade-off between misfit and model roughness, since implementation of large damping values tends to increase the data error and large spatial smoothing values tend to generate over-smoothed models. To choose an optimizing combination of damping, d, and spatial smoothing, λ, constrains, a large set of combinations between these two constrains were used. Specifically, damping values from 0 to 200 with steps of 10 units were tested, with parallel testing of spatial smoothing values from 0 to 1000 with steps of 100 units. The model and data variances were computed to test the trade-off between these parameters for each combination of damping and spatial smoothing constrains following the approach of Zhang et al. (2009). The unbiased model variance can be calculated by (Tong et al., 2014):

$$\sigma_m{}^2 = \frac{1}{M-1}\sum_{i=n}^{M}(X_i - \bar{X})^2 \tag{3.6}$$

where M is the number of model nodes and X is the mean solution. The data variance can be approximated by (Tong et al., 2014):

$$\sigma_d{}^2 = \frac{1}{M-1}\sum_{i=n}^{N}(T_i^{obs} - T_i^{syn} - \sum_{j=1}^{N} a_{ij}X_j - \bar{d})^2 \tag{3.7}$$

where d is computed as:

$$\bar{d} = \frac{1}{N}\sum_{i=n}^{N}(T_i^{obs} - T_i^{syn} - \sum_{j=1}^{M} a_{ij}X_j) \tag{3.8}$$

and quantities $T_i^{obs}$ and $T_i^{syn}$ (i=1,…,N), respectively are observed and synthetic travel-times and $a_{ij}$ are the elements of the derivative matrix.

From the total set damping and smoothing constraints that were tested, data and model variances for values from [0 200] and [500 1000] for each constrain, respectively, are shown in Figure 32 for the frequencies of 2.29 Hz and 3.67 Hz. From the visual inspection of the plots the selected optimal damping constrain is 100, since it minimizes the trade-off between model and data variance for both frequencies and for all iterations. Similarly, a spatial smoothing of 500 was chosen, since the derived tomographic models are smooth, while the corresponding data errors are minimized.

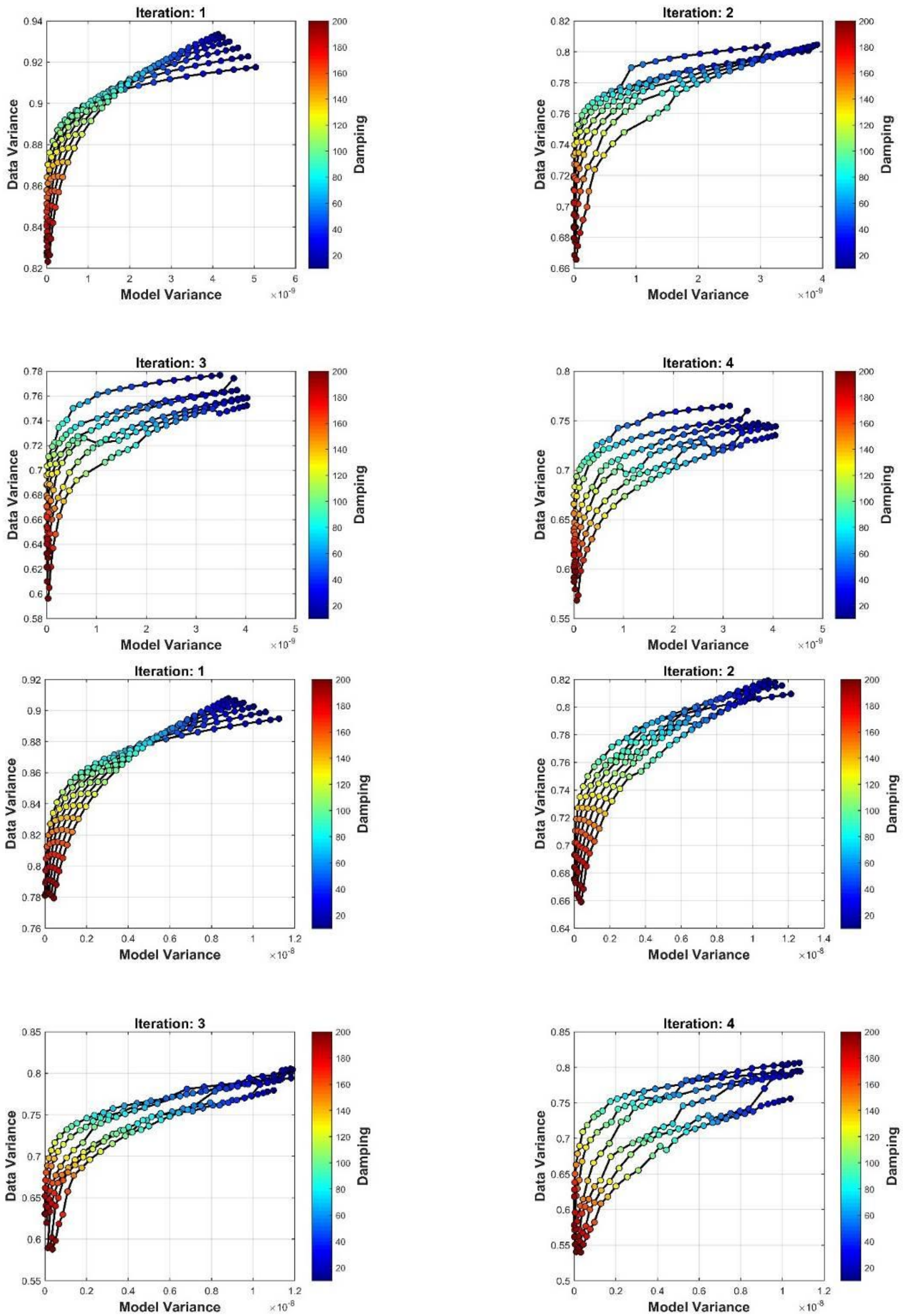


***Figure 32.*** Trade-off curves between data and model variance for each iteration of the solution for damping values from 0 to 200 (different color indexing) and for spatial smoothing values from 500 (lowermost curve) to 1000 (uppermost curve) for frequencies 2.29 Hz (up) and 3.67 Hz (down).

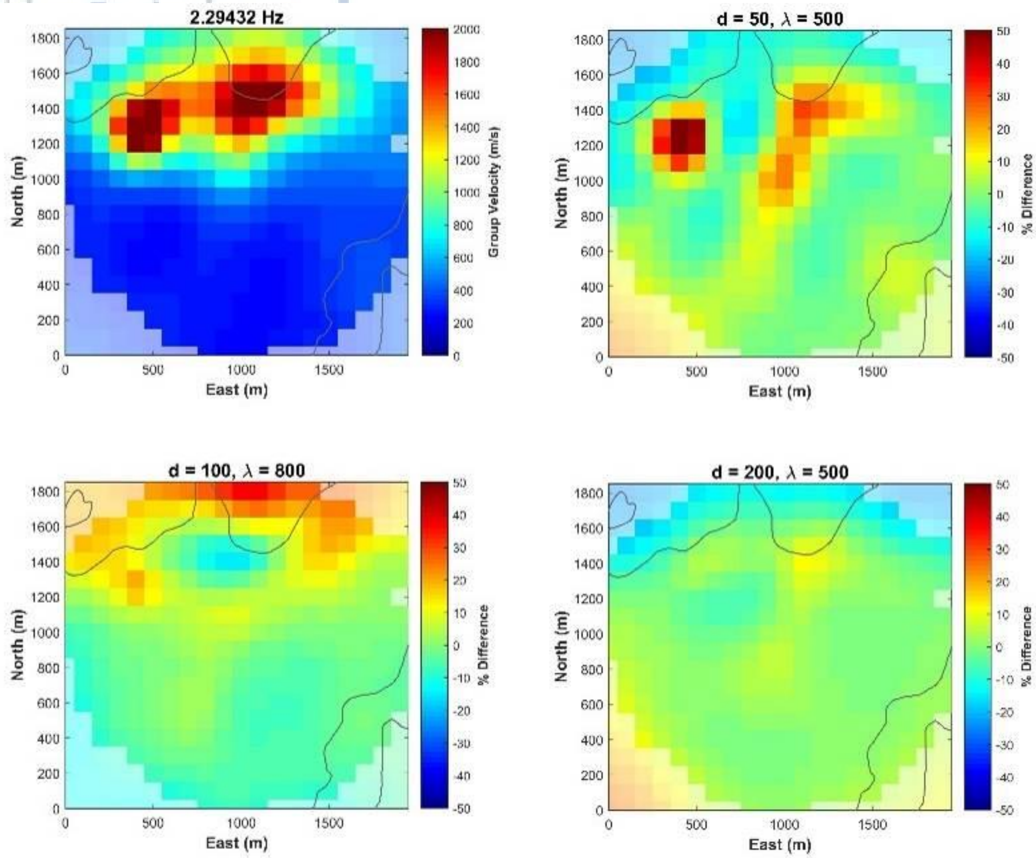


***Figure 33.*** Spatial variation of derived group velocity models for the frequency of 2.29 Hz and percentage differences for under-damped (d=50), over-smoothed (λ=800) and over-damped (d=200) solutions.

To quantitatively examine the impact of damping and spatial smoothing constrains, the percentage differences between the derived group velocity model and the cases of over-smoothed (λ=800), over-damped (d=200) and under-damped (d=50) models are examined for the frequencies of 2.29 Hz and 3.67 Hz, in Figures 33 and 34, respectively. The nodes not satisfying resolution quality cut-off criteria (see section 3.4.2.2) are presented with lighter colors. It is notable that over-smoothed models tend to have larger group velocities in the northern part of the array, while over-damped models have larger group velocities in the southern part of the array and lower in the northern, exhibiting even larger instabilities in the case of under-damped solutions. Especially for nodes not satisfying resolution quality cut-off criteria, these differences vary up to 40% both negative and positive in the northern and the southern part of the array, respectively, indicating the strong control of the solution from the damping and spatial smoothing constrains, since information for these nodes is limited or absent.

The data-set used for the derivation of the trade-off curves was also used to examine the spatial variation of the derived group velocities range for different damping and smoothing constrains. This spatial variation is presented in Figure 35 for the frequency of 2.29 Hz, where only nodes satisfying quality cut-off criteria (later discussed in detail) are shown. The obtained range of velocities for the southern part of the model is smaller compared to the range of Love wave group velocities in the northern part. Furthermore, variations in group velocities for the southern nodes are smaller than 200 m/sec, with nodes even having a variability less than 10 m/sec, while the range of velocities for the northern nodes is of the order of 300 m/sec and varies up to 700 m/sec in some cases.

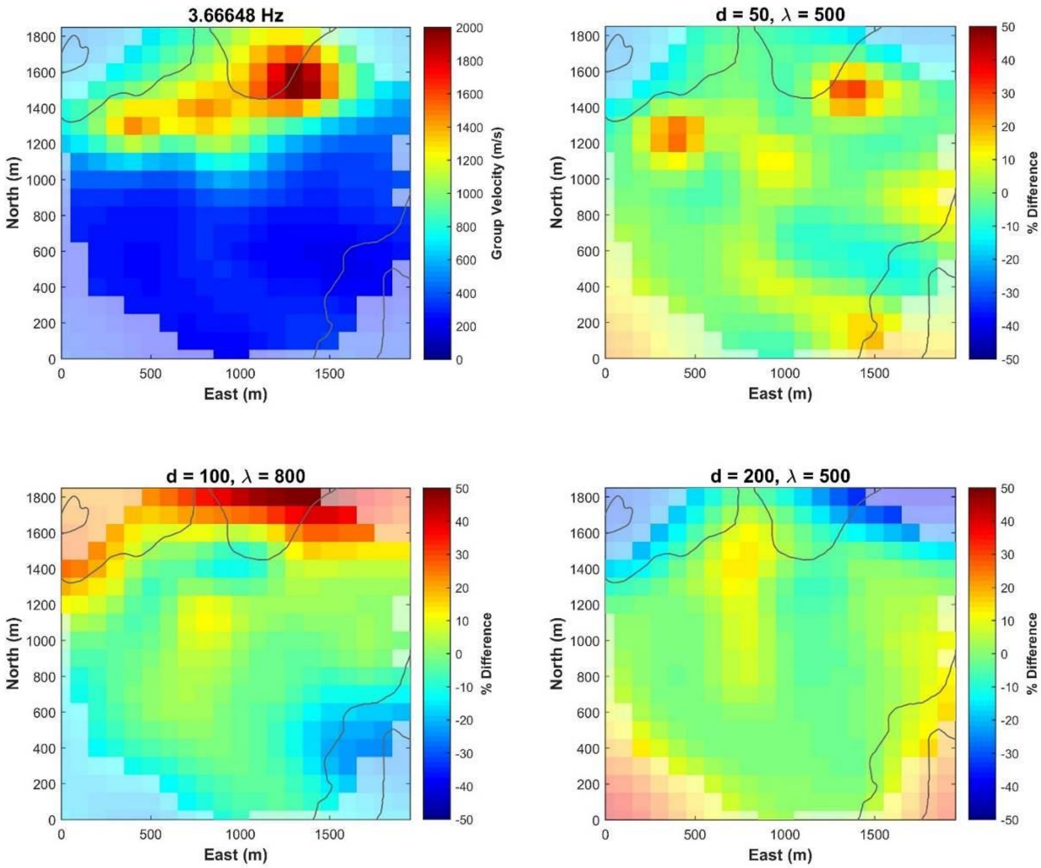


***Figure 34.*** Same with Figure 33 for the frequency of 3.67 Hz.

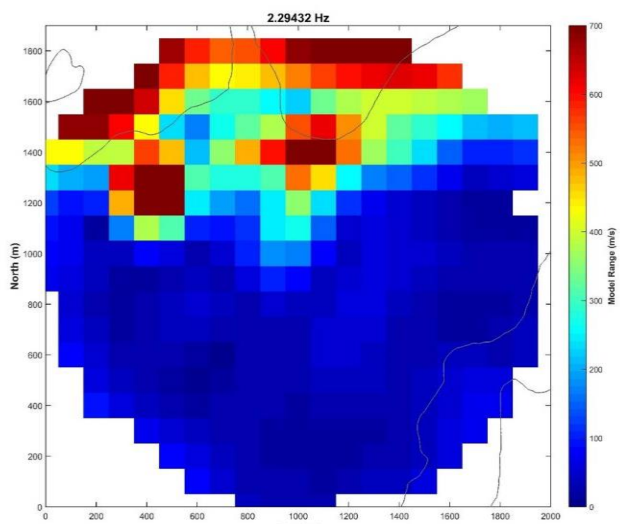


***Figure 35.*** Group velocity range of the derived models for different combinations of damping and spatial smoothing constrains for the frequency of 2.29 Hz.

### 3.3.3. Tomographic results

The derived Love wave group velocity maps for six typical frequencies are presented in Figure 36. The study area was divided in 420 nodes and more than 50 frequencies were inverted (more than 20.000 total group slowness unknowns). As expected, the resulting group velocities for northern nodes are larger than the southern. The results are in excellent agreement with local geology, indicating the presence of the outcropping crystalline bedrock in the north and the sedimentary formations thickening as we move towards the south. Moreover, the contact between the bedrock and the sediments roughly corresponds to the group velocity of ~ 700 m/sec contour. In the western part, this boundary has NW-SE orientation, while in the eastern part (after 1000 m in Cartesian X distance) its trend changes to NE-SW, in excellent agreement with the geometry of the outcropping bedrock.

Due to the uncertainties of the inversion and the solution instability, it is interesting to test the resolution of the boundary between bedrock (high group velocities) and sediments (small group velocities). The tomographic results from over-smoothed, over-damped and under-damped parameterization indicate that the derived group velocities can vary up to 20 % in absolute value in well resolved nodes and up to 40 % in nodes not satisfying resolution quality cut-off criteria. Furthermore, due to the lack of significant lateral variations in the tomographic results for several frequencies, the average solution in a N-S section (parallel to the Cartesian Y coordinate) was computed to test the stability of this boundary. Therefore, the tomographic results were averaged along a N-S section and the average group velocity solution was computed for each increment in Y (North-South) coordinates for all frequencies (Figure 37).

It is notable that the derived group velocities in the southernmost (mainly affected by the sedimentary deposits) and northernmost (mainly affected by the bedrock) part of the tomographic grid vary between the examined solutions. The average solution N-S variation for each frequency indicate that the boundary between low and high group velocities is recognized in all cases (over-damped, under-damped, over-smoothed) and well resolved, since the rate of increase in average group velocities with respect to the Y distance is similar. Therefore, the main features of the 2-D geometry are well resolved by the tomographic results.

An interesting feature of Figure 37 is the absolute variation between the derived average group velocities in the southern and the northern part of the array. The solutions for the southern part of the array tend to have smaller group velocities for over-smoothed and over-damped solutions and larger group velocities for under-damped solutions. In contrast, the solutions for the northern part of the array tend to have larger group velocities for over-smoothed and over-damped solutions and smaller for under-damped solutions. The probability density function and the histogram for the derived solutions for a large set of damping and spatial smoothing constrains are presented in Figure 38, small velocity ranges (~30 m/sec) for southern nodes and a large range (> 300 m/sec) for northern nodes.

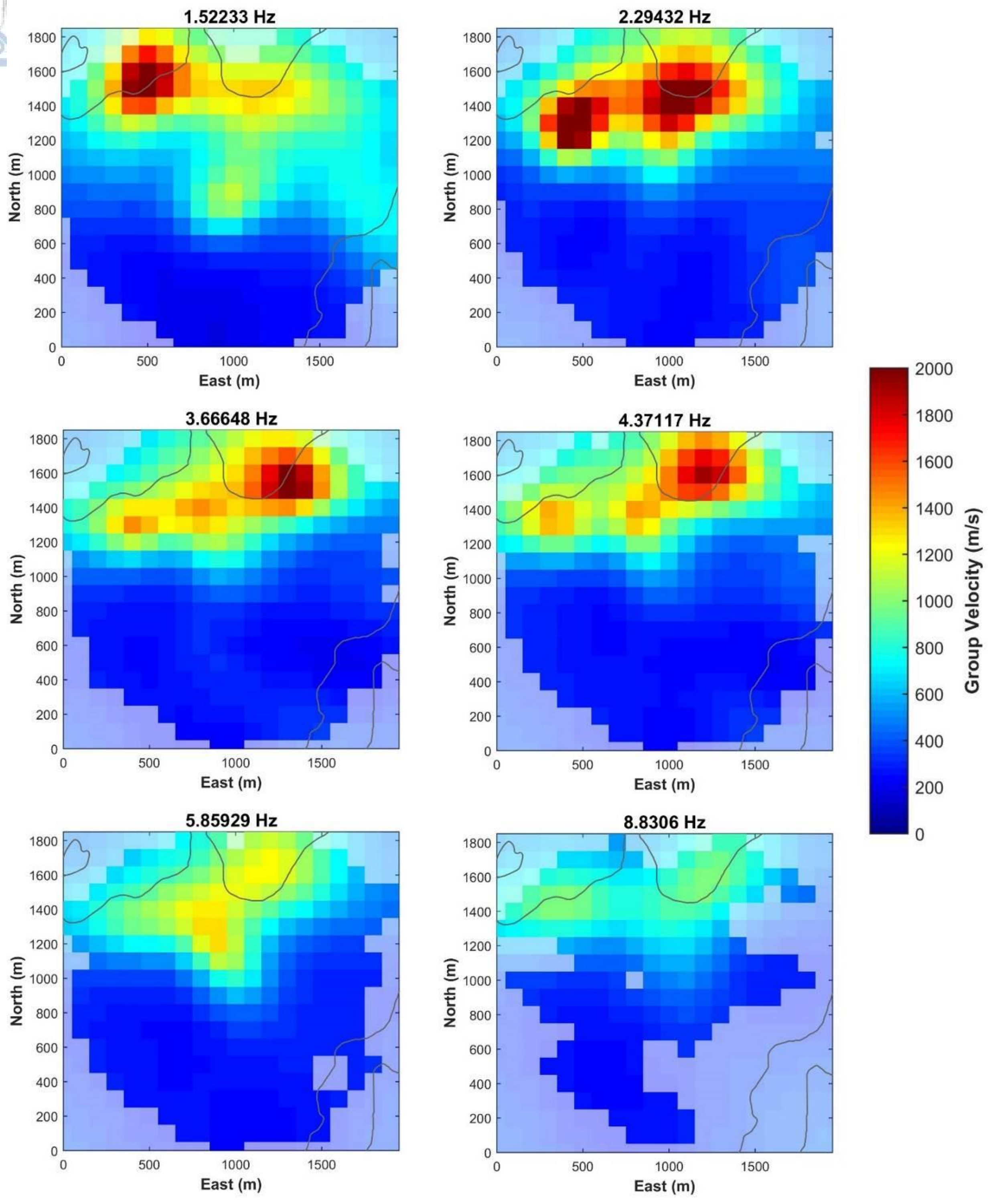


***Figure 36.*** Derived tomographic results of Love wave group velocities for six typical frequencies (1.52, 2.29, 3.66, 4.37, 5.86 and 8.83 Hz). Nodes not satisfying quality cut-off criteria are shown with lighter colors. Each frequency was inverted independently. while the obtained maps are in good agreement with the local geology.

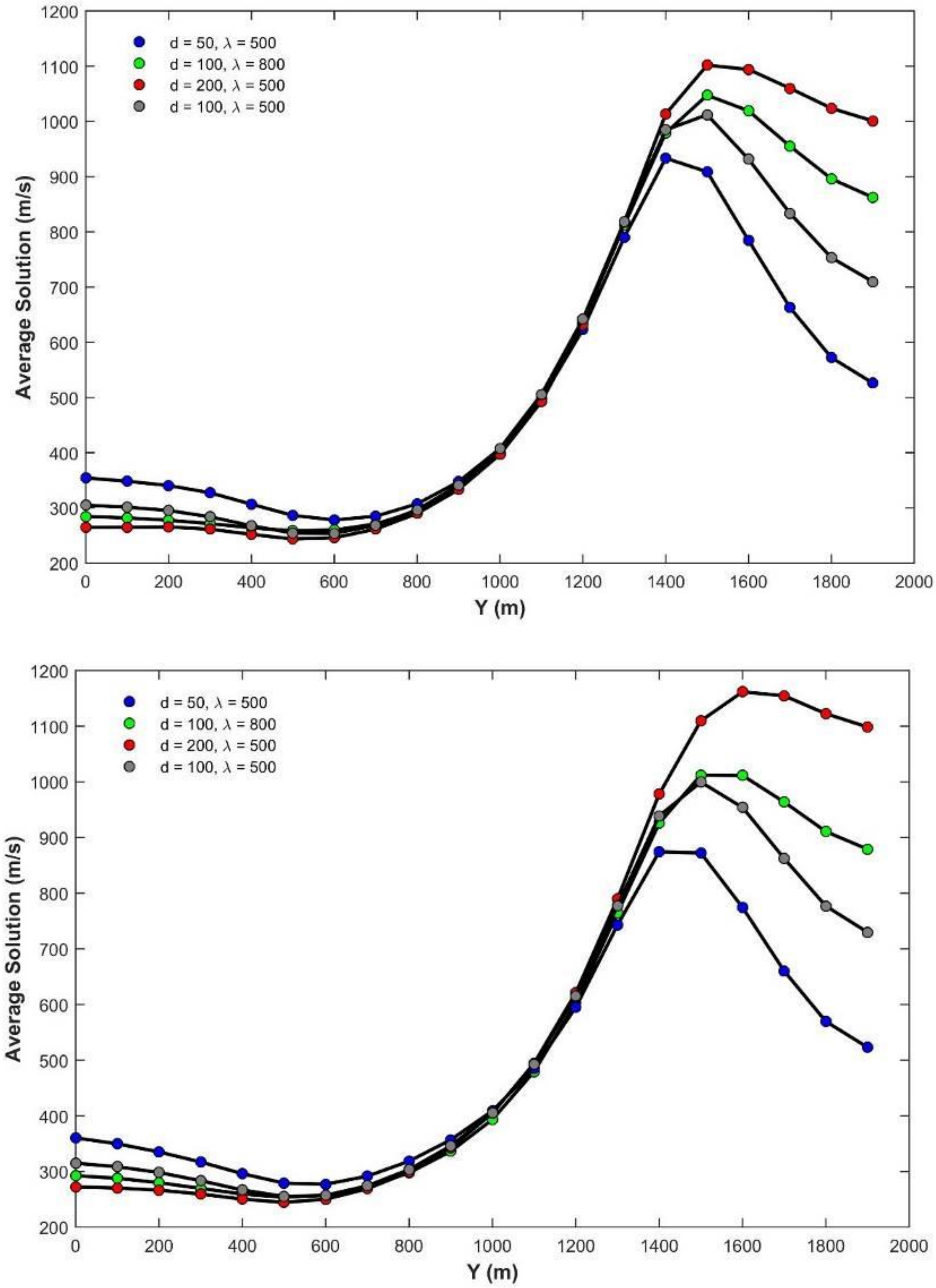


***Figure 37.*** Average group velocity derived from averaging the model along a North-South profiles (Y coordinate) for a set of combinations of damping, d, and spatial smoothing, λ, constrains for the frequencies of 3.67 Hz (up) and 4.37 Hz (down). Grey dots indicate solution minimizing the trade-off between data and model variance, red dots solutions with higher damping, green dots over-smoothed solutions and blue dots under-damped solutions.

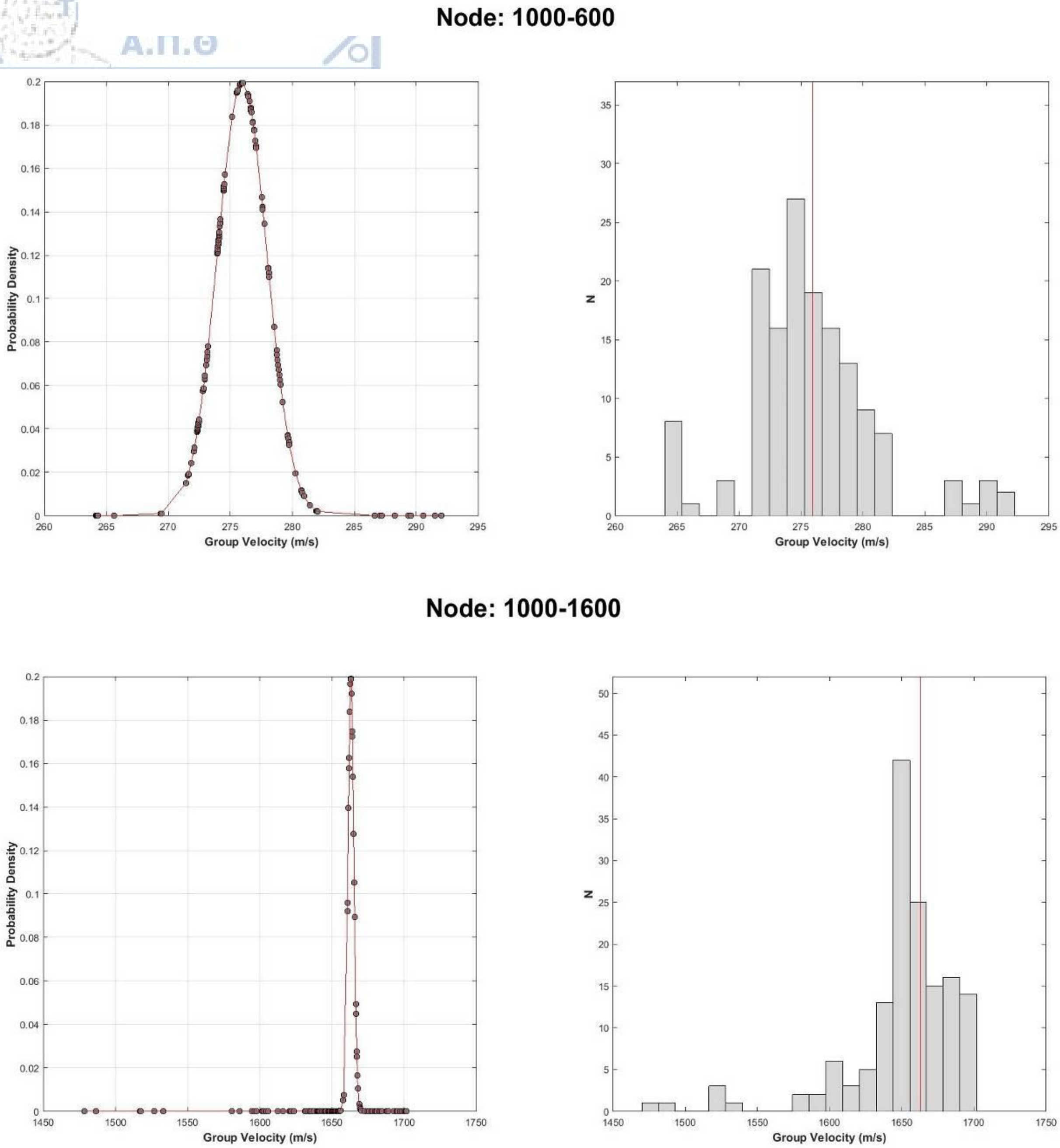


***Figure 38.*** Probability density function and histograms of derived group velocities for two nodes satisfying quality cut-off criteria for the frequency of 2.29 Hz, for different damping and spatial smoothing constrains. The red line depicts the solution minimizing the trade-off between data and model variance adopted in this work.

## 3.4. Data and model errors

### 3.4.1. Data errors

#### 3.4.1.1 Observed and synthetic travel-times

The distribution of the observed versus calculated (synthetic) travel-times was computed for three models. The first model (referred as 1D model) indicates the synthetic travel-times computed from the difference between the observed travel-times and the a-priori group slowness model for each frequency. The second model (referred as 2D model) was computed from the following integral:

$$t_{2D} = \int_0^1 s(y)\left|\frac{ds}{dt}\right| dt = d\int_0^1 s(y)dt \tag{3.9}$$

where d is the Cartesian distance (equation 3.1) between points along path and s(y) is the 3rd order polynomial fit of Figure 30 for constant frequency, f, value:

$$s(y) = a_{33}y^3 + (a_{20} + a_{21}f)y^2 + (a_{10} + a_{11}f + a_{13}f^2)y + (a_{00} + a_{01}f + a_{02}f^2 + a_{03}f^3) \tag{3.10}$$

The third model (referred as 3D model) comprises from the synthetic travel-times computed after the final iteration of the inversion process and from outlier data. The observed travel-times versus calculated travel-times for two typical frequencies (2.29 and 3.67 Hz) are shown in Figure 39 for the 3 models. The distribution of the 1D model calculated travel-times with respect to the observed poor, showing large deviations from the bisector. The 2D model travel-times are significantly better than the 1D model, with smaller deviations from the bisector. Finally, the 3D model travel-times calculated from the inversion process have a good fit with the observed travel-times. In the same figure data with large deviations (more than 2 standard deviations away from the predicted travel-time) are plotted in light grey color and were excluded from the inversion process. A metric of the fit between the observed and synthetic travel-times is the Root Mean Square (RMS) error, calculated from the equation:

$$RMS = \sqrt{\frac{\sum_{i=1}^{N}(T_i^{obs} - T_i^{syn})^2}{N}} \tag{3.11}$$

where $T_i^{obs}$ and $T_i^{syn}$ are the observed and synthetic travel-times and N is the number of data. The computed RMS values indicate that the 3D model parameterization best fits the data, with smaller differences between observed and synthetic travel-times, while the 1D model has the largest RMS values and the 2D model has intermediate RMS values.

The histograms of the residuals between observed and synthetic travel-times are shown in Figure 40 for the frequency of 2.29 Hz. The 3D model travel-time residuals are almost normally distributed, with small tails (indicating outlier data). The 2D model residuals distribution is close to normal. The 1D model distribution is rather sparse and shows two populations, corresponding to fast and slow travel-times, due to the removal of the mean group slowness. In all figures, the normal distribution fits and a kernel smoothed fit are depicted with red and blue colors.

Moreover, the normal probability plots for each model are shown in Figure 41 for frequencies 2.29 and 3.67 Hz. The 1D model residuals tend to aggregate in the red solid line due to the large and small residuals superposition (and corresponding travel-times). The 2D model residuals have significant tails for small and large travel-times (curved fit), while the 3D model residuals fit well to the red solid line, indicating a good fit to the normal distribution for the residuals derived from the tomographic inversion of the travel-time set for both frequencies.

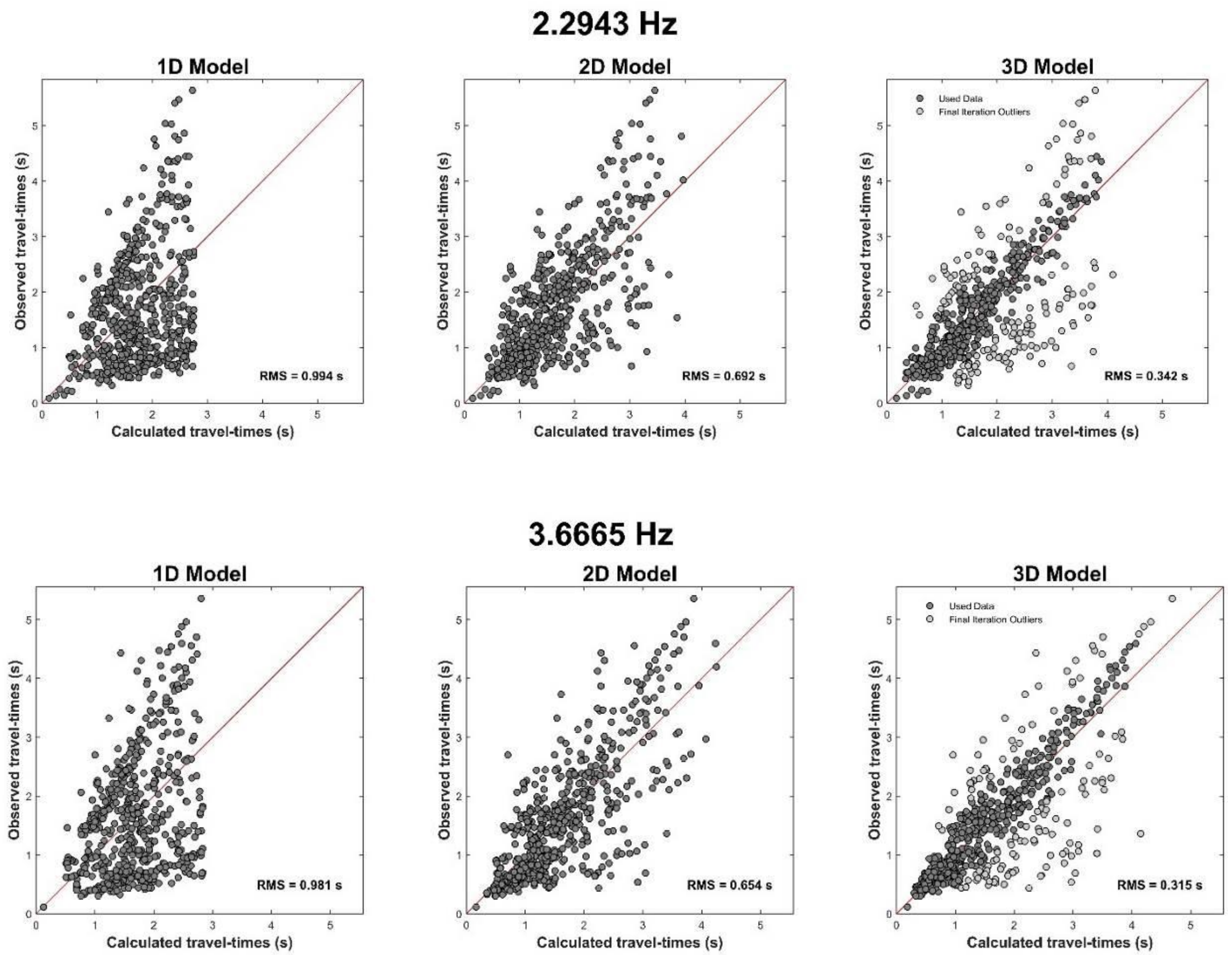


***Figure 39.*** Observed travel-time versus calculated travel-time plots for the 1D, 2D and 3D models (see text for details) for the frequencies of 2.29 and 3.67 Hz. The bisector is depicted with red solid line and light grey colors indicate inversion outlier data.

The lengths of the minor and major axes of the ellipses were computed for 1 standard deviation (RMS error). The derived plots for the first iteration indicate the presence of slow and fast travel-times, since it is derived in the same way for the 1D model, by removing the mean group slowness from the data. The inversion process focused on the minimization of the residuals between the observed and synthetic travel-times minus the 1D model travel-time. The next iteration steps focus on constraining the deviations of these two populations by minimizing the residuals between synthetic and observed travel-time differences and aggregate during last iteration. Most of the Jack-knife solutions are bounded by the ellipse, indicating a good fit between observed and synthetic travel-times for each iteration. The amount of rejected data during the iterative least-square solution of the inverse problem varied between different frequencies with a mean amount of 10-15 % original data rejection.

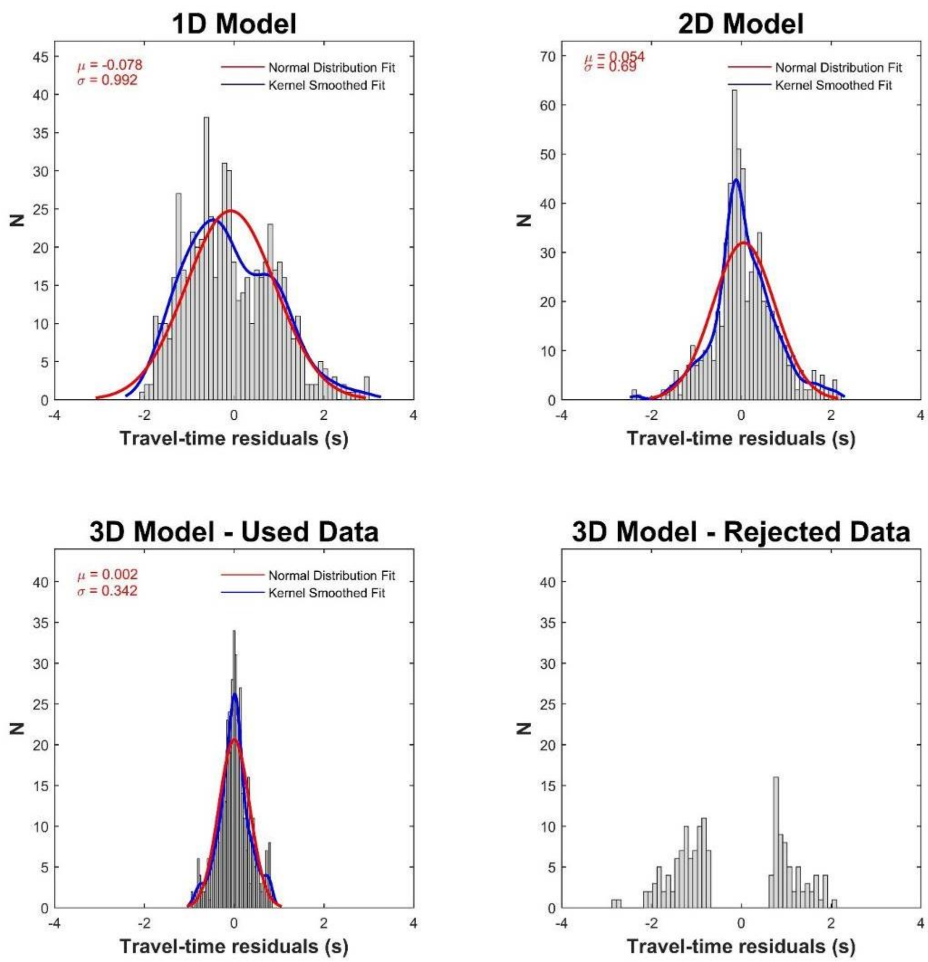


***Figure 40.*** Histograms of travel-times residuals for the three models (1D, 2D, 3D) and the 3D model outlier data for f = 2.29 Hz (see text for details). The normal distribution fit is shown with red color and a kernel smoothed fit with blue color. The mean and standard deviation of the fitted Gaussian distribution are also given with red color.

There are several frequencies for which the synthetic data either overestimate (high frequencies) or underestimate (lower frequencies) the observed travel-times. The best-fit linear regression lines are shown in Figure 48 for the whole frequency band considered (left) and after its limitation (right, also see Figure 52). This observation can be explained either by the small amount of data or by the implemented model uncertainties. As discussed in section 3.4.2.2, the number of data is rather small for high frequencies (larger than 12 Hz) and probably affected by higher modes of propagation, while the amount of data for small frequencies (lower than 1.2 Hz) is efficient.

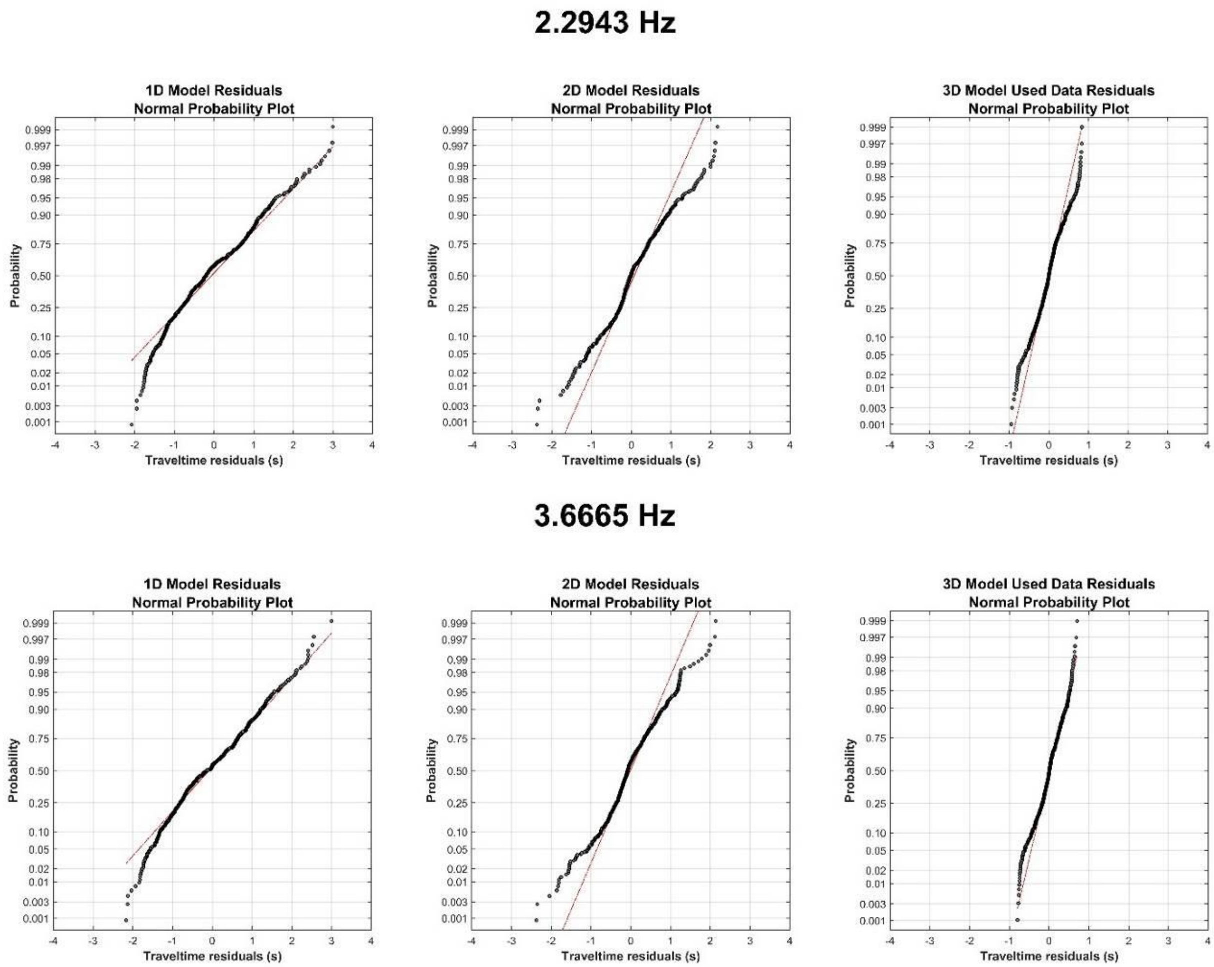


***Figure 41.*** Normal probability plots of the residuals between observed and synthetic travel-times for each model (1D, 2D. 3D). The red solid line depicts the reference line for the normal distribution.

The variance reduction, data RMS and number of used data for each iteration is shown in Figure 44, where grey dots indicate variations for all data and orange dots the variations for used data (without outliers). The number of used data is approximately 17% lower than all data, indicating a moderate amount of outlier (rejected) data during inversion iterations. The used data RMS error drops significantly after the 1$^{st}$ iteration and the total number of iterations (3) results in small data errors. The variance reduction is given by:

$$\mathrm{var.red} = \frac{\mathrm{RMS}_{i-1}{}^{2} - \mathrm{RMS}_{i}{}^{2}}{\mathrm{RMS}_{i-1}{}^{2}} \qquad (3.12)$$

where i stands for current iteration. The variance reduction of the used data is larger than the variance reduction of all data..

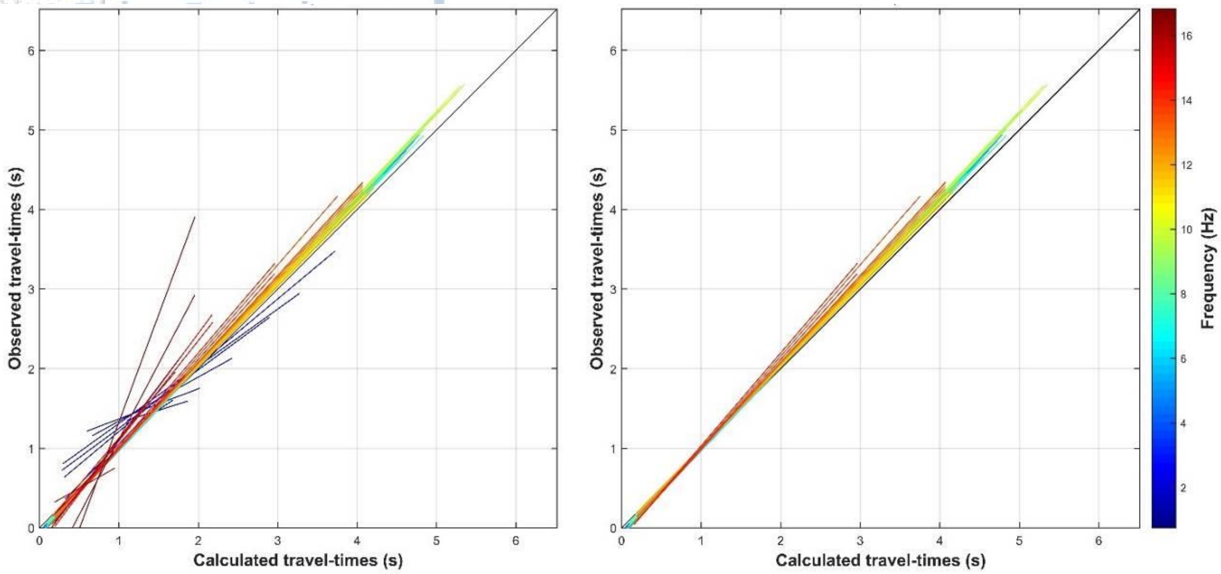


*Figure 43.* Best-fit linear regression trend-lines for the set of examined frequencies before (left) and after (right) frequency rejection.

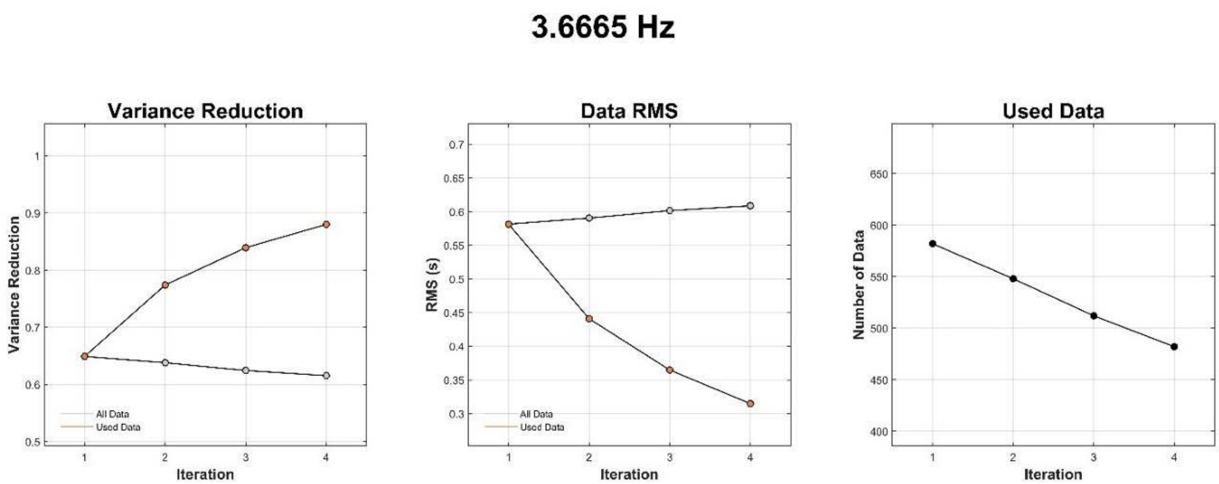


*Figure 44.* Variance reduction, data RMS and number of used data for the frequency of 3.67 Hz.

### 3.4.1.2 Travel-time dependence on inter-station distance and inter-station angle

The implemented inversion scheme resulted in rather small residuals between observed and synthetic travel-times, respectively is restricted to either small and large travel-times, as shown by Figure 45 where the residuals versus observed travel-time are presented for each model (1D, 2D and 3D). The 3D model results, also indicate that rejected data tend to have larger deviations for small and large observed travel-times. The 2D model residuals tend to have larger deviations, while the 1D model residuals exhibit a pseudo-linear trend, due to the different effect of bedrock and sediments in the high- and low-frequency travel-times. Also, 3D model residuals are (in general) smaller than 1 sec, while 2D and 1D model residuals show a rather larger dispersion (less than 2 sec and more than 2 sec, respectively).

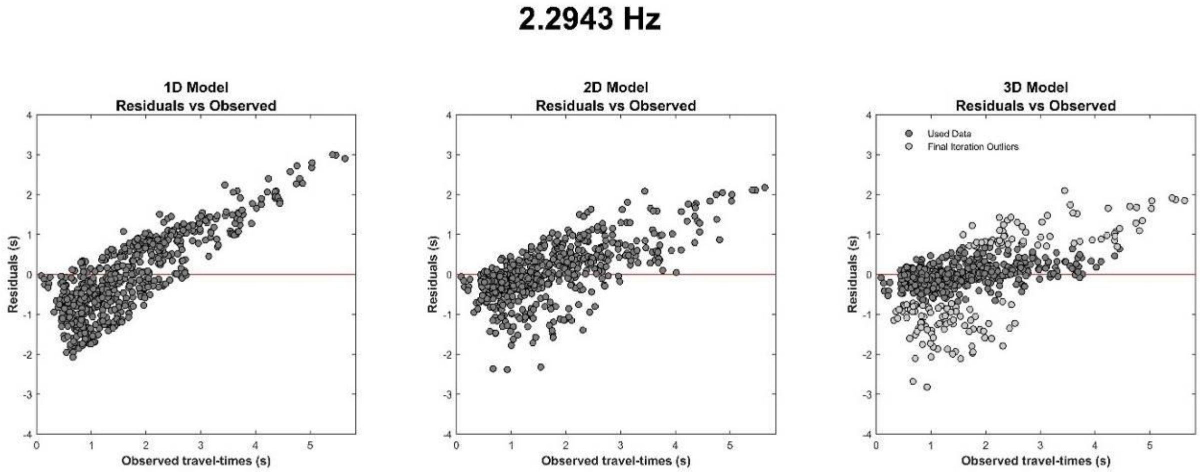


***Figure 45.*** Residuals versus observed travel-times for the three models (1D, 2D, 3D) for f = 2.29 Hz. The red line indicates the zero residual level and light grey points inversion outliers (3D model).

The dependence of travel-time residuals on inter-station distance is examined in Figure 46, where travel-time residual values are plotted for three models. The distribution of residuals for the 1D model is significantly broad, with larger residuals corresponding to large inter-station distances. Furthermore, the dependence of travel-times on inter-station angle is examined in Figure 47. The residuals of the 1D model have a rather random distribution with inter-station angle, indicating that there is no dependence. In contrast, residuals of the 2D and 3D models tend to concentrate in local maxima and minima points but with rather small magnitudes and high uncertainties, with outlier data mainly forming these highs and lows. A typical polynomial fit in order to test for azimuthal anisotropy is shown with an orange line in the 3D model plots, showing small amplitudes. The modelling of azimuthal anisotropy would be quite difficult due to the spatial distribution of stations and the amount of data.

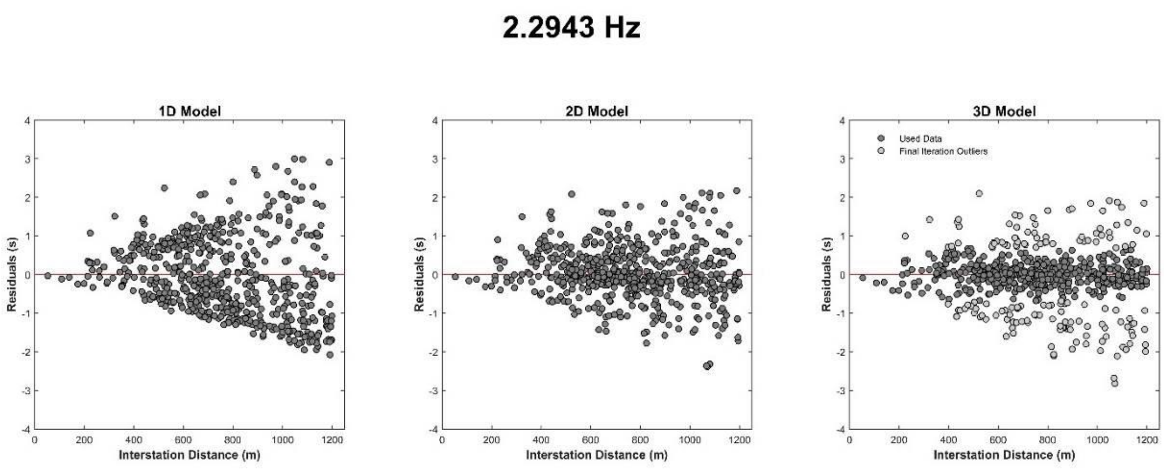


***Figure 46.*** Travel-time residuals versus inter-station distance for the three models (1D, 2D, 3D) for f = 2.29 Hz. Red line indicates the zero residual level and light grey points inversion outliers (3D model).

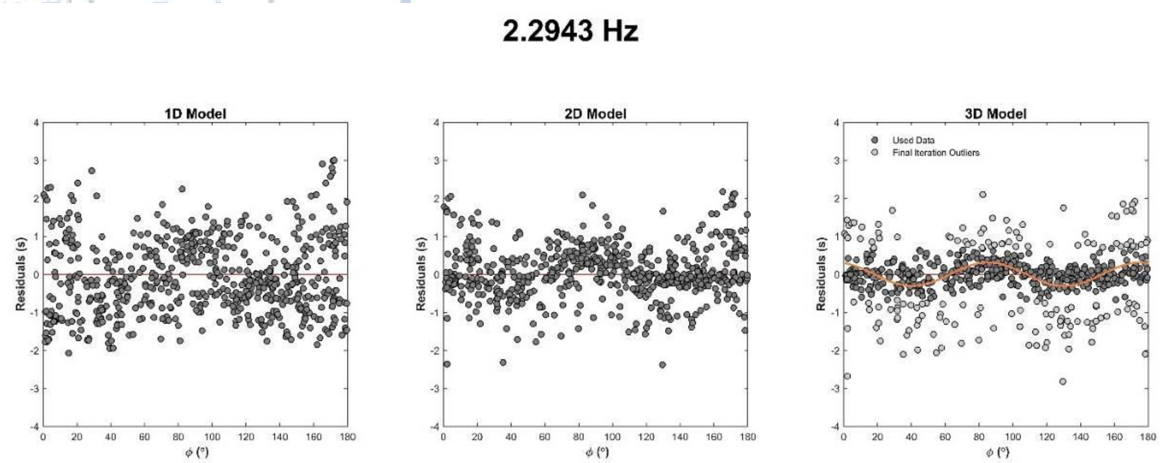


***Figure 47.*** Travel-time residuals versus inter-station angle for the three models (1D, 2D, 3D) for f = 2.29 Hz. The red line depicts the zero travel-time residual level and the orange curve a polynomial fit on the 3D model data.

## 3.4.2. Model errors and resolution

### 3.4.2.1. DWS and spread function

.

A method frequently used to assess the model resolution in seismic tomography is the Derivative Weight Sum (DWS). The DWS is the summation of all the elements of the derivatives weight matrix for each node of the tomographic grid, computed from the ray-tracing procedure. The corresponding distribution provides a better insight of the sampling of each node from ray-paths, since it takes into account the derivatives of the associated paths for each node. Paths with large DWS values tend to be well resolved in comparison with nodes with small DWS values, since they are sampled by more paths. Unfortunately, this method does not give any insight on the azimuthal coverage of each node.

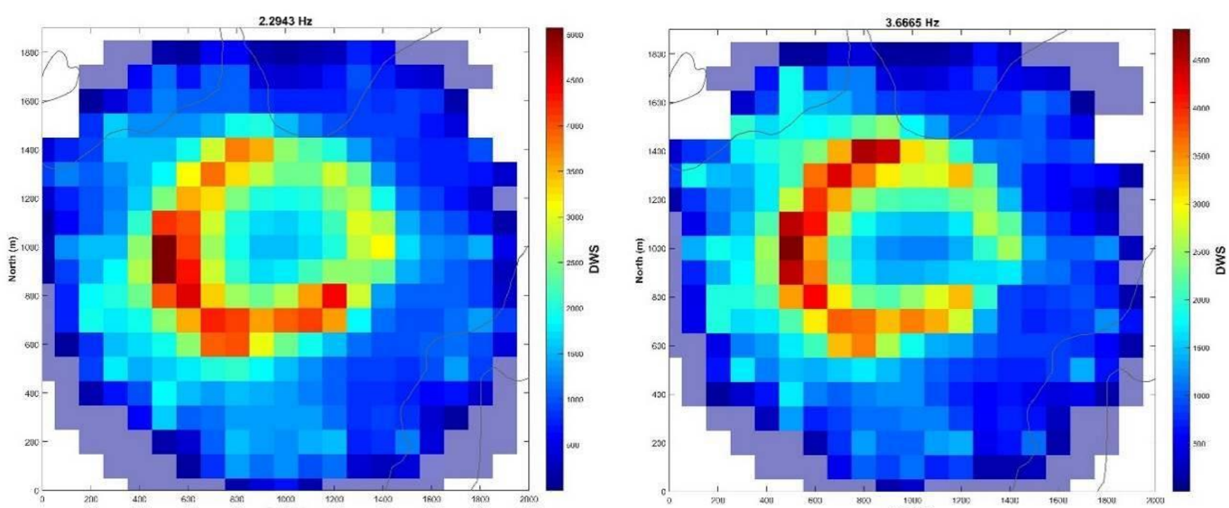


***Figure 48.*** Spatial variation of model DWS for the frequencies of 2.29 and 3.67 Hz. Nodes not satisfying quality cut-off criteria are shown with lighter colors and nodes without values (no rays) with white.

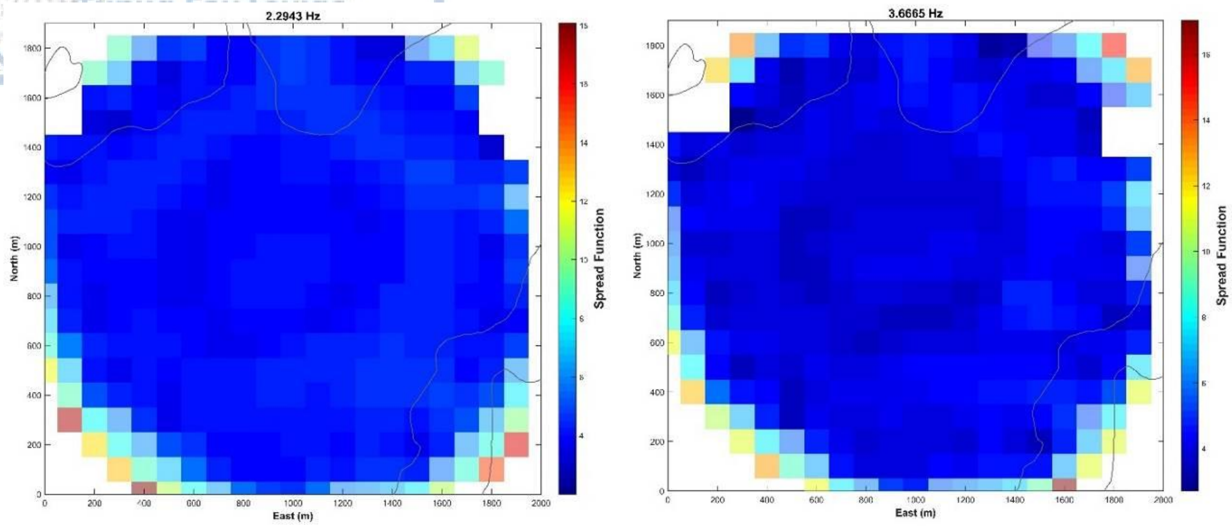


***Figure 49.*** Spatial variation of the Spread Function for the frequencies of 2.29 and 3.67 Hz. Nodes not satisfying quality cut-off criteria are shown with lighter colors and nodes without values (no rays) with white.

Another alternative approach is to consider the Spread Function, SF (e.g. Michelini and McEvilly 1991), which is proportional to the elements of the resolution matrix and their distance. The SF is unit-less and has large values for poor resolved nodes and small values for well resolved nodes. The Spread Function, SF, is computed as:

$$SF = \log\left(|r_j|^{-1} \sum_{k=1}^{M} \left(\frac{r_{kj}}{|r_j|}\right)^2 D_{jk}\right) \qquad (3.13)$$

where $r_j$ is the diagonal element of the resolution matrix of node j (j=1,…,M), $r_{kj}$ is the k$^{th}$ value of the resolution matrix for the same node and $D_{jk}$ is the distance between nodes j and k (k=1,…M). The spatial variation of the model DWS and Spread Functions for each node for the frequencies of 2.29 and 3.67 Hz are shown in Figures 48 and 49. Nodes not satisfying quality cut-off criteria are shown with lighter colors and nodes without DWS values or very poor resolution are shown with white colors.

The derived DWS maps have larger values in the central and the westernmost part of the array, due to the large sampling of these nodes. The movement of the inner circle stations during the network operation created denser path coverage for these nodes. The central part of the array has small SF values, while the external has large SF values, indicating the better resolution of the internal nodes. It is notable that nodes with small DWS values and large SF values are not satisfying the implemented quality cut-off criteria (discussed later). As suggested by other researches (e.g. Toomey and Foulger 1989) the variation of the logarithm of the DWS versus the Spread Function, shows a linear trend and an example is presented in Figure 50 for the frequencies of 2.29 and 3.67 Hz.

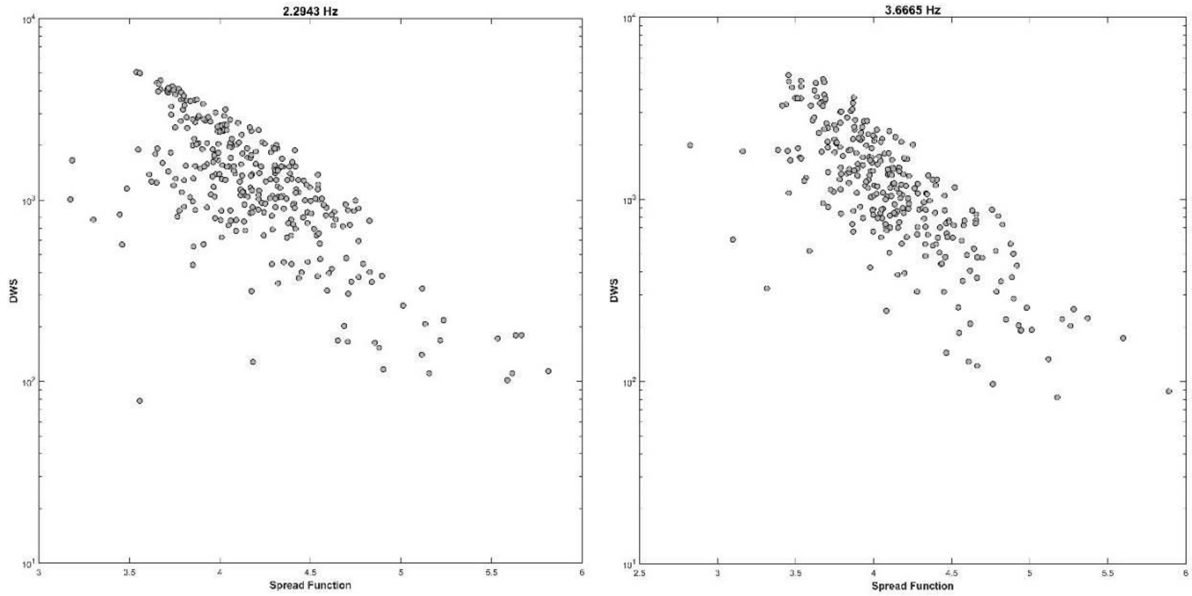


***Figure 50.*** Variation of log(DWS) versus Spread Function for frequencies 2.29 and 3.67 Hz for nodes satisfying quality cut-off criteria.

### 3.4.2.2 Solution quality cut-off criteria

In total, more than 56 frequencies (~0.7 - 16 Hz) were inverted, exhibiting different variation of total data amount and RMS errors (Figure 52). The variation of the number of all data is presented with blue line in Figure 51, while the number of used data (after outlier rejection) with a red line. The RMS of all data is also shown with a black line and the RMS of used data with green line. This figure suggests that for small (<1.2 Hz) and large (>12 Hz) frequencies the number of used data is almost identical to the number of all data and therefore the inversion procedure does not reject almost any data. In contrast, a larger amount of data is rejected for intermediate frequencies. The RMS of used data is significantly lower than the RMS for all data, with RMS errors being smaller than ~0.4 sec. Therefore, frequencies smaller than 1.2 Hz and larger than 12 Hz were rejected, as also suggested by Figure 43.

Solution quality cut-off criteria were implemented to reject nodes with large uncertainties. Thus, the variation of group slowness error versus hitlength and resolving length versus hitlength diagrams were used to detect these quality criteria limits. The Spread Function computations usually leads to strict estimates of the model resolution (e.g. Toomey and Foulger 1989), so the resolving length was computed by the formula:

$$\text{Res.Length} = |r_j|^{-1} \sum_{k=1}^{M} \left( \frac{r_{kj}}{|r_j|}^{2} D_{jk} \right) \tag{3.14}$$

The computed resolving length has length units (meters). Similar to the Spread Function, nodes with large resolving lengths are poorly resolved compared to nodes with small resolving lengths. The variation of the resolving length with the logarithm of ray hitlength and the variation of the group slowness error with the logarithm of the total hitlength for frequencies of 2.29 Hz and 3.67 Hz are shown in Figures 52 and 53, respectively. Both variations display a rather linear trend between the associated quantities, whereas rejected data (displayed with red dots) display a rather sparse distribution. Nodes with hitlength smaller than 70 m or group slowness error larger than $3.5x10^{-4}$ s/m or resolving length larger than 500 m were rejected due to their poor resolution quality.

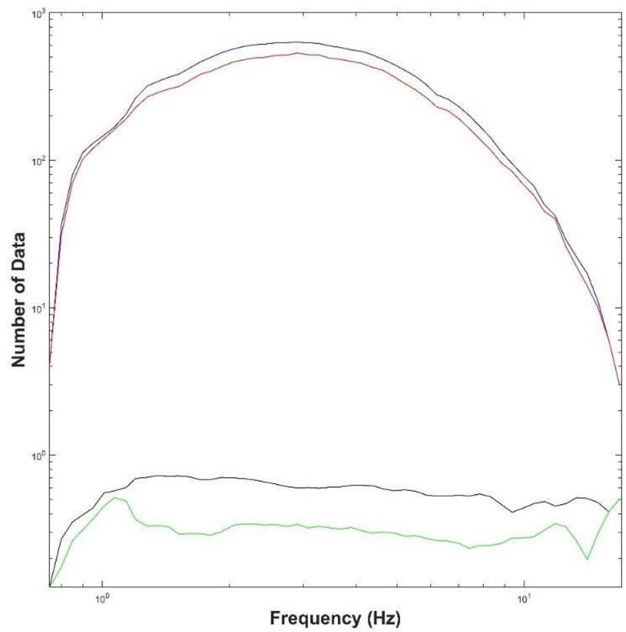


***Figure 51.*** Variation of the total number of data (blue line), number of used data (red line), RMS of all data (black line) and RMS of used data (green line) with frequency.

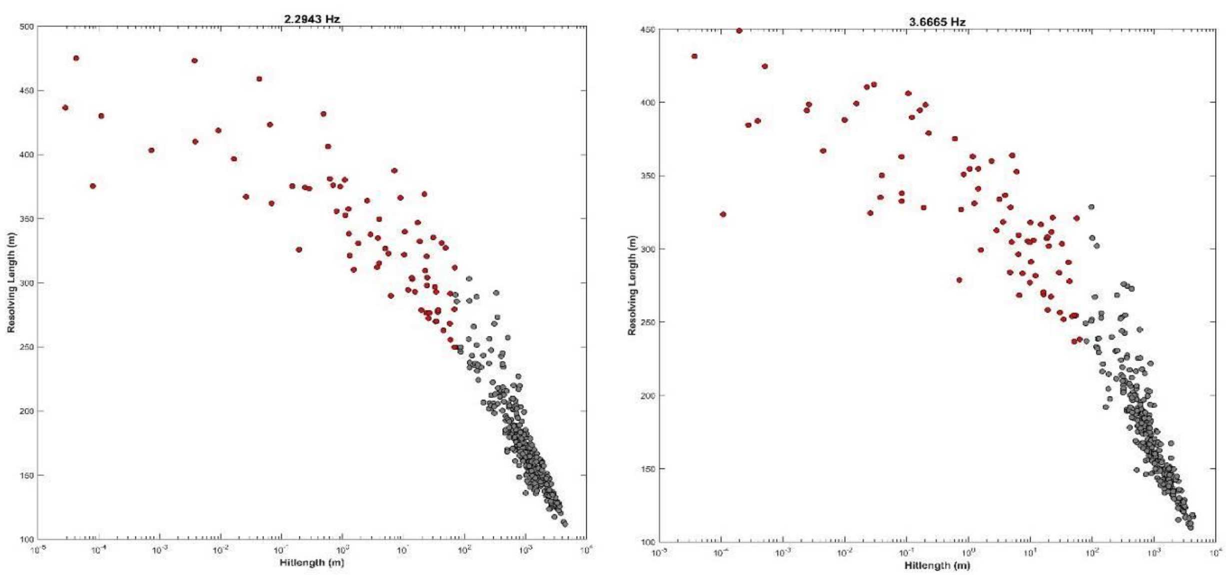


***Figure 52.*** Variation of the resolving length of each node versus the logarithm of the total path hit length for frequencies 2.29 and 3.67 Hz. Red dots indicate nodes rejected from the quality cut-off criteria.

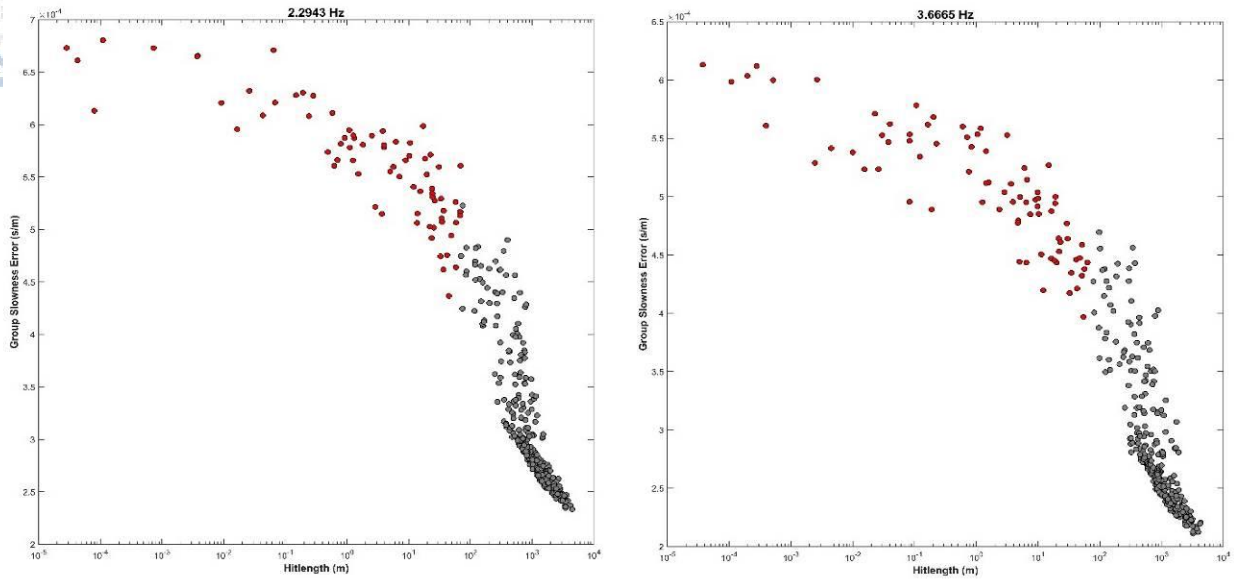


***Figure 53.*** Variation of the group slowness error of each node solution versus the logarithm of the total path hitlength for frequencies 2.29 and 3.67 Hz. Red dots indicate nodes rejected from the quality cut-off criteria.

### 3.4.2.3 Spatial variability of data and model errors

The spatial variation of the rejected ray paths from the tomographic inversion procedure for each iteration were plotted in Figure 54 for an indicative frequency (3.67 Hz). The resulting images show that the rejected ray paths (red paths) are concentrated mainly in the western part, where the acquired travel-time also tend to have larger errors. Also, this figure depicts that paths which were rejected during an iteration step were later accepted in the next iterations, due to the convergence of the model to solutions which generated synthetic travel-times with smaller residuals, compared to previous iterations. Also, the spatial variation of the rejected data standard deviation ratio against the data RMS error ratio is shown in Figure 55. The derived images show that rejected data concentrate mainly in the southern part of the model. The increase of the quantity n*RMS is significant between different iteration steps, mainly affected by the RMS drop and large model corrections between different iteration steps (small model convergence rate between the solution of each iteration and the final solution).

The information presented in this section suggests that the southernmost and westernmost part of the array is associated with large amount of data rejection and data errors. The data with large errors (compared to the RMS value) are rejected in the inversion process during the 1$^{st}$ or 2$^{nd}$ iteration and the magnitude of n*RMS increases rapidly, as the model RMS decreases. Despite these uncertainties, the derived tomographic results are in good agreement with local geology and reliable information has been retrieved regarding the Love wave group velocities.

The derived results for Love wave group slowness and model resolution (Spread Functions and DWS for each node) are presented in Figures 56, 57 and 58 as seven pseudo cross-sections. The results are presented with respect to the local Cartesian distance and period (roughly proportional to depth), for the whole frequency band (~0.7 – 16 Hz), while nodes not satisfying quality cut-off criteria are not plotted.

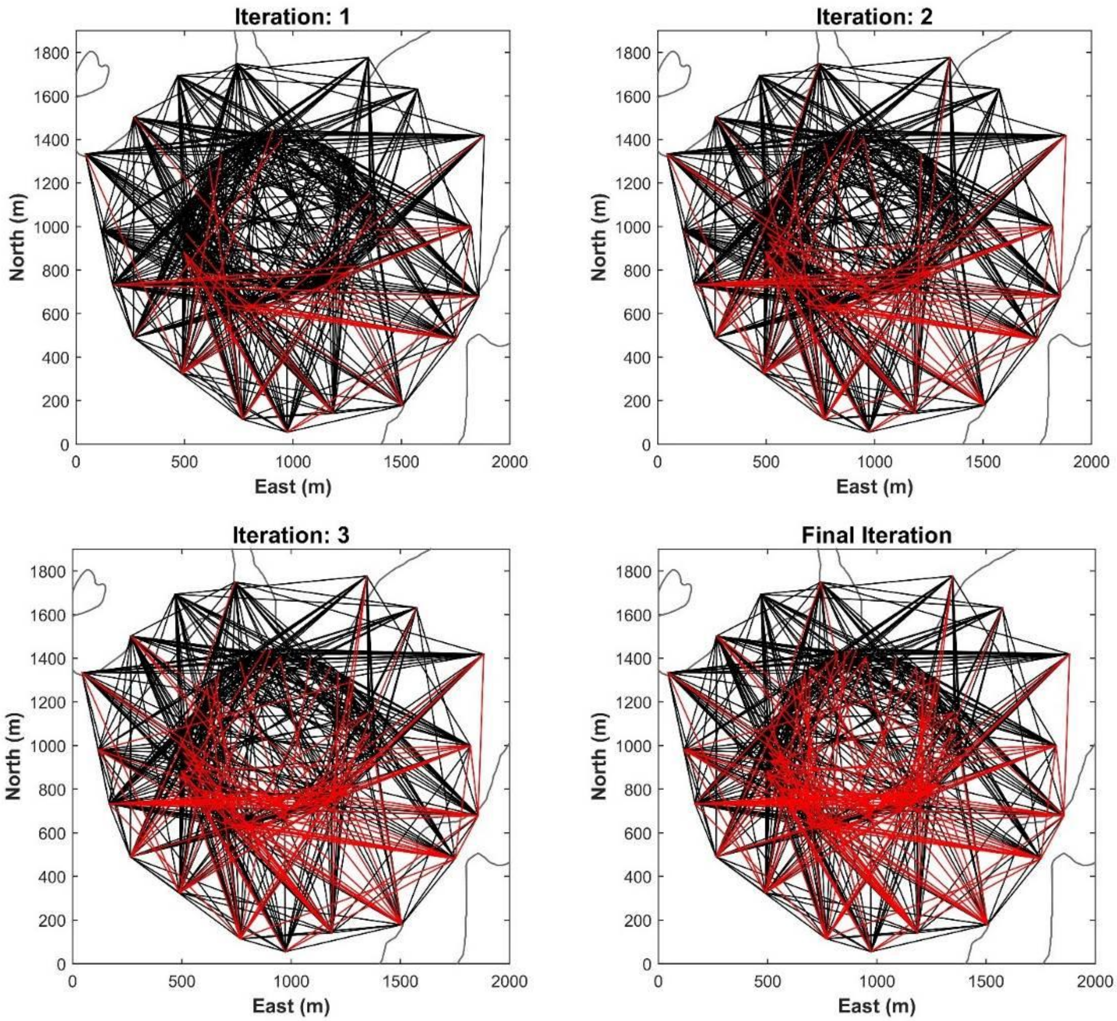


***Figure 54.*** Spatial variation of rejected ray paths (red lines) during different inversion iterations for f = 2.29 Hz.

The obtained Love wave group slowness results are in good agreement with local geology and tectonics. The pseudo cross-sections normal to the 2D trend of the basin (S1-S3) show that for small distances (southern part of the model) the obtained group slowness values are large (small group velocities), corresponding to the sedimentary deposits (pre-Mygdonian and Mygdonian system). Their pseudo-depth gradually decreases as we move towards the northern part of the array, in good agreement with the expected sediment thickening in the southern part, due to the generation of depositional space from the activity of neotectonic faults. In contrast, for large profile distances, the derived group slowness values are small (large group velocities), indicating shallow bedrock depths. The cross-sections parallel to the 2D basin geometry (S4-S6) give an insight of the pseudo-lateral variations of the sedimentary deposits, with a good coverage of large periods for the southern part of the model, adequate but rather unstable for the mid-part and almost absent for the northern part, in very good agreement with the local geology. The pseudo cross-section AB is parallel to the EUROSEISTEST section presented in Chapter 1 and presents similar information.

The spatial variation of the Spread Function indicates that for large periods the SF has large values, in good agreement with the uncertainties for such depths due to their penetration from large wavelengths. The variation of the SF values in all cross-sections suggests that the bedrock group slowness values tend to have larger resolution errors than sedimentary deposits, while model resolution tends to be poorer in the easternmost part of the model. It is notable that the results of the northern part were rejected from the implementation of resolution quality cut-off criteria, where information is absent regarding travel-times, due to the lack of capacity of the array to record wave-lengths penetrating and sampling large bedrock depths.

It should be noticed that large DWS values are higher for the central part of the array due to the dense path coverage from the movement of the sensors during the network operation (sections S1-S3, S5 and especially seen on cross-section AB). The DWS values strongly decrease with periods (or equivalently with depth) in the southern part of the model, corresponding to lack of information for larger depths due to the lack of noise sources providing large wavelengths. Also the western part DWS values are larger than those for the eastern part, pointing out to the different ray path coverage. Finally, the DWS values for bedrock are smaller than the corresponding values for sediments, due to the rather poor network coverage in the bedrock area.

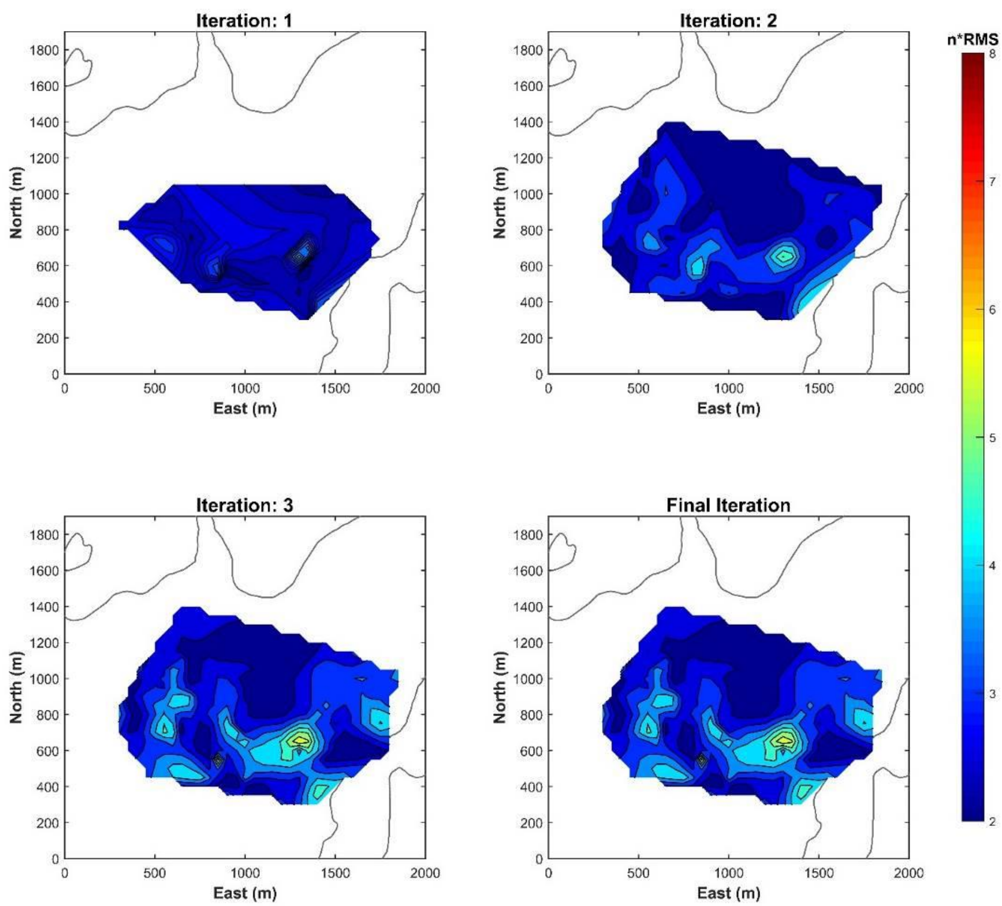


***Figure 55.*** Spatial variation of the data error, expressed as number of RMS values (n*RMS) and for different inversion iterations for the frequency of 2.29 Hz.

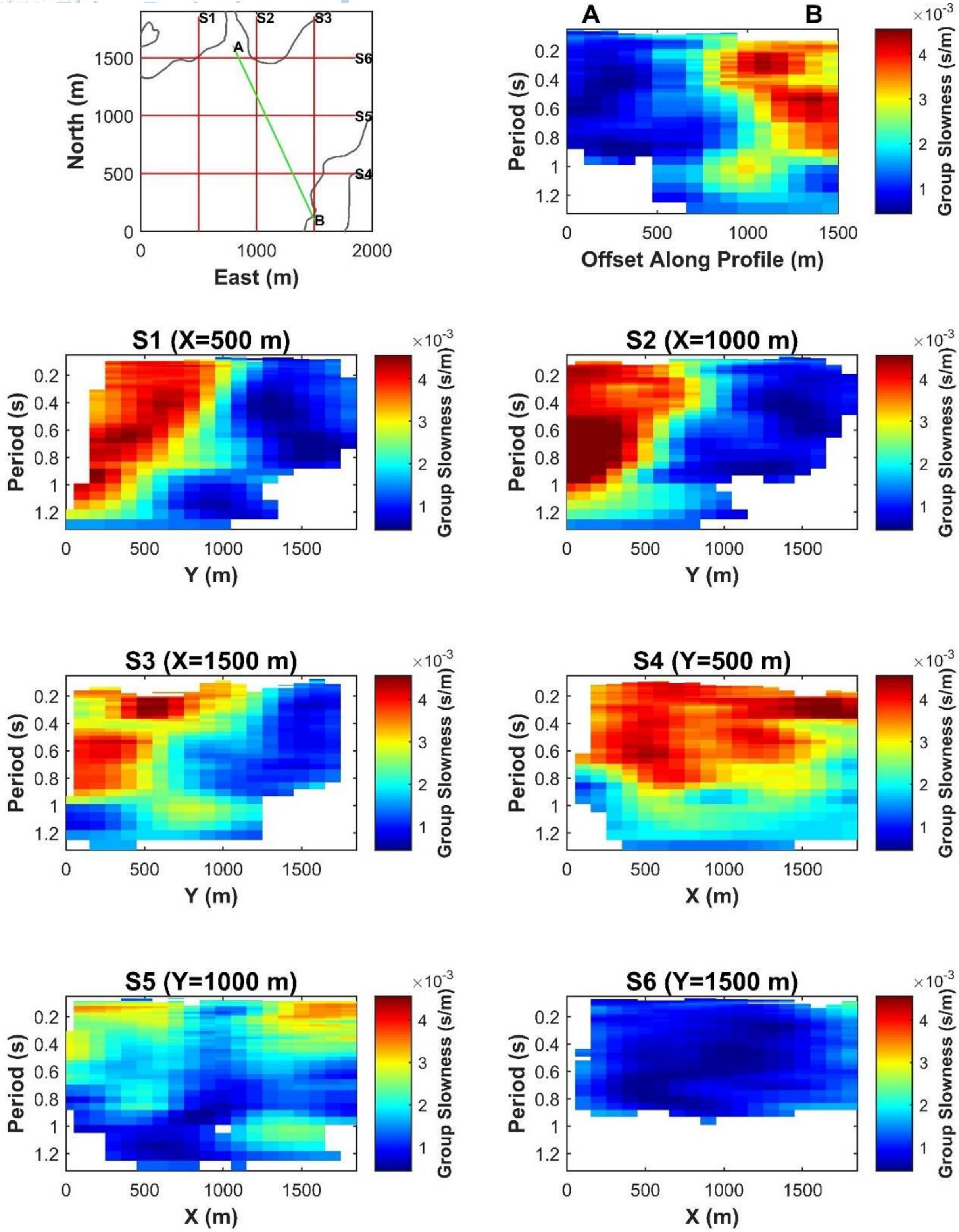


***Figure 56.*** Pseudo cross-sections of the derived group slowness tomographic results with period (roughly proportional to the penetration depth). S1-S3: Parallel to the Y axis sections, S4-S6: Parallel to the X axis sections and AB: EUROSEISTEST cross-section. Solutions not satisfying quality cut-off criteria are not plotted.

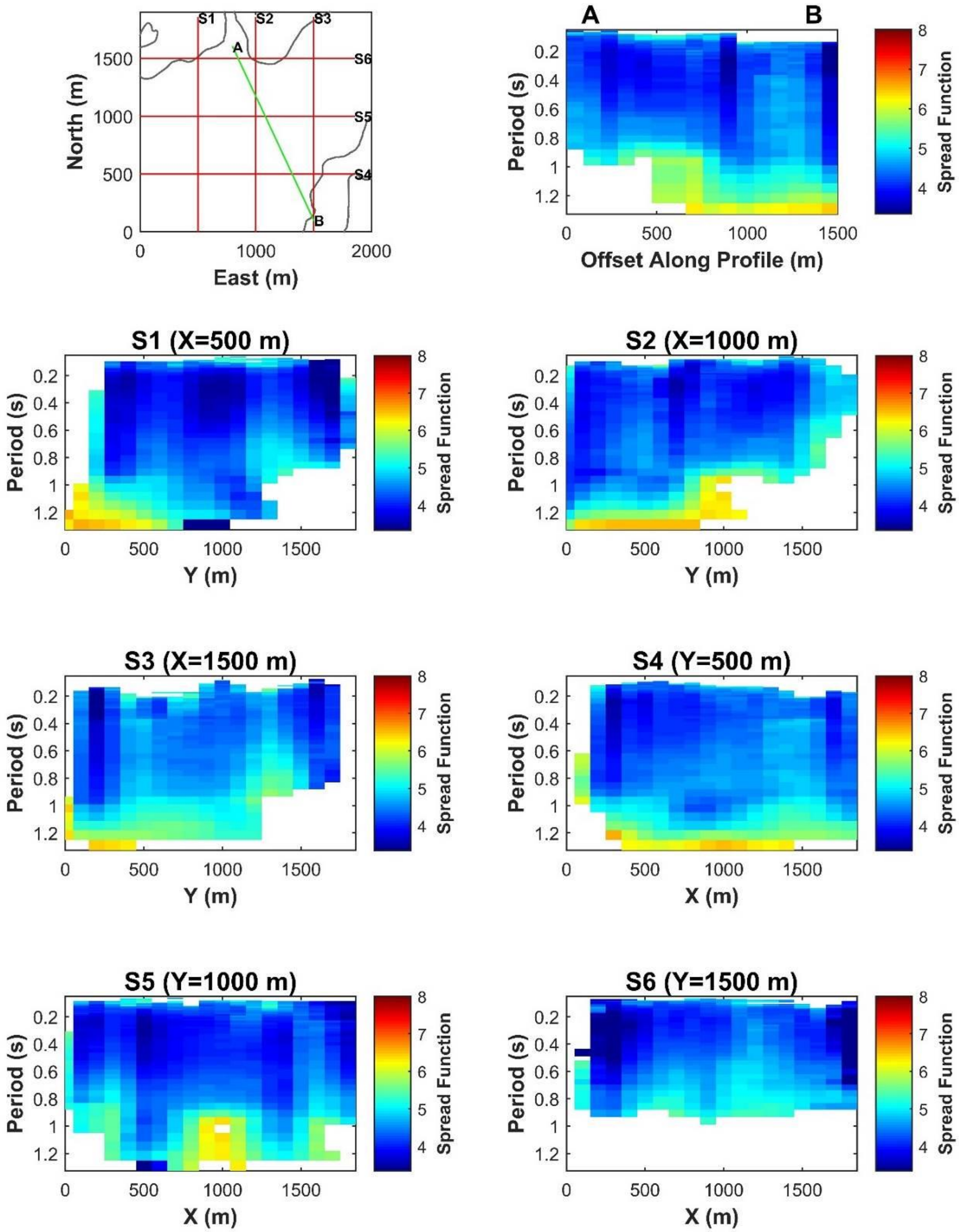


***Figure 57.*** Pseudo cross-sections of the Spread Function values computed for each tomographic node with period (roughly proportional to the penetration depth). S1-S3: Parallel to the Y axis sections, S4-S6: Parallel to the X axis sections and AB: EUROSEISTEST cross-section. Solutions not satisfying quality cut-off criteria are not plotted.

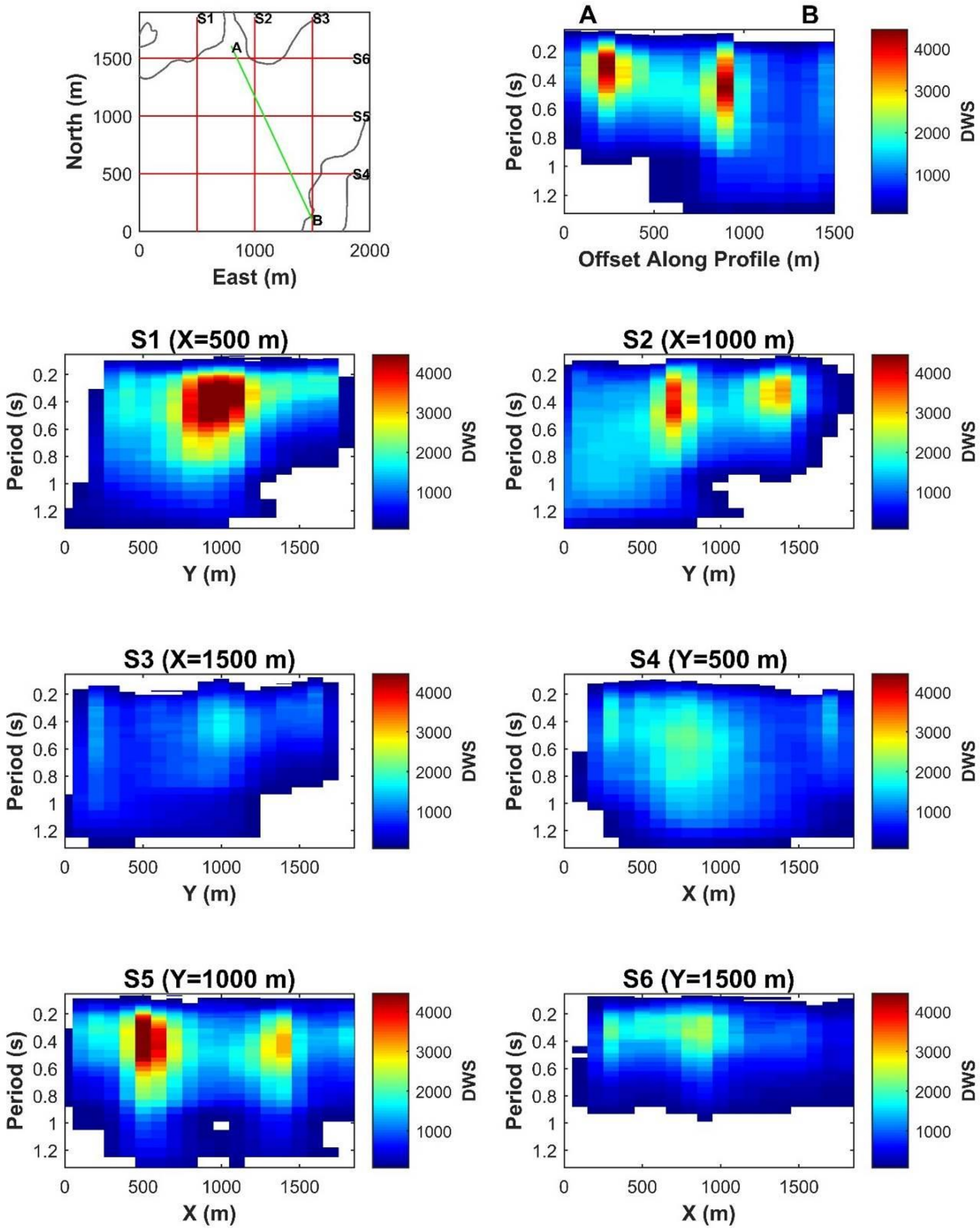


***Figure 58.*** Pseudo cross-sections of the DWS values computed for each tomographic node with period (roughly proportional to the penetration depth). S1-S3: Parallel to the Y axis sections, S4-S6: Parallel to the X axis sections and AB: EUROSEISTEST cross-section. Solutions not satisfying quality cut-off criteria are not plotted.

## 3.5. Travel-time tomography with inter-frequency constrains

The results presented and discussed earlier were based on the solution of the linear system of the equation 3.3, for each frequency independently. To improve the reliability of the results, an additional inter-frequency constrains were introduced in the tomographic system in order to obtain smooth Love dispersion curves, following Hannemann et al. (2014). Therefore, the following system was solved:

$$\begin{bmatrix} \mathbf{L} \\ d\mathbf{I} \\ \varepsilon\nabla_{xy}^{2} \\ \lambda\nabla_{f}^{2} \end{bmatrix} \mathbf{s} = \begin{bmatrix} \mathbf{t} \\ 0 \\ 0 \\ 0 \end{bmatrix} \tag{3.15}$$

where λ is the additional inter-frequency constrains.

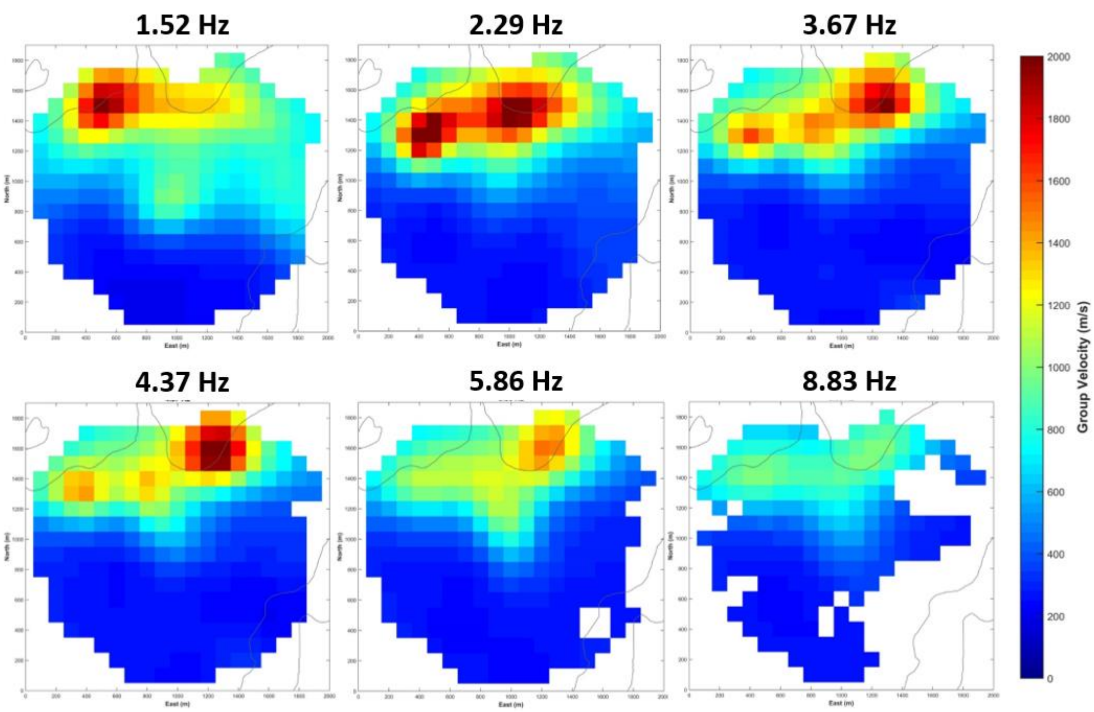


***Figure 59.*** Love wave group velocity maps for six typical frequencies from the tomographic inversion of travel-times using inter-frequency smoothing constrains. Nodes not satisfying resolution quality cut-off criteria are not plotted.

Following this approach, the derived spatial variation of Love wave group velocities is similar to the one obtained without the implementation of inter-frequency constrains. As expected, the observed spatial variation of Love wave group velocities (Figure 59) identifies the main geotectonic features of the basin, featuring a significant velocity contrast (~700 m/s) between the northern (faster) and southern (slower) nodes of the tomographic grid. The resolution of southern nodes is limited for higher frequencies, indicating the high anelastic attenuation of Love waves propagating in Holocene / Quaternary deposits, while the resolution of northern nodes is limited for lower frequencies, implementing the inadequate propagation of large wavelengths in the bedrock area. The obtained results were used to reconstruct local group slowness dispersion curves for each node of the grid for the considered frequency band.

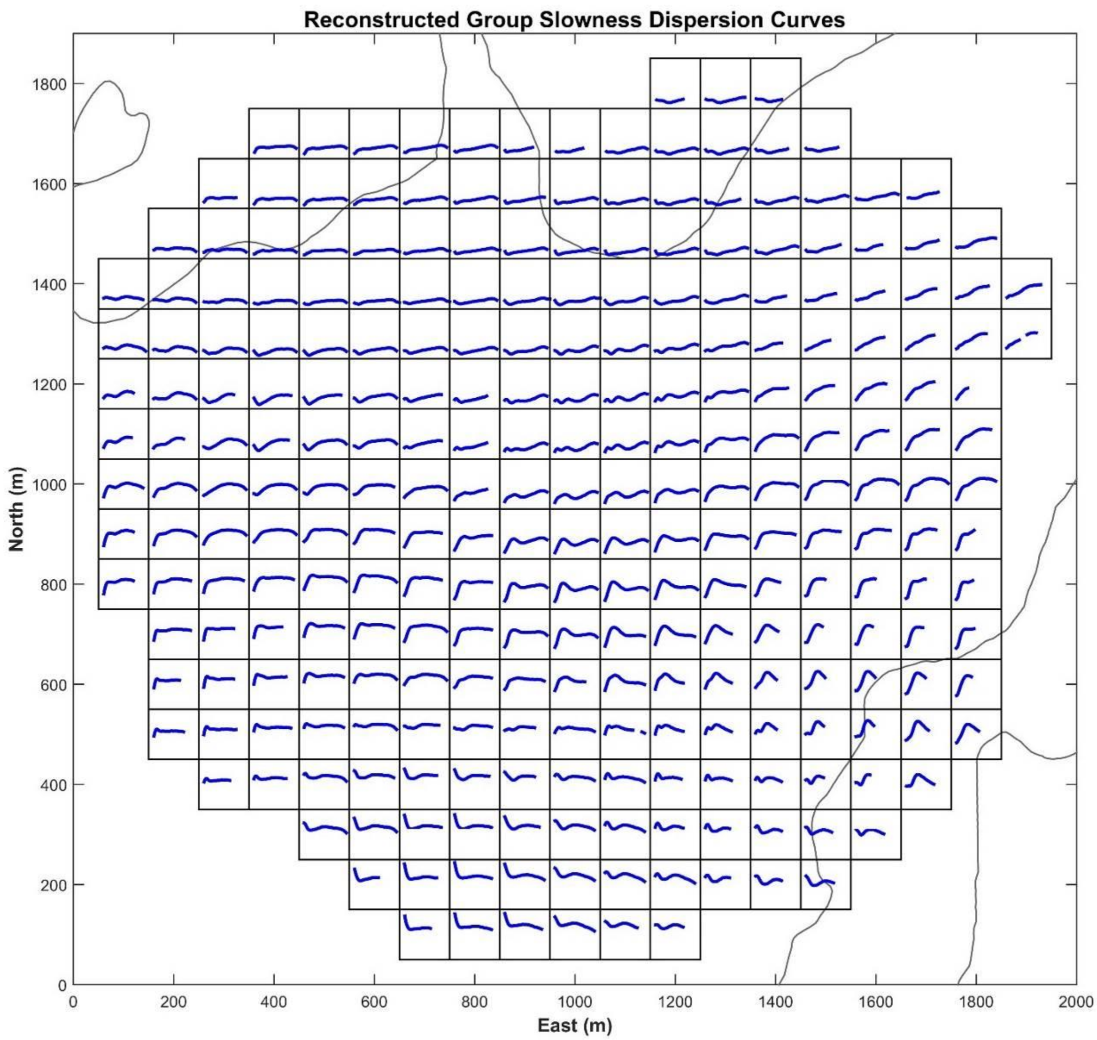


***Figure 60.*** Reconstructed Love wave group slowness dispersion curves for each node of the tomographic grid. The local horizontal axis for each node varies between 1.27 and 11.82 Hz (in logarithmic scale) in East (X) while the vertical axis between 0 and $3x10^{-4}$ s/m. Only solutions satisfying quality cut-off criteria are shown and each node dispersion curve presented has at least 10 points.

Inversion solutions for three values of the inter-frequency constrain multiplier (0, 2000 and 5000) for a southern and a northern node of the study area are presented in Figure 61. The group slowness dispersion curves that resulted without the implementation of inter-frequency smoothing (λ=0) exhibit rather anomalous variations. The reconstructed local dispersion curves are significantly smoother with the implementation of inter-frequency constrains (blue and green dots in Figure 61). In general, solutions not satisfying quality cut-off criteria are quite common among all three cases (white dots).

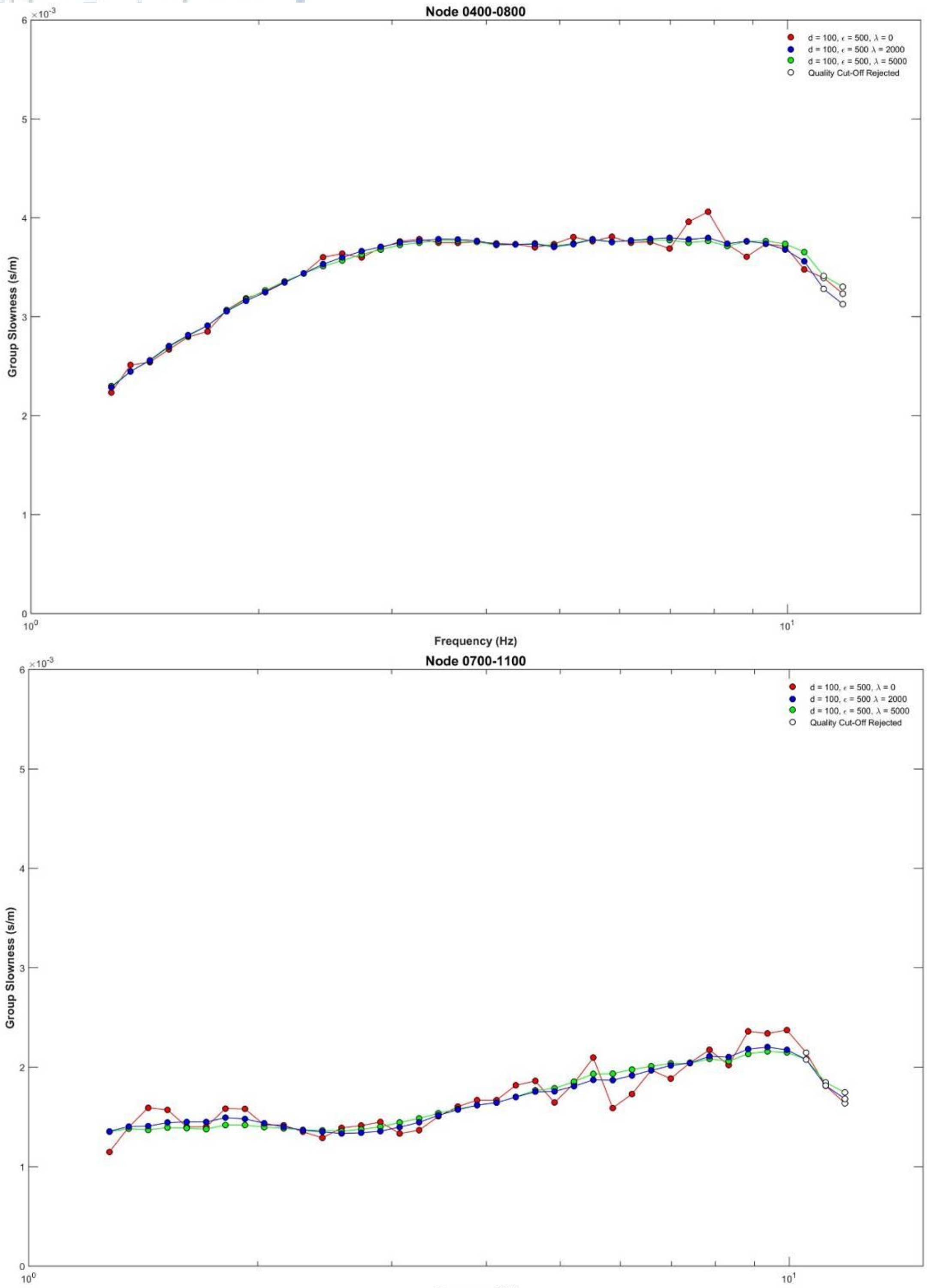


***Figure 61.*** Group slowness results for a southern node (X:400, Y:800, top figure) and a northern node (X:800, Y:1100, bottom figure) of the tomographic grid for different inversion schemes. Red dots depict Love wave group slowness values for inversion without inter-frequency constrains, blue for inter-frequency smoothing constrain value of 2000 and green for 5000, while white dots correspond to results not satisfying quality cut-off criteria.

## 3.6. 1-D Inversion of local group slowness dispersion curves

The resulting reconstructed local group slowness dispersion curves (Figure 61) are affected by the main basin features, exhibiting small group slowness values in the northernmost part of the array (where bedrock outcrops) and large in the southernmost (pre-Mygdonian / Mygdonian system sediments). Although the 2-D group velocity maps with (Figure 60) and without (Figure 36) inter-frequency constrains give an insight regarding the main basin geological features, they do not provide information about actual shear velocities (Vs) and their depth variation. To better understand these factors, a 1-D inversion approach of the local group slowness dispersion curves was adopted, following the approach of Hannemann et al. (2014).

To find a suitable 1-D model of Vs depth variation for each node a directed Monte Carlo algorithm was adopted, using the Neighborhood Algorithm (Sambridge 1999a; 1999b). The program package Geopsy (www.geopsy.org) was used for this purpose, which uses the implementation of Wathelet (2008). The Neighborhood Algorithm is adapted to resolve the inversion non-uniqueness problem and escape local minima. The 7UL-2 model parameterization of Hannemann et al. (2014) was used, since it generated the most reliable layer depth results for Rayleigh waves, compared to the other tested model parameterizations. For each node 100.000 ground profiles were generated and the layer bottom depths were computed from averaging the ground model solutions which had misfits with less than 1 standard deviation from the best-fit solution. The resulting average bottom layer depths are presented in Figure 62.

In general, the Mygdonian system sediments (layers A-D in Table I and Figure 8, roughly corresponding to layers with fixed Vs = 150, 250, 350 and 425 m/sec) have small thicknesses, which increase as we move towards the southern part of the model and exhibit significant thicknesses for layers with fixed Vs = 350 and 425 m/sec. The Mygdonian system sediments are absent in the northern part, which is dominated by the outcropping bedrock. The pre-Mygdonian system sediments (layers E-F in Table I and Figure 8, roughly corresponding to layers with fixed Vs= 600, 700 and 800 m/sec) have reasonable thicknesses in the southern part of the model. The pre-Mygdonian system sediments / bedrock discontinuity (Vs = 800 m/sec) has an average depth of ~200 m in the south. While the main basin characteristics are well resolved, results for several nodes exhibit local instabilities and inversion results derive larger average bottom layer depths for these specific nodes.

To examine local instabilities, the observed local group slowness dispersion curves and the synthetic group slowness dispersion curves for four nodes are presented in Figure 63. The first three nodes correspond to a northern (X: 800, Y: 1400), a central (X: 1000, Y: 700) and a southern (X: 1400, Y: 200) node, while the fourth (X: 500, Y: 500) node derived unrealistic large average bottom layer depth results. The local group slowness dispersion curves derived from travel-time tomographic inversion without inter-frequency constrains are also shown for comparison (red marks), while the group slowness dispersion curves with a λ = 2000 inter-frequency smoothing parameter and their errors are shown with blue colors. The synthetic group slowness dispersion curves (black lines) correspond to the minimum misfit ground profile from the 1-D inversion. It is clear that for the problematic nodes (e.g. X:500, Y:500) the 1-D inversion approach was not able to derive a reliable model (with and without inter-frequency smoothing constraining), especially for small frequencies.

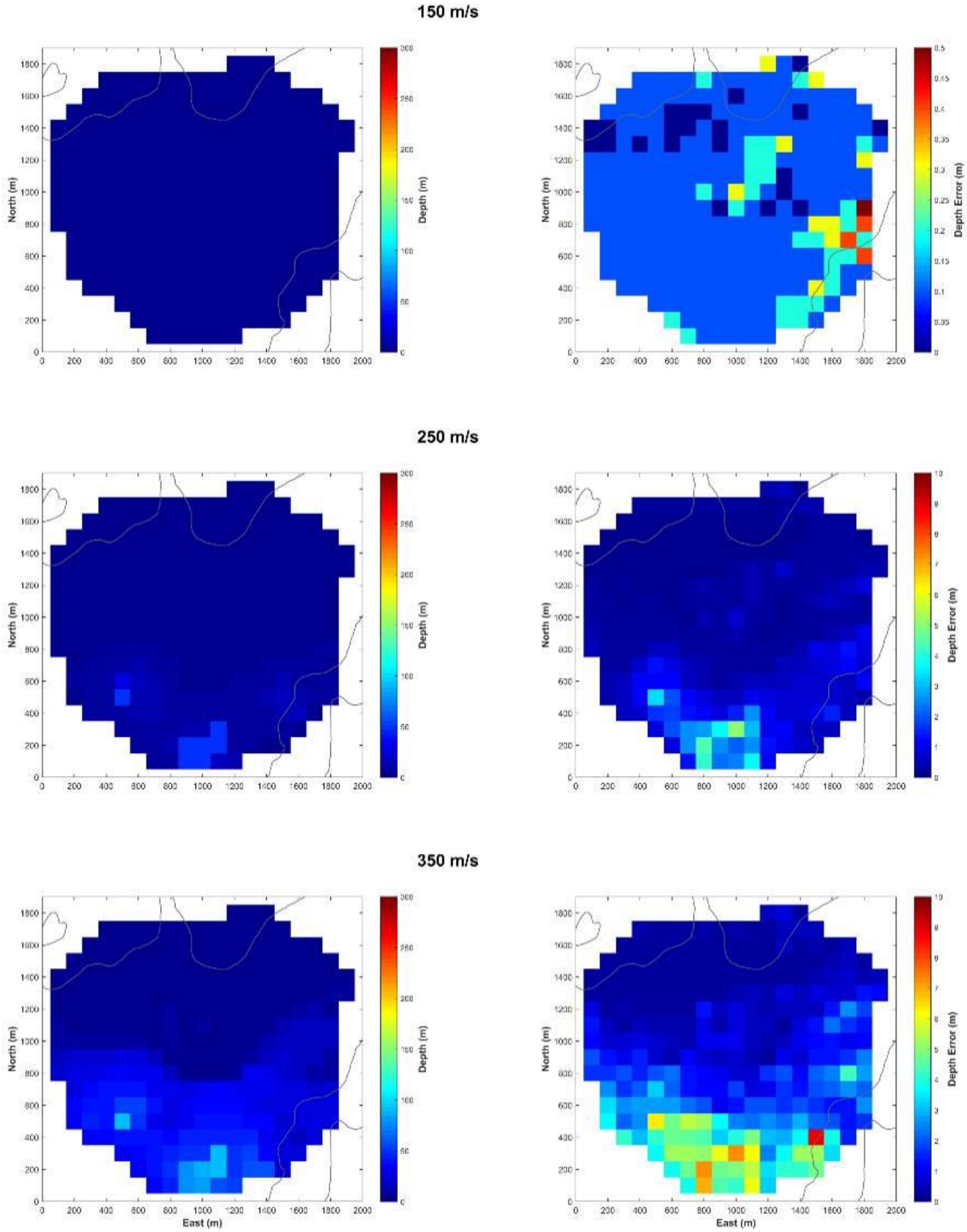


***Figure 62.*** Resulting average bottom layer depths for 7UL-2 model parameterization from *Hannemann et al. (2014)* from the 1-D inversion of local group slowness dispersion curves (left) and their errors (right).

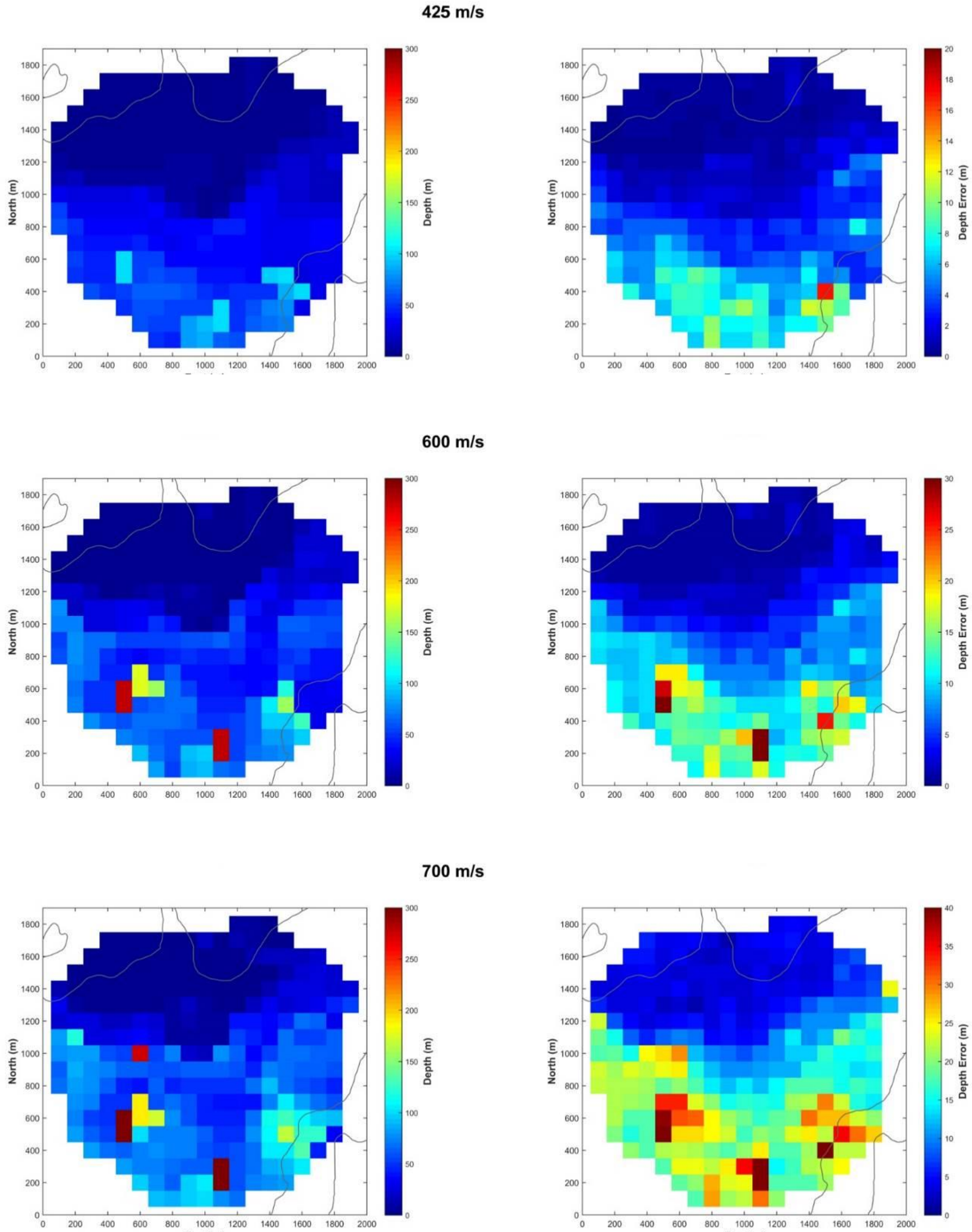


***Figure 62-continued***

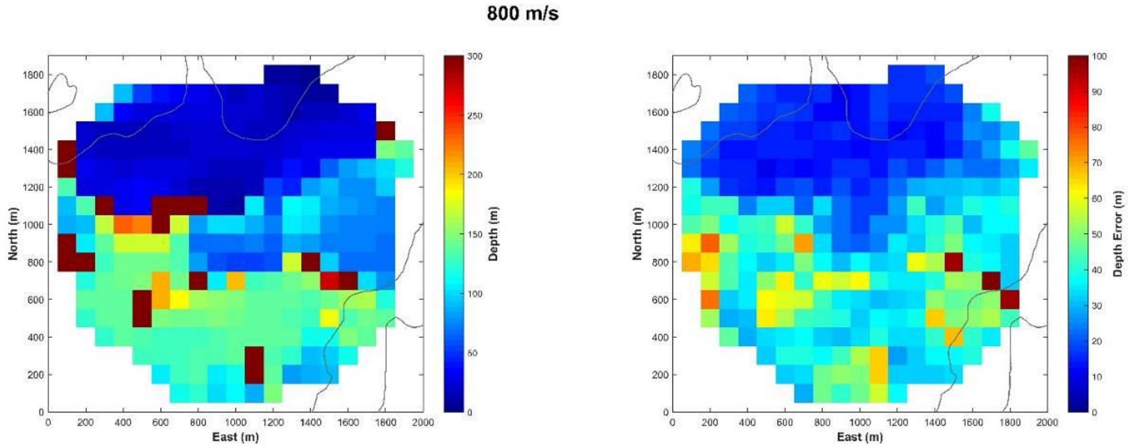


***Figure 62-continued***

The 2-D variation of average bottom layer depths from the 1-D inversion of local group slowness curves without inter-frequency smoothing led to similar results. Local instabilities were also observed mainly for layers with large Vs velocities (deeper formations) with bedrock depths up to the maximum allowed depth in the model parameterization (500 m). The spatial variation of local instabilities tends to be completely random for both cases, mainly affecting southern nodes, implying that the inversion scheme could not sample the model space with efficient accuracy and find a model which fits the observed local dispersion curves mainly for small frequencies. Since each node is inverted independently, the adopted inversion scheme could not generate a smooth pseudo-3D Vs model for the area.

The derived halfspace Vs velocities from the 1-D inversion of local group slowness dispersion curves with and without inter-frequency smoothing are presented in Figure 64. The observed halfspace velocities are larger in the south (mean value ~ 2000 m/sec) and smaller in the north (mean value ~ 1000 m/sec), indicating a good agreement with local geology and the expected sediment thickening in the south. The resulting halfspace velocities also exhibit local instabilities for both cases, with the residuals between the two datasets being almost normally distributed. It is notable that local instabilities are mainly distributed in the southern part of the study area, while in the north they are almost absent.

The maximum resolving depth was assumed to be equal to the half maximum wavelength for each node. Since group slowness were inverted, the maximum wavelength for each dispersion curve was assumed to be equal to the wavelength of the maximum group slowness for each frequency. To obtain a better understanding of the derived pseudo-3D Vs model, a cross-section parallel to the EUROSEISTEST cross-section was estimated. The resulting cross-section and the maximum resolving depths are presented in Figure 65. The results are in good agreement with those from Hannemann et al. (2014) and resolve the main basin structures, with small sediment thicknesses in the north and larger as we move towards the south. The fault F1 position is observed at ~500 m horizontal distance along the profile, closer to the basin center than the proposed position by Raptakis et al. (2010). The fault F2 position is not recognized in the resulting cross-section and, as suggested by Hannemann et al. (2014), it possibly does not affect shallow sedimentary formations. The maximum resolving depths are shallower in the south and exhibit large depths in the north. It is notable that local model instabilities that resulted in deeper and unrealistic layer depths in the south are often larger than the maximum resolving depths.

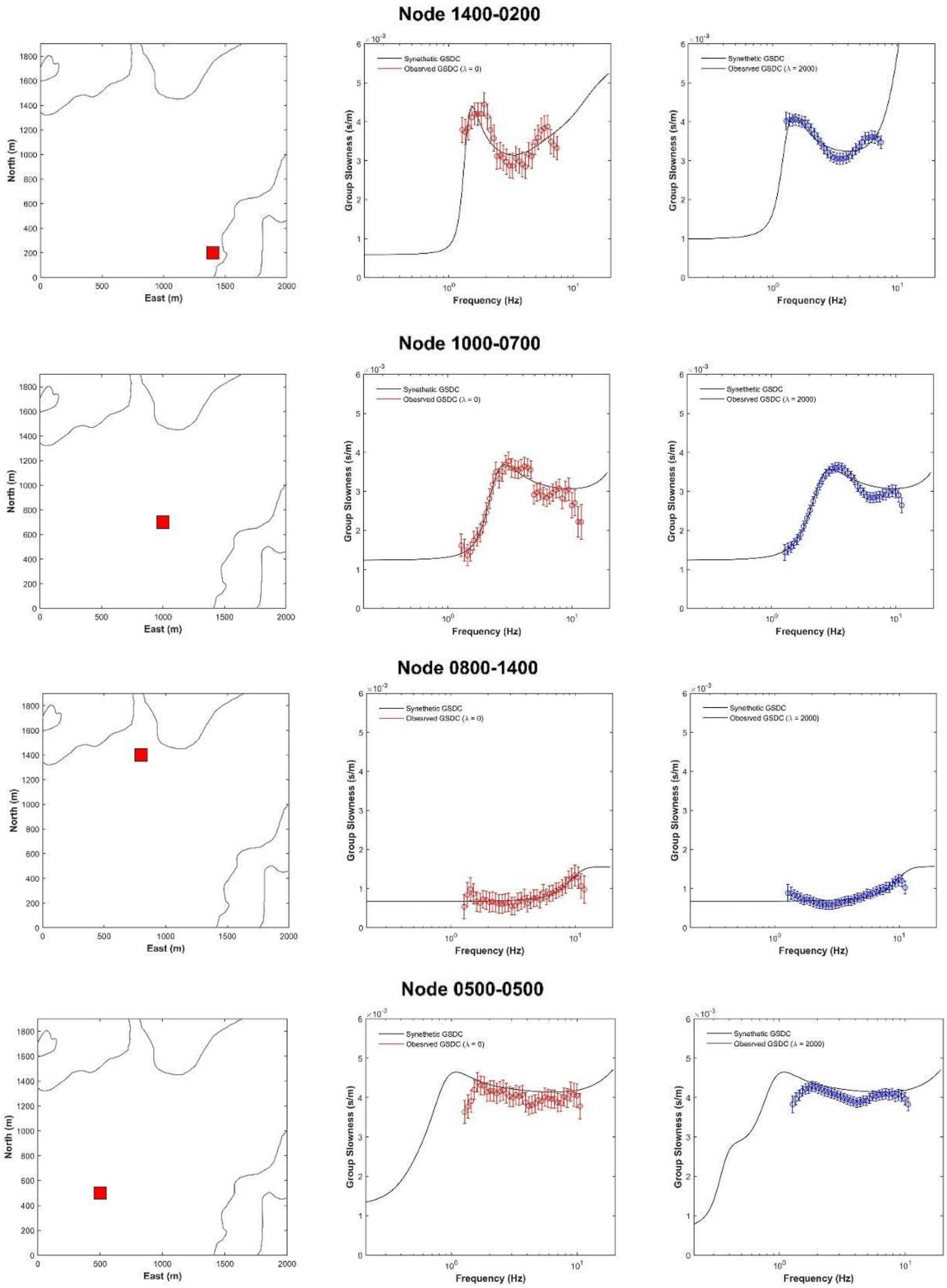


***Figure 63.*** Comparison between synthetic and observed group slowness dispersion curves for four nodes. Red curves correspond to group slowness results without inter-frequency smoothing and blue with λ = 2000 inter-frequency smoothing parameter. Black lines indicate synthetic group slowness curves for minimum misfit ground profile.

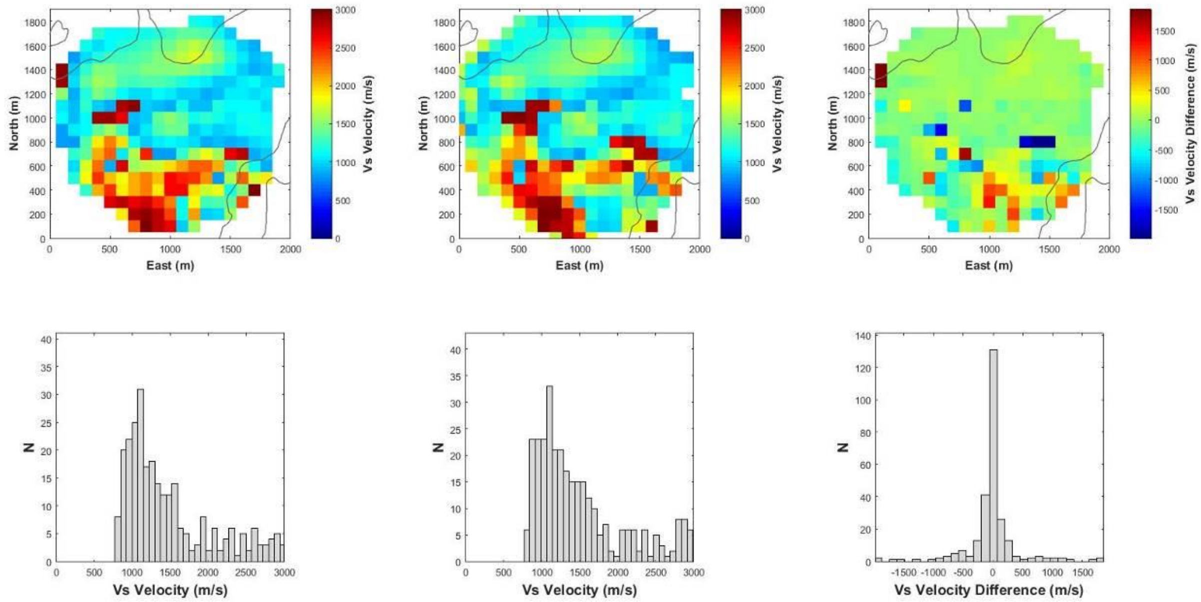


***Figure 64.*** Resulting 2-D spatial variation maps and histograms of half-space Vs velocities from the 1-D inversion of local dispersion curves with (left) and without (center) inter-frequency smoothing constrains and their differences (right).

It should be noted that the 7UL-2 model parameterization layer depths obtained from Love waves are shallower than results for the same area from Hannemann et al. (2014) for Rayleigh wave data. This can result of the strong transverse anisotropy of sedimentary deposits and the faster group velocities of propagating Love waves. To examine the presence of transverse anisotropy for the study area, the derived average bottom layer depths for Rayleigh waves from Hannemann et al. (2014) and for Love waves from this study were compared by computing the $Vs^L/Vs^R$ ratios. The velocities derived from Love wave data theoretically correspond to SH waves, while Rayleigh wave velocities to SV waves. The average $Vs^L/Vs^R$ ratios for the pre-Mygdonian / Mygdonia system sediments discontinuity and the pre-Mygdonian system / bedrock discontinuity are presented in Figure 66. The presence of transverse anisotropy is rather strong in the pre-Mygdonian system sediments, with SH waves travelling roughly 50% larger velocities than SV waves in the south and more than 50% in the north. In contrast, SH waves have roughly 20% faster velocities in the northern part (than SV waves) and nearly the same compared to SV wave velocities in the Mygdonia system sediments. The transverse anisotropy results indicate that the joint inversion of both wave types could potentially provide a better understanding of the actual Vs variation with depth for the study area.

To better understand the shallow structure of the study area, Vs30 maps were computed for the final model and grouped soil classes B, C and D based on the NEHRP soil site classification standard (Figure 67). The results are in good agreement with the local geology, with large Vs30 values dominating the northern part (weathered / healthy bedrock geologic formations, soil sites B and roughly C) and smaller in the south (sediments). The derived maps suggest that the weathered bedrock has significant thickness in the north, while southern results despite being affected by local model instabilities, give a good insight in the soil conditions with soil sites C and D dominating the central and southern part of the test site.

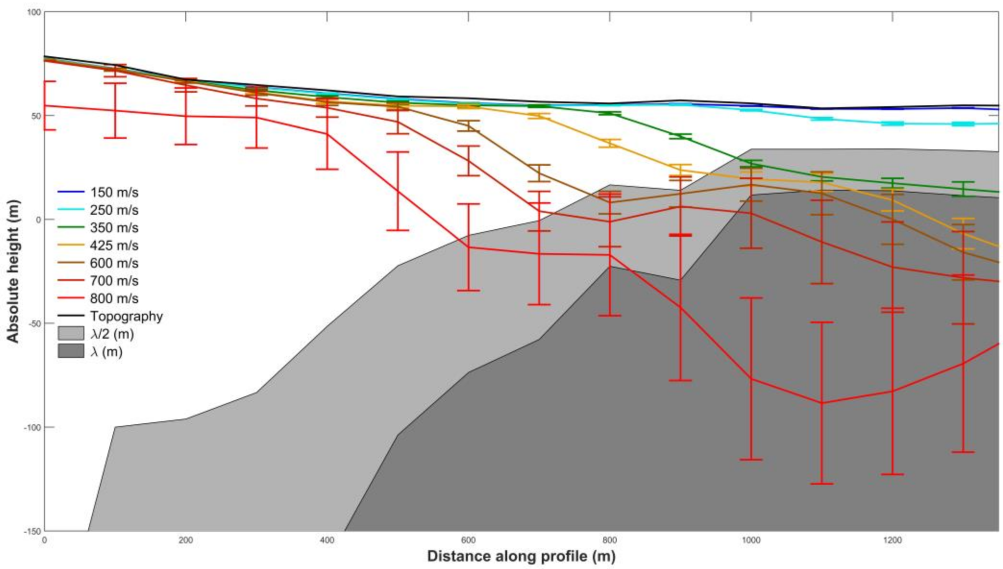


***Figure 65.*** Cross-section along the EUROSEISTEST profile (Table I and Figure 8) depicting the topography, bottom layer average depths (7UL-2 parameterization) and their errors, as well as the maximum and half-maximum wavelengths.

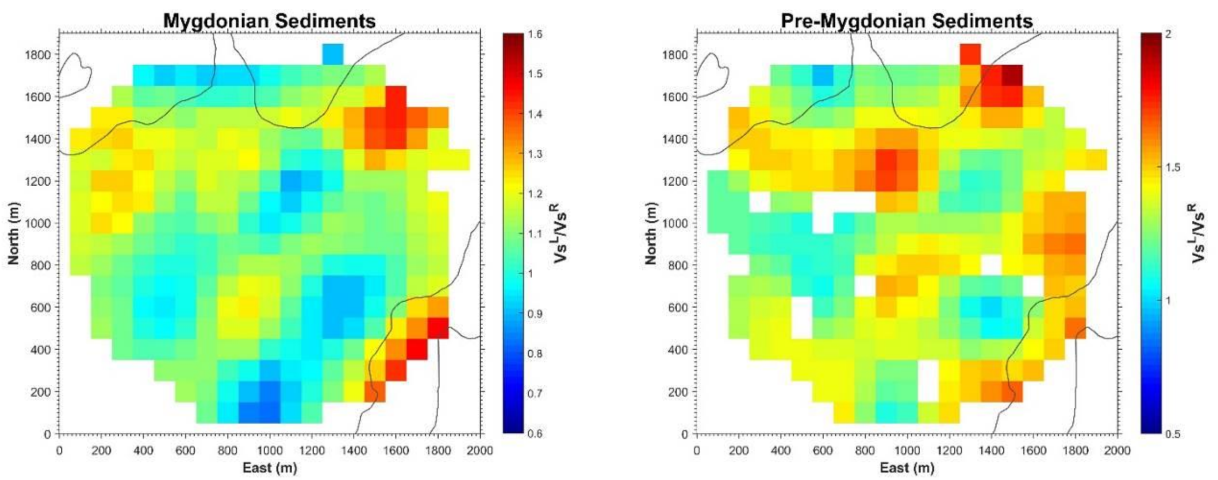


***Figure 66.*** Ratios of $Vs^L/Vs^R$ (theoretically SH/SV) for the Mygdonian (layers D/E in Table I and Figure 8) and pre-Mygdonian system sediments (layers F/G in Table I and Figure 8).

The derived 3D Vs model was compared to independent geophysical information (boreholes, downhole Vs profiles), in order to evaluate its reliability. The comparison of three node models, in the north (X: 800, Y: 1400), central part (X: 1000, Y: 700) and the south (X: 1400, Y: 200) with the available boreholes S2, S5 and S7 (borehole positions marked as stars in Figure 68) is shown in Figure 69. In general, the correlation between the actual Vs profiles and obtained local 1D Vs models are quite adequate. More specifically, the derived results for Love waves show that the 7UL-2 model results fit well with downhole data for borehole S2 and good for borehole S5. The Vs depth variation for borehole S7 does not fit well with the downhole data, with the Love wave model showing a larger Vs velocity increase with depth and depicting a smaller weathered bedrock thickness.

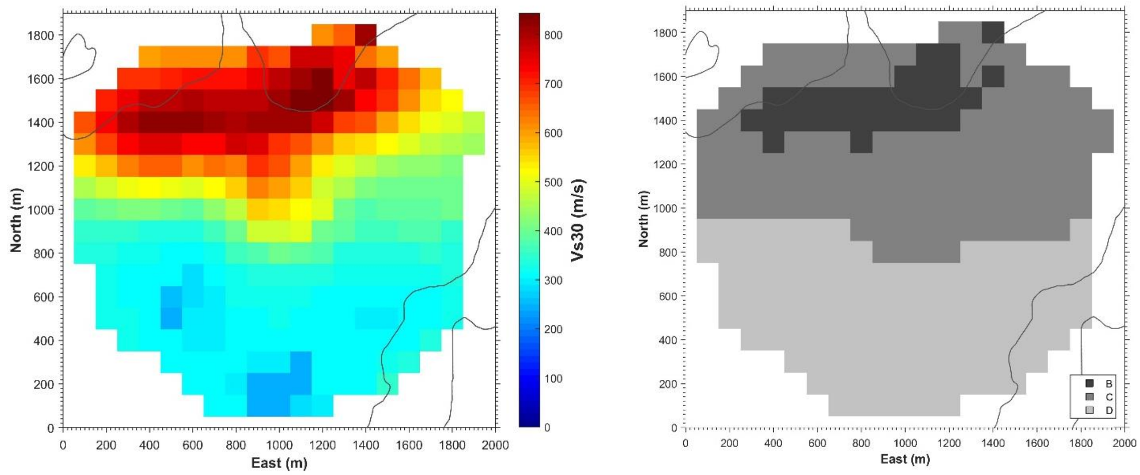


***Figure 67.*** Map of Vs30 velocities for the study area and positions of boreholes S2, S5 and S7 (left) and NERHP soil site classification (right).

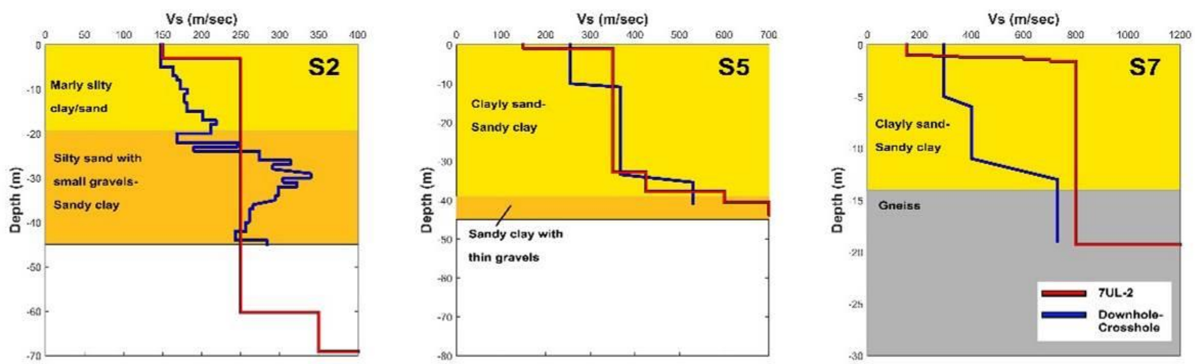


***Figure 68.*** Comparison of downhole Vs profiles (blue) and derived 3-D Vs model (red) variations with depth for three boreholes (positions marked as stars in Figure X) and corresponding borehole geologic profile.

## 3.7. Discussion

The present thesis focused on the generation of a 3-D Vs model for the EUROSEISTEST area (Mygdonia basin, northern Greece) from Love wave ambient noise cross-correlation tomography. The dispersion curve and its errors for each cross-correlation path was manually picked from the maximum RMS amplitudes of the FTAN plots, corresponding to the envelope of the cross-correlation traces. The histograms of the manual picking errors revealed two populations, with the larger error population being mainly distributed in the westernmost part of the array. The final results are strongly affected by the uncertainties of the two step inversion procedure. The first inversion results identify the main basin structure and the resulting group velocity maps derive a velocity border, with its orientation being in good agreement with the outcropping bedrock geometry. The second inversion approach is strongly affected by the initial model parameterization, as suggested by Hannemann et al. (2014) for the same area. The obtained Love wave group travel-times identify three sub-areas, in excellent agreement with the local geology. Specifically, large average group velocities were observed in the north (outcropping bedrock), small in the south (sedimentary deposits) and intermediate in the central part of the area.

The observed Love wave group travel-times for each frequency were inverted using a tomographic approach, with *a-priori* model information (average group slowness computed from the observed travel-times) and the implementation of approximate Fresnel volumes, damping, spatial and inter-frequency smoothing constrains. To improve the efficiency of the inversion scheme, damping and spatial smoothing constrains, which minimize the trade-off between data and model errors were chosen. To obtain smooth inter-frequency variations of group slowness results, the implementation of inter-frequency constraining was adopted, similar to Hannemann et al. (2014). The resulted group slowness maps for each frequency depict the main basin geologic features, exhibiting larger group velocities in the north (bedrock) and smaller in the south (sediments).

The effect of damping and spatial smoothing constrains was tested for the cases of over-damped, under-damped and over-smoothed cases, resulting in group velocities up to ~25 % different than the final results. The impact of damping and spatial smoothing constrains affects the resulting group velocity values for the southern and the northern parts. The synthetic travel-times generated from the inversion and their residuals were compared against the observed travel-times, the inter-station distance and the inter-station angle, without giving any insight for a strong correlation. A maximum number of three iterations was used and data with errors more than two times the RMS error were rejected for each iteration.

Local group slowness dispersion curves were reconstructed for ~270 nodes of the tomographic grid, with more than 10 group slowness values, satisfying resolution quality cut-off criteria. Each node was inverted independently using a directed Monte Carlo inversion approach to find a 1D Vs model. 100.000 ground models were generated for each mode and the average bottom layer depths were computed from the best-fit models. The derived 2-D maps of average bottom layer depths are in good agreement with local geology and resolve well the main basin geologic features.

Despite the local model instabilities, the final pseudo-3D Vs model provides a good insight in the main basin 3-D structure. The resulting Mygdonian / pre-Mygdonian system discontinuity and bedrock interface slopes are presented in Figure 69. It is notable that the maximum slope values are in excellent agreement the morphology of the proposed F1 fault position. Since the slope maps are plotted for different discontinuity depths, these high slope traces are displaced towards the northernmost part of the grid, as we move to larger depths. The F1 fault position is shifted by ~100 m towards the basin center than its proposed position (Raptakis et al. 2010). Furthermore, the "horst-type" structure first reported by Hannemann et al. (2014) is also recognized in the study area. The $Vs^L/Vs^R$ ratios (Figure 66) indicate that transverse anisotropy is strong in pre-Mygdonian system sediments and nearly absent in Mygdonian system sediments. The results from this study suggest that the joint inversion of both surface waves would give a better insight in understanding and modelling the main basin features and 3-D structure. Furthermore, the joint inversion of dispersion curves and HVSR curves could possibly stabilize the local model instabilities, especially regarding the deeper model horizons.

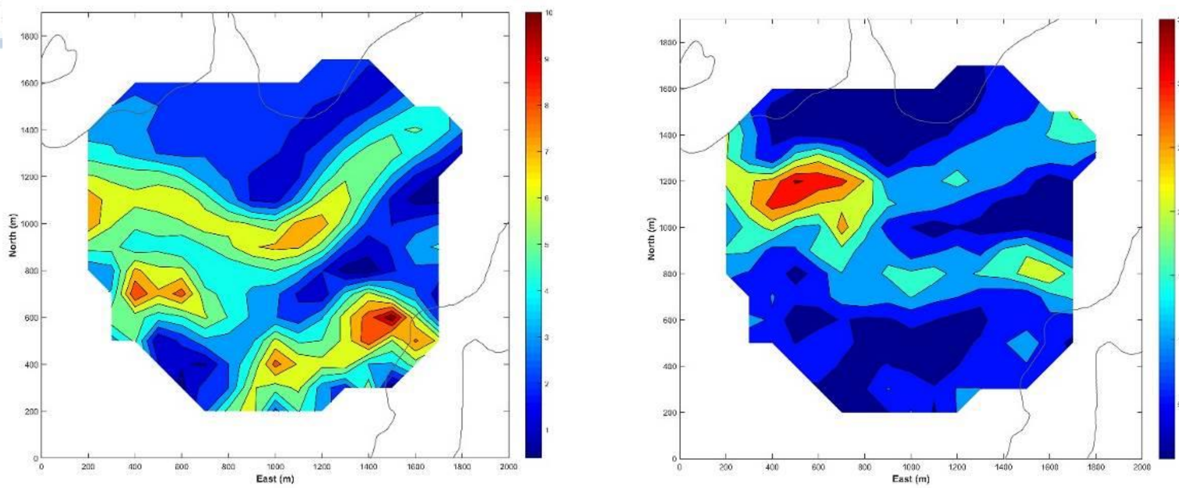


***Figure 69.*** Mygdonian/pre-Mygdonian system sediments discontinuity slope (left) and bedrock interface slope (right).

## *References*

Aki, K. (1957). Space and Time Spectra of Stationary Stochastic Waves, with Special Reference to Microtremors. Bull. Earthquake Res. Inst. Tokyo Univ. 25, pp. 415-457.

Aki, K., W., Lee (1976). Determination of three-dimensional velocity anomalies under a seismic array using first P arrival times from local earthquakes: 1. A homogenous initial model, *J. Geophys. Res*., 81, 4381-4399.

Ashten, M., (1978). Geological Control on the Three-Component Spectra of Rayleigh-Wave Microseism, *Bulletin of the Seismological Society of America Vol. 68*, 1623-1636.

Ashten, M., J., Henstridge (1984). Array Estimators and Use of Microseisms for Reconnaissance of Sedimentary Basins, *Geophysics (49)*, 1828-1873.

Autio, U., Smirnov, M. Yu., Savvaidis, A., Soupios, P., Bastani, M., Combining electromagnetic measurements in the Mygdonian sedimentary basin, Greece, *Journal of Applied Geophysics*, Elsevier, Volume: 135 Special Issue, p. 261-269, DEC 2016.

Becker T.W., C.P., Conrad, A.J., Schaeffer, S., Lebedev (2014). Origin of azimuthal seismic anisotropy in oceanic plates and mantle. *Earth and Planetary Science Letters 401*. 236-250.

Becker, T., J., Kellogg, G., Ekstrom, R., O' Connell (2003). Comparison of azimuthal seismic anisotropy from surface waves and finite strain from global-mantle circulation models, *Geophys. J. Int., 155*, 696-714.

Behm, M., G.H., Leahy, R., Snieder (2013). Retrieval of local surface wave velocities from traffic noise – an example from the La Barge basin (Wyoming), Geophysical Prospecting, 1-21, DOI:10.1111/1365-2478.12080.

Bensen, G.D., M.H. Ritzwoller, M.P., Barmin, A.L., Levshin, F., Lin, M.P., Moschetti, N.M., Shapiro, Y., Tang (2007). Processing seismic ambient noise data to obtain reliable broadband surface wave dispersion measurements, *Geophys. J. Int.*, *169(3)*, 1239-1260.

Bonnefoy-Claudet, S., C., Cornou, P., Bard, F., Cotton, P., Moczo, J., Kristek, D. Fah (2006). H/V ratio: a tool for site effects evaluation. Results from 1-D noise simulations, *Geophys. J. Int.* 167, 827-837.

Bonnefoy-Claudet, S., C., F., Cotton, P., Bard (2006). The nature of noise wavefield and its applications for site effects studies A literature review. *Earth Science Reviews* 79, 205-227.

Bromirski, P., F. Duennebier (2002). The Near-Coastral Microseism Spectrum: Spatial and Temporal Wave Climate Relationships. *Journal of Geophysical Research (107)*.

Burg J.-P. (2012), Rhodope: From Mesozoic convergence to Cenozoic extension. Review of petro-structural data in the geochronological frame, *J. Virtual Explorer*, 42 (1), doi:10.3809/jvirtex.2011.00270.

Capon, J. (1969). High-resolution frequency-wavenumber sprectrum analysis. Proc. IEEEE, Vol. 57, pp. 1408-1418.

Cerveny V, Soares EP (1992). Fresnel volume ray tracing, *Geophysics*, 57(7), 902-915.

Cerveny, P., E.P., Soares (1992). Fresnel volume ray tracing, *Geophysics 57(7)*, 902-915.

Chatzipetros A., Pavlidis S. (1998). A quantitative morphotectonic approach to the study of active faults; Mygdonia basin, northern Greece. *Bulletin of the Geological Society of Greece*. Vol. 32-1 p. 155-164.

Christofides G., A. Koroneos, A. Liati, J. Kral (2007). The A-type Kerkini granitic complex in North Greece: Geochronology and Geodynamic Implications, *Bull. Geol. Soc. Greece XXXX*, 700 - 711.

Christofides G., Koroneos A., Soldatos T., Eleftheriadis G., Kilias A. (2001). Eocene magmatism (Sithonia and Elatia plutons) in the Internal Hellenides and implications for Eocene–Miocene geological evolution of the Rhodope massif (Northern Greece), in: Tertiary Magmatism in the Dinarides, *Acta Vulcanologica*, H. Downes, V. Orlando (eds.), 13, pp. 73–89.

Constable, S., R., Parker, C., Constable (1987). Occam's inversion: A practical algorithm for generating smooth models from electromagnetic sounding data, *Geophysics*, 52, 289-300.

Cupillard, P., L., Stehly, B., Romanowicz (2011). The one-bit noise correlation: a theory based on the concepts of coherent and incoherent noise, *Geophysical Journal International*, 184(3), 1397-1414.

Doukas. I., A. Fotiou, I.M. Ifadis, K. Katsambalos, K. Lakakis, N. Petridou - Chrysohoidou, C. Pikridas, D. Rossikopoulos, P. Savvaidis., K. Tokmakidis and N. Tziavos, 2004. Displacement field estimation from GPS measurements in the Volvi area. TS16 – Deformation Measurements and Analysis I, FIG Working Week May 22-27 Athens, Greece.

Dziewonski, A., S., Bloch, M., Landisman (1969). A technique for the analysis of transient seismic signals, *Bull. Seismol. Soc. Am.*, 59(1), 427-444.

Galanis O. C., Papazachos C. B., Hatzidimitriou P. M., and Scordilis E. M. (2005). Application of 3-d velocity models and ray tracing in double difference earthquake location algorithms: Application to the Mygdonia basin (Northern Greece), *Bull. Geol. Soc*. Greece, 36, 1396-1405.

Gkarlaouni, C., E. Papadimitriou, V. Karakostas, A. Kilias, S. Lasocki (2015). Fault population recognition through microseismicity in Mygdonia region (nothern Greece), *Bollettino di Geofisica Teorica ed Applicata Vol. 56*, 367 - 382.

Gkogkas K., Papazachos C, Anthymidis M., Ohrnberger M., Savvaidis A. (2018). Preliminary results on the 3D structure and transverse anisotropy of the EUROSEISTEST area (northern Mygdonia basin, Greece) from Love wave ambient noise tomography, *16ECEE*, Thessaloniki, 18-21 June 2018.

Gouedard, P., et al. (2008). Cross-correlation of random fields: Mathematical approach and applications, *Geophys Prospect.*, 56(3), 375-393.

Gurk M., A. S. Savvaidis, M. Bastani (2007). Tufa Deposits in the Mygdonian Basin (Northern Greece) studied with RMT/CSTAMT, VLF & Self-Potential, *Kolloquium Elektromagnetische Tiefenforschung, Hotel Maxicky, Decin, Czech Tepublic*, 22, 231 - 238.

Gutenberg, P. (1958) Microseisms, *Advanced Geophysics (5)*, 53-92.

Hannemann K., Papazachos C., Ohrnberger M., Savvaidis A., Anthymidis M., and Lontsi, A.M. (2014). Three-dimensional shallow structure from high-frequency ambient noise tomography: New results for the Mygdonia basin-Euroseistest area, northern Greece, J. Geophys. Res. Solid Earth, 119, 4979-4999.

Kilias A., G. Falalakis , A. Sfeikos, E. Papadimitriou, A. Vamvaka, C. Gkarlaouni (2013). The Thrace basin in the Rhodope province of NE Greece - A tertiary supradetachment basin and its geodynamic implications, *Tectonophysics 595-596*, 90 - 105.

Kilias A., G. Falalakis , D. Mountrakis (1999). Cretaceous-Tertiary structures and kinematics of the Serbomacedonian metamorphic rocks and their relation to the exhumation of the Hellenic hinterland (Macedonia, Greece), *Int Journ Earth Sciences 88*, 513-531.

Kilias A., G. Falalakis, A. Sfeikos, E. Papadimitriou, C. Gkarlaouni, B. Karakostas (2013). The Mesohellenic trough and the Thrace basin. Two Tertiary molassic basins in Hellenides: Do they really correlate?, *Bull. Geol. Soc. Greece XVII*, 551 - 562.

Koufos G. D., Syrides G. E., Kostopoulos D. S., and Koliadimou K. K. (1995), Preliminary results about the stratigraphy and the palaeoenvironment of Mygdonia basin Macedonia, Greece, *Geobios*, 18, 243–249.

Kydonakis K., Brunn J.-P., Poujol M., Monie P., Chatzitheodoridis E. (2015). Inferences on the Mesozoic evolution of the North Aegean from the isotopic record of the Chalkidiki block, *Tectonophysics*, 682, 65-84. doi:10.1016/j.tecto.2016.06.006.

Lacoss R., Kelly, E., Toksoz, M., (1969). Estimation of seismic noise structure using arrays. Geophysics, Vol. 34, pp. 21-38.

Lay, T., Wallace, T. (1995). Modern Global Seismology. Academic Press.

Li, T., F., Ferguson, E., Herrin, B., Durrham (1984). High-Frequency Seismic Noise at Lajitas, Texas, *Bulletin of the Seismological Society of America (Vol. 74)*, 2015-2033.

Lin, F.C., D., Li, R.W., Clayton, D., Hollis (2013). High-resolution 3D shallow crustal structure in Long Beach, California: Application of ambient noise tomography on a dense seismic array. *Geophysics (Vol. 78), No.4*, Q45-Q56.

Manakou, M. V., D. G. Raptakis, F. J. Chavez-Garcia, P. I. Apostolidis, K. D. Pitilakis (2010). 3D soil structure of the Mygdonian basin for site response analysis, *Soil Dynamics and Earthquake Engineering 30*, 1198 - 1211.

Marquardt, D. (1963). An algorithm for least-squares estimation of nonlinear parameters, *Soc. Ind. Appl. Math. J. Appl. Math.*, 11, 431-441.

Menke, W. (1989). Geophysical Data Analysis: Discrete Inverse Theory. Academic Press.

Michail, M., Pipera, K., Koroneos, A., Kilias, A., and Ntaflos, T. (2016). New perspectives on the origin and emplacement of the Late Jurassic Fanos granite, associated with an intra-oceanic subduction within the Neotethyan Axios-Vardar Ocean. *International Journal of Earth Sciences*, 105(7), 1965–1983. doi:10.1007/s00531-016-1321-4.

Michellini, A., T., McEvilly (1991). Seismological studies at Parkfield: I. Simultaneous inversion for velocity structure and hypocenters using cubic B-splines parameterization, *Bull. Seismol. Soc. Am.*, 81(2), 524-552.

Mountrakis D. (2010) Geology of Greece. University Studio Press; 960-12-0139-4.

Mountrakis D., Kilias A., Zouros N. (1993). Kinematic analysis and Tertiary evolution of the Pindos-Vourinos Ophiolites (Epirus-Western Macedonia Greece). *Bulletin of the Geological Society of Greece*, Vol. 28 p.111-128.

Mpogiatzis, P. (2010). Contribution to joint tomography of different types of seismic data, Ph.D Thesis, *Aristotle University of Thessaloniki, Greece*, pp. 228.

Nakamura, Y. (1989). A Method for Dynamic Characteristics Estimation of Subsurface using Microtremor on the Ground Surface, *Quarterly Report of Railway Technical Research Institute (Vol. 30)*, 64-82.

Nogoshi, M., T., Igarashi (1971). On the Amplitude Characteristics f Microtremor (Part 2), *Journal of Seismological Society of Japan (Vol. 24)*, 24-40.

Ohrnberger, M., D., Vollmer, F. Scherbaum (2006). WARAN - A mobile wireless array analysis system for in-field ambient vibration dispersion curve estimation, Abstract-ID 2017, *1st European Conference on Earthquake Engineering and Seismology, ECEES*, 3-8 September 2006, Switzerland.

Okada, H. (2003). The Microtremor Survey Method, *Society of Exploration Geophysics (SEG)*, 135.

Papazachos B. C. and Papazachou C. B. (2003). The Earthquakes of Greece, Ziti Editions, Thessaloniki, pp.286.

Papazachos B. C., Comninakis P. E., Deep structure and tectonics of the Eastern Mediterranean, *Tectonophysics*, Volume 46, Issues 3–4, 1978, Pages 285-296, ISSN 0040-1951, https://doi.org/10.1016/0040-1951(78)90208-1.

Papazachos C. B., D. A. Vamvakaris, G. N. Vargemezis and E. V. Aidona (2001). A study of the active tectonics and deformation in the Mygdonia basin (N. Greece) using seismological and neotectonic data, *Bull. Geol. Soc. Greece* XXXIV, 303 - 309.

Papazachos, B. C., Mountrakis, D., Psilovikos, A. and Leventakis, G. (1979). Surface fault traces and fault plane solutions of the May-June 1978 major shocks in the Thessaloniki area. *Tectonophysics*, 53, 171-183.

Paradisopoulou P. M., V. G. Karakostas, E.E. Papadimitriou, M. D. Tranos, C. B. Papazachos, G. F. Karakaisis (2006). Microearthquake study of the broader Thessaloniki area (Northern Greece), *Annals of Geophysics Vol. 49*, 1081 - 1093.

Pavlidis S., Soulakellis N. (1990). Multifractured seismogenic area of Thessaloniki 1978 earthquake (N. Greece). Proceedings of the International Earth Science Congress on Aegean Regions IESCA – 1990. International Earth Science Congress on Aegean Regions IESCA – 1990. (eds) Savaşçin, M. Y. and Eronat, A. H. Izmir, Turkey. D.E. University, Dept. of Geology. Vol.2 p.64-74.

Poli C., G. Christofides, A. Koroneos, T. Soldatos, D. Perugini, A. Langone (2009). Early Triassic granitic magmatism - Arnea and Kerkini granitic complexes - in the Vertiskos unit (Serbo-Macedonian massif, North-Eastern Greece) and its significance in the geodynamic evolution of the area, *Acta Vulcanologica Special Issue*, 47 - 70.

Psilovikos A. (1977). Paleogeographic development of the basin and lake of Mygdonian (Lagada - Volvi area, Greece), *PhD Thesis*, Department of Geology, Aristotle University of Thessaloniki.

Raptakis D. G., Chavez-Garcia F., Makra K. A., Pitilakis K. D. (2000). Site effects at Euroseistest-I. 2D Determination of the valley structure and confrontation of the observations with 1D analysis, *Soil Dyn. Earthquake Eng.*, 19, 1-22.

Rhie, Z., B., Romanowicz (2004). Excitation of Earth’s continuous free oscillations by atmosphere-ocean-seafloor coupling. *Nature Vol. 431*. 552-556.

Sambridge M (1999a). Geophysical inversion with a neighborhood algorithm-I. Searching a parameter space, *Geophys. J. Int., 138(2), 479-494,* doi:10.1046/j.1365-246X.1999.00876.x.

Sambridge M (1999b). Geophysical inversion with a neighborhood algorithm-II. Appraising the ensemble, *Geophys. J. Int., 138(2)*, 479-494, doi:10.1046/j.1365-246X.1999.00900.x.

Scherbaum, F. (2007). Of poles and zeros: Fundamentals of Digital Seismology, Springer, Dordrecht, Netherlands, 2nd edn.

Seidl, D. (1980). The simulation problem for broad-band seismograms, *J. Geophys. Res.*, 48, 84-93.

Seo, K. (1997). Comparison of Measured Microtremors with Damage Distribution, *In JICA, Research and Development Project on Earthquake Disaster Prevention.*

Shapiro, M., M., Campillo (2004). Emergence of broadband Rayleigh waves from correlations of the ambient seismic noise, *Geophysical Research Letters (Vol. 31)*, L07614.

Sotiriadis L., A. Psilovikos, E. Vavliakis and G. Syrides (1983). Some Tertiary and Quaternary basins of Macedonia/Greece. Formation and evolution, *Clausthaler Geologische Abhandlungen*, pp 21.

Stehly, L., M., Campillo, N., Shapiro (2006). A study of the seismic noise from its long range correlation properties, *J. Geophys. Res. 111, B10306*.

Stein, S., Wysession, M. (2003). An Introduction to Seismology, Earthquakes and Earth Structure. Blackwell Publishing.

Tokimatsu, K. (1998). Geotechnical site characterizatin using surface waves, *Earthquake*

*Geotechnical Engineering*, 1333-1368.

Tong, P., D., Zhao, D., Yang, X., Yang, J., Chen, Q., Liu (2014). Wave-equation-based travel-time seismic tomography – Part 2: Application to the 1992 Landers earthquake (Mw 7.3) area, Solid Earth, 5, 1169-1184.

Toomey, D.R., G.R. Foulger (1989). Tomographic inversion of local data from the Hengil-Grensdalur central volcano complex, Iceland, *J. Geophys. Res.*, 94, 17,497-17,510.

Tranos M. D., E. E. Papadimitriou and A. A. Kilias (2003). Thessaloniki-Gerakarou Fault Zone (TGFZ): the western extension of the 1978 Thessaloniki earthquake fault (Northern Greece) and seismic hazard assessment, *J. Struct. Geol.* 25, 2109 - 2123.

Tranos M., Kilias A., Mountrakis D. (1993). Emplacement and Deformation of the Sithonia Granitoid Pluton (Macedonia, Greece). *Bulletin of the Geological Society of Greece*, Vol. 28-1 p. 195-210.

Vamvakaris D. A., C. B. Papazachos, E.E. Karagianni, E. M. Scordilis, P. M. Hatzidimitriou (2006). Small-scale spatial variation of the stress field in the back-arc Aegean area: Results from the seismotectonic study of the broader area of Mygdonia basin (N. Greece), *Tectonophysics 417*, 249-267.

Wathelet M (2008). An improved neighborhood algorithm: Parameter conditions and dynamic scaling, *Geophys. Res. Lett.*, *35*, L09301, doi:10.1029/2008GL033256.

Yamamoto, H. (2000). Estimation of Shallow S-Wave Velocity Structures from Phase Velocities of Love and Rayleigh Waves in Microtremors, *Proceedings of the 12th World Conference on Earthquake Engineering (Auckland, New Zealand)*.

Yamanaka, H., M., Takemura, H., Ishida, M., Niwa (1994). Characteristics of Long-Period Microtremors and their Applicability in Exploration of Deep Sediments, *Bulletin of the Seismological Society of America (Vol. 84)*, 1831-1841.

Zhang, H., S. Sarkar, M.N., Toksoz, H.S., Kuleli, F., Al-Kindy (2009). Passive seismic tomography using induced seismicity at a petroleum field in Oman, *Geophysics*, 74(6), WCB57–WCB69.